Magneto-optic detection limits for semiconductor spintronics

Indira Zhaksylykova

université PARIS-SACLAY

NNT : 2018SACLX099

Thèse de doctorat

Magneto-optical detection limits for semiconductor spintronics

Thèse de doctorat de l'Université Paris-Saclay
préparée à l'École Polytechnique

École doctorale n°573 Interfaces (approches interdisciplinaires, fondements, applications et innovation)
Spécialité de doctorat : Physique

Thèse présentée et soutenue à Palaiseau, le 12 décembre 2018, par

INDIRA ZHAKSYLYKOVA

Composition du Jury :

Davide BOSCHETTO Chercheur ENSTA, École nationale supérieure de techniques avancées (UMR CNRS 7639)	Président
Xavier MARIE Professeur, Institut National des Sciences Appliquée de Toulouse (UMR 5215 - LPCNO)	Rapporteur
Maria VLADIMIROVA Chargée de recherche au CNRS, Université de Montpellier (UMR CNRS 5221)	Rapporteur
Michel LEQUIME Professeur Emérite, Institut FRESNEL (UMR CNRS 6133)	Examinateur
Alistair ROWE Chargé de recherche au CNRS, École Polytechnique (UMR CNRS 7643)	Directeur de thèse
Yves LASSAILLY Directeur de recherche au CNRS, École Polytechnique (UMR CNRS 7643)	Co-directeur de thèse
Jacques PERETTI Directeur de recherche au CNRS, École Polytechnique (UMR CNRS 7643)	Co-directeur de thèse

Contents

List of Figures

List of Tables

List of Abbreviations

2DEG	Two-**D**imensional **E**lectron **G**as
ABCM	**A**diabatic **B**ond **C**harge **M**odel
BS	**B**abinet-**S**oleil (compensator)
CMRR	**C**ommon **M**ode **R**ejection **R**atio
EOM	**E**lectro-**O**ptic **M**odulator
EPM	**E**mpirical **P**seudopotential **M**odel
FET	**F**ield-**E**ffect **T**ransistor
FOM	**F**igure-**O**f-**M**erit
HH	**H**eavy **H**oles
HW	**H**alf-**W**ave
LC	**L**iquid **C**rystal
LH	**L**ight **H**oles
LED	**L**ight-**E**mitting **D**iode
MO	**M**agneto-**O**ptical (signal)
MOKE	**M**agneto- **O**ptical **K**err **E**ffect
NMR	**N**uclear **M**agnetic **R**esonance
OB	**O**ptical **B**ridge
P	**P**arity (symmetry)
PBS	**P**olarizing **B**eam **S**plitter
PCP	**P**artially **C**rossed **P**olarizers
PEM	**P**hoto**E**lastic **M**odulator
PES	**P**hoto**E**mission **S**pectroscopy
PGC	**P**hase **G**enerated **C**arrier
PL	**P**hoto**L**uminescence
QPC	**Q**uantum **P**oint **C**ontact
RTD	**R**esonant **T**unneling **D**evice
SNR	**S**ignal-to-**N**oise **R**atio
SO	**S**plit **O**ff

SOI	**S**pin-**O**rbit **I**nteraction
T	**T**ime (symmetry)
TGG	**T**erbium **G**allium **G**arnet
TRFR	**T**ime-**R**esolved **F**araday **R**otation

Physical Constants

Bohr magneton	$\mu_B = 9.274\,009\,99 \times 10^{-24}\,\mathrm{J\,T^{-1}}$
Elementary electric charge	$e = 1.602\,176\,62 \times 10^{-19}\,\mathrm{C}$
Planck constant	$h = 6.626\,070\,04 \times 10^{-34}\,\mathrm{J\,s}$
Speed of Light	$c = 2.997\,924\,58 \times 10^{8}\,\mathrm{m\,s^{-1}}$
Vacuum permeability	$\mu_0 = 1.256\,637\,061\,4 \times 10^{-6}\,\mathrm{T\,m\,A^{-1}}$
Vacuum permittivity	$\epsilon_0 = 8.854\,187\,817 \times 10^{-12}\,\mathrm{F\,m^{-1}}$

List of Symbols

B	magnetic field
E	energy
E_g	energy band gap
G	carrier generation rate
g	g-factor
I	light intensity
k	wave vector
L	length of a spin polarized or magnetized area
L_s	spin diffusion length
m	carrier mass
m^*	effective mass of the carriers
n	carrier concentration
N_+	relative population of spin-up electrons
N_-	relative population of spin-down electrons
$\mathfrak{n}$	refractive index
P_{EL}	electronic spin polarization
P_{PL}	circular polarization of light
P_i	initial spin polarization
s	spin concentration
$\mathbb{S}$	Sherman function
T_1	spin relaxation time
T_S	period in a Sagnac loop
V	Verdet constant
$\mathbb{V}$	volume
α	absorption coefficient
Δ_{SO}	split-off energy
η	counting efficiency

θ	analysis angle
θ_F	Faraday rotation angle
λ	wavelength
π	linearly polarized light
σ	diameter of a laser spot
σ^+	right circularly polarized light (from the point of view of the source)
σ^-	left circularly polarized light (from the point of view of the source)
σ_F	Faraday rotation cross section
τ	carrier lifetime
τ_s	spin lifetime
ϕ	phase shift
ω_L	Larmor frequency
ω	angular frequency

Résumé

L'utilisation du degré de liberté supplémentaire du spin électronique dans les structures semi-conductrices, par opposition à la spintronique classique dans les métaux, permet de contrôler le fonctionnement de tout dispositif par des champs électriques via l'interaction spin-orbite ou par des champs magnétiques via l'effet Hanle. L'excitation optique d'électrons polarisés de spin utilisant la lumière polarisée circulairement est un outil puissant pour sonder les propriétés de spin d'électrons dans les semi-conducteurs. Bien que le «pompage optique» soit bien connu en arséniure de gallium (GaAs), il est mal compris dans les semi-conducteurs à gap indirect, tels que le silicium (Si), qui est l'un des principaux candidats à la spintronique des semiconducteurs (Jansen, 2012). À ce jour, les études sur la dynamique de spin dans de tels matériaux utilisent l'injection électrique de spins, par exemple via des contacts tunnel (Dash et al., 2009). Non seulement la fabrication d'échantillons est techniquement difficile, mais aucune information concernant la structure électronique résolue en spin n'est obtenue. Pour ces raisons, l'étude de la dynamique de spin par détection optique présente un intérêt.

En général, le signal de spin électronique à pompage optique est détecté par des techniques polarimétriques, comme la photoluminescence polarisée (PL) ou des expériences classiques de photoémission (PES). Moins fréquemment, le moment magnétique de spin est détecté par des mesures magnéto-optiques de Kerr (MOKE) ou de Faraday. L'analyse comparative des rapports signal sur bruit (SNR) pour chacune de ces techniques est effectuée sur la base d'une expérience de pompage optique typique dans GaAs. Le SNR résultant de ces differentes détections mangéto-optiques s'avère être plus élevé que dans d'autres techniques et, dans la limite du bruit de photons, il dépend de l'intensité de la lumière de sonde, ce qui permet une régulation indépendante du SNR. En outre, ces techniques magnéto-optiques présentent l'avantage d'être mieux adaptées aux mesures dans les semi-conducteurs à gap indirect où le signal mesuré avec les techniques polarimétriques a tendance à être extrêmement petit (Roux, 2008; Favorskiy, 2013). De plus, dans la région de

la transparence, ils permettent une mesure non invasive des moments magnétiques nécessaires à la spectroscopie du bruit de spin (Ryzhov et al., 2015; Vladimirova et al., 2018; Crooker et al., 2004; Dahbashi et al., 2014). Comme les méthodes de détection magnéto-optique ne nécessitent pas la présence d'électrons hors d'équilibre, elles peuvent être utilisées pour étudier la dynamique de spin des porteurs majoritaires (Kato et al., 2004). Ce travail explore l'utilisation de l'effet Faraday magnéto-optique pour étudier la dynamique de spin d'électrons de conduction dans des semiconducteurs non magnétiques dans des conditions de pompage optique.

Le chapitre 1 passe en revue l'état de l'art des méthodes de détection magnétométrique à haute sensibilité. Il est établi que les magnétomètres basés sur l'effet Faraday magnéto-optique sont les mieux adaptés aux études de la dynamique de spin dans les semi-conducteurs non luminescents. Ces magnétomètres peuvent en principe atteindre d'excellentes sensibilités et sont compatibles avec l'application des champs magnétiques transversaux nécessaires aux expériences de dépolarisation de spin de Hanle.

Les bases de l'effet Faraday sont discutées au chapitre 2, suivies d'une comparaison théorique de trois configurations de détection optique permettant des mesures de rotation de polarisation, notamment les polariseurs partiellement croisés (PCP), le pont optique (Chang et al., 2011; Li et al., 2014) et l'interféromètre de Sagnac modifié (Xia et al., 2006). L'analyse des sources de bruit et l'expression analytique du facteur de mérite (FOM) pour chacune des trois techniques sont présentées.

Au chapitre 3, ces configurations de détection sont comparées en termes de sensibilité en mesurant les rotations de polarisation issues d'une couche mince ferromagnétique de cobalt et d'un cristal paramagnétique de grenat de gallium terbium (TGG).

Il a été démontré que l'interféromètre de Sagnac est fonctionnellement équivalent aux polariseurs partiellement croisés. Toutefois, sa performance est compromise par la perte d'intensité lumineuse de chacun des séparateurs de faisceau requis par la géométrie expérimentale. Par contre, il est bien connu que l'interféromètre de Sagnac est capable de différencier les phénomènes réciproques (T) des phénomènes non réciproques ($\overline{\mathrm{T}}$) dans le temps, et cette thèse propose différentes modifications de la géométrie de l'interféromètre de Sagnac, qui, en combinaison avec la technique de porteuse générée en phase (phase generated carrier, PGC), traitent des signaux uniquement sensibles à l'une des quatre combinaisons de symétries de temps

(T) et de parité (P). Ces combinaisons comprennent la symétrie TP, les phénomènes symétriques dans le temps et dans l'espace, caractéristiques de la biréfringence linéaire, la symétrie $\overline{\text{T}}\text{P}$, les phénomènes non réciproques mais symétriques dans l'espace incluant, par exemple, l'effet Faraday, $\text{T}\overline{\text{P}}$, les phénomènes réciproques et asymétriques dans l'espace, avec un exemple de média chiral, et la symétrie $\overline{\text{TP}}$ caractéristique des matériaux ferroélectriques.

À la suite de la comparaison de différentes techniques de détection, le pont optique a montré une mesure de l'angle de rotation de Faraday limitée du bruit de photons, même avec de fortes intensités lumineuses sur les détecteurs, et a atteint le FOM le plus élevé. Dans les démonstrations expérimentales sur des matériaux magnétiques, un bruit de fond de 1,3 nrad $/\sqrt{\text{Hz}}$ est atteint pour une puissance de sonde de 9 mW. Avec cette configuration de détection, le semi-conducteur non magnétique de GaAs ($n = 5,5 \times 10^{15}$ cm^{-3}) a été étudié dans la géométrie classique de l'effet Faraday où le champ magnétique externe présente une composante non nulle dans la direction de propagation de la lumière de la sonde et induit une rotation proportionnelle à cette composante.

Au chapitre 4, une brève description du processus de pompage optique en GaAs est donnée, une mesure standard de photoluminescence polarisée (PL) est ensuite effectuée sur le même échantillon de GaAs à partir duquel un rapport de durée de vie de spin et de porteurs de charges est extrait (τ_s/τ = 0,137). Ensuite, une configuration expérimentale pour une série de mesures de rotation de Faraday à pompe-sonde à température ambiante est décrite et les résultats obtenus sur un échantillon de GaAs pompé optiquement sont présentés. Les angles de rotation de Faraday les plus importants, de l'ordre de 400 μrad, sont détectés lorsque le moment localement sondé est maximisé en focalisant fortement les faisceaux pompe et sonde et en choisissant une longueur d'onde de sonde adaptée à une résonance optique dans la structure électronique. La position de ce pic de résonance pour la rotation de Faraday induite optiquement diffère de la rotation de Faraday classique dans un champ magnétique longitudinal, ce qui peut s'expliquer par une augmentation locale de la température du réseau induit par le processus de pompage optique et qui souligne l'importance de la procédure de réglage (Crooker et al., 2007). À partir des mesures de rotation dans le champ magnétique transverse, la valeur de champ magnétique de Hanle est extraite B_{HWHM} = 0,43 T et la durée de vie du spin est déduite τ_s = 13 ps.

Le dernier chapitre 5 résume les résultats du travail réalisé, aborde les perspectives et les difficultés des expériences possibles sur le silicium à gap indirect pompé optiquement, l'un des candidats les plus prometteurs pour la spintronique à semiconducteurs, où le spin des électrons n'a jamais été mesuré directement par des méthodes optiques.

Introduction

The use of electron spin degree of freedom in semiconductor structures, as opposed to a conventional metal-based spintronics, may offer a control of device operation by electric fields via the spin-orbit interaction, or with magnetic fields via Hanle effect. The optical excitation of spin-polarized electrons by means of circularly polarized light is a powerful tool for provisional exploration of electron spin properties in semiconductors. While this "optical pumping" is well known in Gallium Arsenide (GaAs), it is poorly understood in indirect band gap semiconductors, such as Silicon (Si), which is one of the main candidates for semiconductor spintronics (Jansen, 2012). To date, the few studies of spin dynamics in such materials utilize electrical injection of spins, for example via tunnel contacts (Dash et al., 2009). Not only is the sample fabrication technically challenging, but no information concerning the spin-resolved electronic structure is obtained. For these reasons the study of spin dynamics using optical means is of interest.

Generally, the optically pumped electron spin signal is then detected by means of polarimetric techniques, such as a polarized photoluminescence (PL) or standard photoemission experiments (PES). Less commonly the spin associated magnetic moment is sensed using magneto-optical Kerr (MOKE) or Faraday effects. The comparative analysis of the signal-to-noise ratios (SNR) for each of these techniques is given, and an order of magnitude estimation is done, supposing a typical optical pumping experiment on GaAs. The resulting SNR of magneto-optical detection methods turns out to be higher than in other techniques, and in the shot noise limit it is conveniently dependent on the intensity of probing light, allowing for an independent regulation of the SNR. Besides, such magneto-optical techniques present potential advantages of being better suited for measurements in indirect band gap semiconductors where with polarimetric techniques the signal tends to be immeasurably small (Roux, 2008; Favorskiy, 2013). In addition, in the transparency region, they permit a non-invasive measurement of magnetic moments required for a spin noise spectroscopy (Ryzhov et al., 2015; Vladimirova et al., 2018; Crooker et al., 2004; Dahbashi et al., 2014). Since

magneto-optical detection methods do not require the presence of out of equilibrium electrons, they can also be used to study spin dynamics of majority carriers (Kato et al., 2004).

In Chapter 1, a review of the state-of-the art in high-sensitivity magnetometric detection methods indicates that magnetometers based on the magneto-optical Faraday effect are best adapted for studies of spin dynamics in non-luminescent semiconductors. Such magnetometers can in principle achieve excellent sensitivities and are compatible with the application of transverse magnetic fields necessary for Hanle spin depolarization experiments.

Further, this work explores the use of the magneto-optical Faraday effect to study conduction electron spin dynamics in non-magnetic semiconductors under optical pumping conditions. The basics of the magneto-optical Faraday effect are covered in Chapter 2, followed by a theoretical comparison of three optical detection configurations that allow for polarization rotation measurements, including standard partially crossed polarizers (PCP), an optical bridge (Chang et al., 2011; Li et al., 2014), and a modified Sagnac interferometer (Xia et al., 2006). The analysis of noise sources and the analytic expression for a figure-of-merit (FOM) for each of the three techniques are given. In Chapter 3, these detection configurations are compared in terms of their practical sensitivities to polarization rotations arising from a ferromagnetic thin film of cobalt and from a paramagnetic crystal of terbium gallium garnet (TGG) with results published in The Review of Scientific instruments (Rowe et al., 2017).

It was shown that the Sagnac interferometer is functionally equivalent to partially crossed polarizers, however its performance is compromised by the loss of light intensity on each of the required beam splitters in the experimental geometry. On the other hand, it is well known that the Sagnac interferometer is capable of differentiating between reciprocal (T) and non-reciprocal ($\overline{\text{T}}$) phenomena (Spielman et al., 1990), and this thesis proposes different modifications of the Sagnac interferometer geometry, which, in combination with phase generated carrier technique (PGC), result in signals that are uniquely sensitive to one of the four time (T) and parity (P) symmetries combinations. These combinations include TP symmetry, time and space symmetric phenomena, that is characteristic to linear birefringence, $\overline{\text{T}}$P symmetry, non reciprocal inversion symmetric phenomena that include, for example, the Faraday effect, T$\overline{\text{P}}$, reciprocal but space asymmetric phenomena with an example of

chiral media, and $\overline{\text{TP}}$ symmetry characteristic of ferroelectric materials.

As a result of the comparison of different detection techniques, the optical bridge has shown a photon-shot noise limited measurement of the Faraday rotation angle, even with large photon intensities on the detectors, and has reached the highest FOM. In the experimental demonstrations on magnetic materials, a noise floor of 1.3 nrad/$\sqrt{\text{Hz}}$ is reached for a probe laser power of 9 mW. With this detection configuration, GaAs ($n = 5.5 \times 10^{15}$ cm^{-3}) has been studied in the classical Faraday effect geometry where the externally applied magnetic field has non-zero component along the direction of probe light propagation, and induces the rotation proportional to the strength of this component.

In Chapter 4, a brief description of the process of optical pumping in GaAs is given, a standard polarized photoluminescence (PL) measurement is then performed on the same GaAs sample from which a ratio of spin to carrier lifetimes is extracted ($\tau_s/\tau = 0.137$). Next, an experimental setup for a series of room-temperature, pump-probe Faraday rotation measurements is described and the results on optically pumped GaAs sample are presented. The largest Faraday rotation angles of the order of 400 μrad are found when the locally probed moment is maximized by strongly focusing the pump and probe beams, and by choosing a probe wavelength tuned to an optical resonance in the electronic structure. The position of the resonance peak for optically induced Faraday rotation differs from the classical Faraday rotation in a longitudinal magnetic field, which can be explained by the local heating of the lattice in the optical pumping process, and which emphasizes the importance of the tuning procedure (Crooker et al., 2007). From the Lorentz fit of rotation measurements in the transverse magnetic field the Hanle halfwidth is extracted B_{HWHM} = 0.43 T and the spin lifetime is deduced τ_s = 13 ps.

Chapter 5 summarizes the results of this work, addresses the perspectives and the difficulties of possible experiments on optically pumped indirect band gap silicon, being one of the most promising candidates for semiconductor spintronics, where the spin of electrons has never been measured directly by optical means.

Chapter 1

Motivation

This work is carried out in order to contribute to a field of spintronics that studies spin-related phenomena in solids, and in particular in metals and semiconductors. The practical goal of semiconductor spintronics is to integrate spin of electrons into conventional charge-based electronic devices giving them the potential advantages of non-volatility, increased data processing speed, decreased electric consumption and increased integration densities. In comparison with well-developed metal-based spintronics, the use of semiconductor structures may offer more versatile design of spintronic devices due to the ability of controlling spin polarization in the device channel by external voltages, device structure and doping densities. Another advantage of semiconductors compared to metals is the orders of magnitude longer lifetime of electronic states, that can be explained by reduced electron-electron scattering processes and that permits the transport of spin over much longer distances. Silicon, being the most widely used semiconductor in integrated circuits, is one of the obvious choices for spintronics.

1.1 Spin field-effect transistor (spin FET)

A basic function of a semiconductor spintronic device can be illustrated on an example of spin field-effect transistor (spin FET) first proposed by Datta and Das, 1990 and shown in 1.1. There are three main processes that constitute the function of such device: the spin first needs to be created, the process is called spin injection, then manipulated in the material (spin manipulation) and finally extracted (spin detection).

In such device the spin of electrons aligns with the magnetization of the source

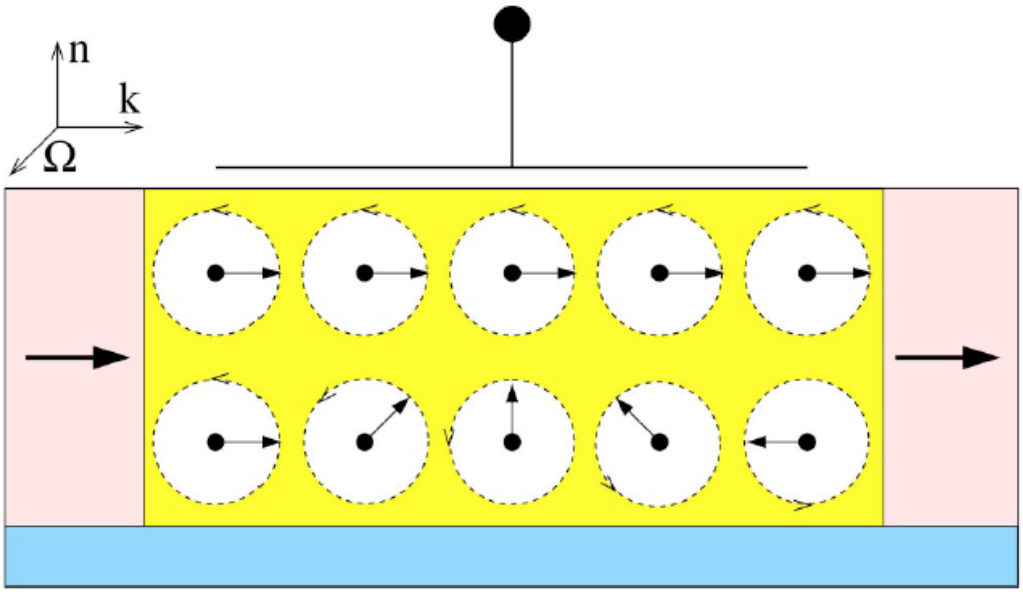

FIGURE 1.1: Scheme of the Datta and Das spin field-effect transistor (Datta and Das, 1990), extracted from (Zutic, Fabian, and Das Sarma, 2004). The source (on the left) and the drain (on the right) are ferromagnetic metals with direction of magnetization aligned with k-direction. The injected spins move ballistically in a heterostructure grown along n. In an external applied electric field electron spins precess about the precession vector Ω, caused by the spin-orbit coupling. In this way, the control of the precession frequency by changing the gate voltage allows for the spin filtering: the current is large if the electron spin has not changed during the passage in the semiconductor channel (top row), and small if its direction has been reversed.

ferromagnet, these spin polarized electrons then travel ballistically through a one-dimensional semiconductor channel to a ferromagnetic drain contact. The electrons whose spin is aligned with the magnetization of the drain ferromagnet are collected, others are scattered away.

The precession of the electron spin direction is along the effective magnetic field that arises from the applied electric gate field and proportional to its strength. In this way, by changing the applied electric field, the current over the channel can be modulated from high (electron spin didn't change its direction) to low (electron spin has rotated by π and get scattered). The effect of spin precession of a moving electron in any electric field is mediated by spin-orbit interaction (SOI), the role of which increases for heavy atoms.

There have been several experiments attempting to construct spin FET. Experiment of Koo et al., 2009 shows a spin FET in nonlocal lateral spin valve geometry, where a high-mobility InAs single quantum well with a strong spin-orbit coupling was used as a semiconductor channel, two $Ni_{81}Fe_{19}$ electrodes served as source and

drain. The function of this spin FET requires the application of magnetic fields (0.5 T) in the direction of electron propagation, temperatures lower than 40 K allow for ballistic transport of electrons along the channel.

Chuang et al., 2015 have manufactured an all-electric spin FET with enhanced ON/OFF switching modulation due to higher spin injection efficiency. An InGaAs heterostructure was used as a two-dimensional electron gas (2DEG) semiconductor channel with several surface gates patterned on its surface. One of them is the middle metallic gate that controls the spin precession, the others are split gates that define quantum point contacts (QPCs) allowing for nearly 100% injection and detection efficiency. The conductance modulation decreases rapidly with temperature and no modulation of the detector voltage is observed for T > 17 K.

1.2 Benefits of a magnetometer

Based on the above examples it is obvious that so far the integration of spin FET into nowadays electronics is far from being realizable. But the paper of Datta and Das, 1990 has provoked a lot of interest in the research field of semiconductor spintronics resulting in further development of the concept of spin FET as well as the proposition for new spintronic devices such as spin LEDs (light-emitting diode) (Jonker, 1999), spin RTD (resonant tunneling device) (Slobodskyy et al., 2003), optical switches, etc. The success in realization of these devices depends on the fundamental knowledge about spin dynamics and spin interactions in solid state materials as well as about the effects of doping concentration, temperature, dimension reduction and electronic band structure in modifying this dynamics. Among the most important parameters characterizing the conduction electron spin are the lifetime of electron spin τ_s and the spin diffusion length L_s. These parameters are going to be the limiting factors for the devices, for instance, the length of the active area should not exceed the spin diffusion length. Furthermore, the time scale associated with spin manipulation should not surpass the spin lifetime. Often these parameters, and the knowledge of how they depend on doping, bias, temperature, strain and geometry, are difficult to extract from the electronic measurements alone, which is why the optical techniques of injection and detection of electron spin provide an alternate noninvasive path.

To date, the most efficient way of optically creating non-equilibrium spin population in semiconductors is provided by optical pumping (Kastler, 1957). In this process, circularly polarized photons of a particular energy create electron-hole pairs with preferential spin orientation. Under continuous pumping conditions, in the steady state, the photocreated carrier density is a product of a generation rate G and a carrier lifetime τ: $n = G\tau$. The concentration of electron spin is smaller by a factor of $P_i\tau_s/\tau$: $s = P_i G\tau_s$, where τ_s is the spin lifetime and P_i is an initial spin polarization, dictated by electronic structure of a specific semiconductor. The absolute value of P_i for direct band gap GaAs is equal to 0.5 and is relatively easy to calculate (details in Section 4.1), whereas its calculation is much more complicated in the case of indirect band gap silicon (see B.2).

Further, we are going to describe three optical detection techniques and compare them analytically by looking at the expressions for signal, noise and signal-to-noise ratios (SNR) (see Table 1.1), as well as estimating the SNR in each case supposing a typical optical pumping experiment conducted on GaAs.

Once the spin population has been created, there are different ways to optically detect it. The most common experimental technique for studying the optical pumping in semiconductors is called polarized photoluminescence (PL), where one detects the circular polarization of photons reemitted in the process of radiative recombination of electron-hole pairs. In this way, the signal in the PL technique is proportional to the total number of spins $S = s\mathbb{V}$, where $\mathbb{V}$ is the volume where the spin is created. It is also proportional to P_i, since the selection rules are reversible in time and it is the polarization of photons that is detected. The efficiency of the detection scheme in collecting those photons is expressed with η, a counting efficiency, which in the PL experiment is typically equal to 10^{-4} (Favorskiy et al., 2010). In the absence of all noise sources except the photon shot noise, the noise of the measurement is a square root of the total number of photons detected by the system $\sqrt{N \cdot \eta} = \sqrt{n\mathbb{V}\eta}$.

There is another polarimetric technique - polarized photoemission spectroscopy (PES), which measures the spin polarization of electrons emitted from the semiconductor surface by photoelectric effect. In this case, as compared with the PL experiment, the signal is again proportional to the total amount of spin $s\mathbb{V}$, the detection efficiency is much lower, $\eta^* \approx 10^{-8}$, and P_i is replaced by a Sherman function $\mathbb{S}$ which is dependent on the experimental conditions, but is close to 0.3 (Favorskiy, 2013). The shot noise of electrons in such measurement is equal to $\sqrt{n\mathbb{V}\eta}$.

Detection method	Signal	Shot noise	SNR	SNR estimation, GaAs
Polarized photoluminescence	$s\mathbb{V}\cdot\eta P_i$	$\sqrt{n\mathbb{V}\eta}$	$\frac{P_i G\tau_s}{\sqrt{G\tau}}\sqrt{\eta\mathbb{V}}P_i$	1
Photoemission spectroscopy	$s\mathbb{V}\cdot\eta^*\mathbb{S}$	$\sqrt{n\mathbb{V}\eta^*}$	$\frac{P_i G\tau_s}{\sqrt{G\tau}}\sqrt{\eta^*\mathbb{V}}\mathbb{S}$	10^{-2}
Magnetometry based on Faraday effect	$\theta_F\cdot I_0$	$\sqrt{I_0}$	$P_i G\tau_s\sigma_F L\cdot\sqrt{I_0}$	10^2

TABLE 1.1: A comparison of analytical expressions for signal to noise ratios (SNR) of three detection methods: polarized photoluminescence, spin resolved photoemission spectroscopy and magneto-optical detection based on Faraday effect. An estimation of the SNR is given in the last column for a typical optical pumping experiment conducted on GaAs.

The last technique, the magnetometry based on magneto-optical (MO) Kerr or Faraday effect, qualitatively differs from the first two methods. It measures a rotation of linear polarization of light that is reflected from (Kerr effect) or transmitted through (Faraday effect) a magnetized media. This rotation, which we call θ_F, is proportional to the sample magnetization, and thus, to the spin concentration s in the case of optically pumped semiconductors. It is also proportional to the length of the spin polarized volume, L, via a proportionality factor σ_F called a Faraday cross-section (Giri et al., 2012): $\theta_F = \sigma_F sL$. The signal in the measurement is then the product of the Faraday rotation θ_F and the intensity of probing light I_0. The noise in such measurement, in the limit of shot noise, is equal to square root of the probe light intensity, and hence, the SNR of such technique is also proportional to $\sqrt{I_0}$.

At this point we can compare the SNR dependencies in all three cases (see SNR column in Table 1.1) and mark out two main advantages of the magneto-optical method with respect to PL and PES methods. The SNR in the case of PL method is proportional to P_i^2, where $P_I < 1$, in the case of PES method it is proportional to $P_i\mathbb{S}$, where $\mathbb{S} < P_i$. On the contrary, the SNR of magneto-optical methods is only linearly proportional to P_i, which results in a factor $1/P_i$ gain. The second advantage of magneto-optical methods is related to the possibility of tuning up the SNR by increasing the probe intensity I_0, as long as you stay in the shot noise limit.

Now, in order to make an estimation for SNR in each technique, we are going to look at a typical optical pumping experiment conducted on GaAs, where a 785 nm laser source of 10 mW power, of a circular polarization is focused to a 10 μm

diameter spot. Supposing 100 ps spin lifetime (Zerrouati et al., 1988) and a reasonable average of 10% for steady state electronic spin polarization, we get an estimate for carrier lifetime τ = 0.5 ns. Under such conditions, and taking into account the mentioned approximate values for η, η^* and S, we can evaluate the SNR for the first two techniques, which gives $SNR_{PL} \approx 1$, $SNR_{PES} \approx 10^{-2}$, which can be found in the last column of Table 1.1.

The estimation of the SNR for MO detection using Faraday effect requires some information on the probe source of light, and we take a 825 nm source of 10 mW power. More importantly, an order of magnitude for the Faraday rotation has to be known, and we rely in our calculations on the study of spin Hall effect in GaAs by Kato et al., 2004, where using the Kerr rotation microscopy the authors have measured the maximum of 2 μrad rotation accumulated near the edges of the GaAs sample. Using these values we can evaluate the SNR for the MO detection methods: $SNR_{MO} \approx 10^2$.

Based on this rough estimation in direct band gap semiconductor such as GaAs where, in principle, the polarimetric techniques have proven to work (Zakharchenya et al., 1971; Pierce, Meier, and Zürcher, 1975), it seems like the magnetometric techniques might be a good alternative, or can be used in combination with polarimetric techniques providing an additional information about the semiconductor.

Moreover, this technique might be used to study optical pumping in indirect band gap semiconductors like Silicon. The lifetime of photocreated carriers τ in such semiconductors tends to be very long (of $\sim$ 1 ms in undoped Si (*Electrical properties of Silicon (Si)*)), and this makes the resulting SNR for the PL and PES techniques (which are $1/\sqrt{\tau}$ functions of the lifetime) immeasurably small (Roux, 2008; Favorskiy, 2013). The SNR of the MO detection method, on the other hand, does not contain a τ dependence, and thus is potentially better suited for optical pumping in indirect semiconductors.

MO detection in the transparency region is also proven to be useful in studies of nuclear spin requiring non-destructive off-resonant measurements (Giri et al., 2013), studies of spin noise spectroscopy (Ryzhov et al., 2015; Vladimirova et al., 2018; Crooker et al., 2004; Dahbashi et al., 2014) and the study of spin dynamics of majority carriers (Kato et al., 2004).

1.3 Detection of a small number of spins

In the case of optically pumped semiconductors it is the magnetization created by a circularly polarized light that has to be measured. Considering again the optical pumping experiment performed on GaAs and taking the value of g-factor at room temperature, $g = 0.3$ (Litvinenko et al., 2008), we can estimate the value of an electron spin associated magnetic moment $m = \frac{g\mu_B}{2} s\mathbb{V}$ to be $\approx 10^{-15}$ emu, or 10^{-18} J/T. A magnetometer of choice for this type of experiment has to be sensitive enough to magnetic moments of such amplitude, and since some magnetometers measure magnetic fields, it is important to envision the geometry of an experiment. This optically created magnetic moment is going to be sensed at the point where the sensor is positioned for a particular magnetometer. To simplify, we consider the volume where the spin population has been created to be a single magnetic dipole of strength $m \approx 10^{-15}$ emu. The created magnetic field dependence on the distance r from the magnetization point is described by the following equation:

$$\mathbf{B}(\mathbf{r}) = \frac{\mu_0}{4\pi}\left(\frac{3\mathbf{r}(\mathbf{m}\cdot\mathbf{r})}{r^5} - \frac{\mathbf{m}}{r^3}\right), \tag{1.1}$$

where μ_0 is the vacuum permeability. This expression simplifies in the case where we look at the field in the direction of the dipole:

$$B(r) = \frac{\mu_0}{2\pi}\cdot\frac{m}{r^3}. \tag{1.2}$$

The above magnetic field dependence on the distance from the dipole of strength $m = 10^{-15}$ emu is plotted in Fig. 1.2 in the direction of the dipole. This figure will serve as a tool when trying to work out the relevance of each of the magnetometers for our experiments. Depending on the distance and the magnetic noise floor of the considered magnetometer we can then conclude whether this magnetometer has enough sensitivity to measure optically induced magnetic moments or not.

Next, the geometry of an experiment must allow for a pump laser to hit the sample for optical spin injection. Finally, for the Hanle effect measurement, typically performed to confirm the spin nature of the signal, the external magnetic field needs to be applied in the direction perpendicular to the pump light $\boldsymbol{k}$-vector of propagation, thus, perpendicular to the actual magnetic field to measure. This implies that scalar magnetometers that measure the total value of magnetic field should be

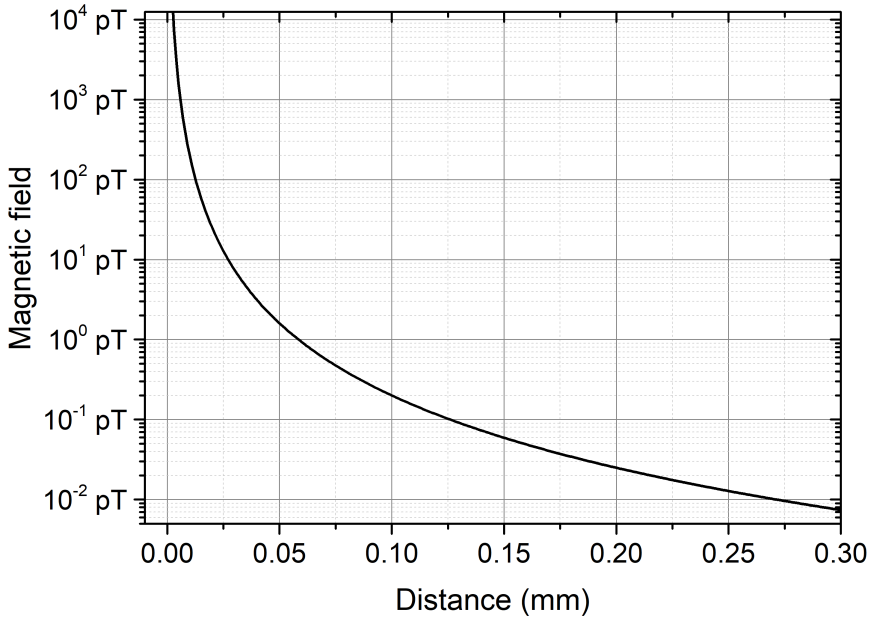

FIGURE 1.2: Dependence of magnetic field on distance from magnetic dipole of value 1×10^{-15} emu that corresponds to our estimation of magnetic moment created in GaAs by optical pumping.

avoided.

The aim of this part of Chapter 1 is to focus on those magnetometers that potentially have the required sensitivity and are compatible with the application of transverse magnetic field in Hanle measurement and illumination with the pump light for optical injection of electron spins in semiconductors.

In tables 1.2 and 1.3 brief information on some high sensitivity magnetometers is gathered for a quick comparison. Several articles and books have been published that describe different types of magnetometers (Grosz et al., 2016; Ripka, 2001; Popović, 1989; Díaz-Michelena, 2009). Our review of sensitive magnetometers is based mainly on these references.

1.3.1 Induction coil magnetometer

The first type of magnetometer considered here is one of the oldest and most well-known, it is the induction coil magnetometer. Such magnetometers measure the

Name	Noise floor	Comments (pros and cons)
Induction coil magnetometer	80 fT/$\sqrt{\text{Hz}}$[a] (1 Hz)	+: available commercially, -: temperature stabilization, -: complicated geometry of the Hanle measurement
SQUID	0.33 fT/$\sqrt{\text{Hz}}$ (1 kHz) state of the art[b] 10^{-8} emu for commercial SQUID[c]	-: weak sensitivity of commercially available SQUIDs, -: cryogenic temperatures, complicated fabrication of state of the art SQUIDs
Fluxgate magnetometer	1 pT/$\sqrt{\text{Hz}}$ (1 Hz) state of the art[d], 12 pT/$\sqrt{\text{Hz}}$ (1 Hz) commercial[e]	+: available commercially, -: complicated geometry of the Hanle measurement
Planar Hall effect (PHE) magnetometer AMR magnetometer GMR magnetometer GMI magnetometer	200 pT/$\sqrt{\text{Hz}}$(1 Hz) state of the art[f] 2 nT/$\sqrt{\text{Hz}}$ (1 Hz)[g] 100 pT/$\sqrt{\text{Hz}}$[h] 1.3 pT/$\sqrt{\text{Hz}}$[i]	+: available commercially, -: low sensitivity -: temperature dependence

TABLE 1.2: Sensitive magnetometers characteristics. Magnetometers available commercially.

[a] *BF-4 Magnetic Field Induction Sensor* 2009.
[b] Schmelz et al., 2011.
[c] *Cryogenic Limited - S700X SQUID Magnetometer* 2018.
[d] Butta and Sasada, 2014.
[e] *TFM100-G2 Ultra miniature triaxial fluxgate magnetometer* 2008.
[f] Grosz et al., 2016.
[g] Ripka et al., 2003.
[h] Fermon and Pannetier-Lecoeur, 2013.
[i] Yabukami et al., 2009.

Magnetic resonance force microscopy (MRFM) magnetometer	single spin measurement[a]	+: microscopy -: cryogenic temperatures, vacuum, indirect measurement of the magnetization
Torque magnetometry	1.3×10^{-20} Nm/$\sqrt{\text{Hz}}$[b]	-: sample combined with detector requires fabrication
Spin excahge relaxation free (SERF) magnetometers	0.16 fT/$\sqrt{\text{Hz}}$[c]	-: heated temperature conditions -:scalar magnetometer
Magneto-optical magnetometry (MOKE, Faraday effect)	400 pT/$\sqrt{\text{Hz}}$[d]	+: ambient conditions -: indirect measurement of magnetization in the case of optical pumping

TABLE 1.3: Sensitive magnetometers characteristics. State of the art laboratory magnetometers.

[a] Rugar et al., 2004.
[b] Wu et al., 2017.
[c] Dang, Maloof, and Romalis, 2010.
[d] Rowe et al., 2017.

change in the magnetic flux according to Faraday's law of induction. The most sensitive magnetic field induction sensor available commercially is the one from Schlumberger[1] with a magnetic field sensitivity of 0.08 $\mathrm{pT}/\sqrt{\mathrm{Hz}}$ at 1 Hz, which might, in principle, be sensitive enough to measure optically induced magnetization if placed at distances < 0.1 mm. However, from the practical viewpoint, in the case of detecting magnetic fields smaller than 1 pT, the application of transverse magnetic fields of the order of 1 T typically necessary for the Hanle measurements, might be complicated: in order to avoid components of the applied magnetic field along the direction of the detection we will have to be able to align the two field to within a picoradian, which is practically impossible thing to do.

1.3.2 Superconducting quantum interference device

Probably the most commonly used laboratory magnetometer is a superconducting quantum interference device (SQUID) magnetometer, discovered in 1960s (Jaklevic et al., 1964), and which has, since its discovery, many applications for the detection of weak magnetic fluxes. Its operation principle is based on Josephson tunneling (Josephson, 1962) and magnetic flux quantization and the entire device is cooled below cryogenic temperatures to maintain superconductivity. A standard commercial SQUID magnetometer has noise level of 10^{-8} emu[2], which is obviously not enough for our goal.

The most sensitive state-of-the art reported SQUID magnetometer consists of 12 Josephson loops and is able to measure fields down to sub-fT region with noise floor = 0.33 $\mathrm{fT}/\sqrt{\mathrm{Hz}}$ at frequencies > 1 kHz that increases to several $\mathrm{fT}/\sqrt{\mathrm{Hz}}$ at 1 Hz, Schmelz et al., 2011. The cryogenic requirements limit the temperature range of measurements that can be easily studied with SQUIDs. In addition, to block out any external magnetic fields (like, for example, Earth's magnetic field) the SQUID must be operated within a superconducting shield. A sample is thus spatially separated from the SQUID and the magnetic flux from it is transferred to the SQUID via a superconducting pick-up coil. In such situation the coupling factor between sample's magnetization and the SQUID is weak and limits the sensitivity of the entire device.

[1] *BF-4 Magnetic Field Induction Sensor* 2009.
[2] *Cryogenic Limited - S700X SQUID Magnetometer* 2018.

After the discovery of high-Tc superconductors, SQUIDs cooled with liquid nitrogen have become fairly common, but they suffer from one to two orders of magnitude loss in sensitivity compared with low-Tc SQUIDs (Clarke, 1997).

The idea of measuring the magnetization reversal of an individual magnetic particle has led to the development of micro- and nano-SQUIDs. The coupling factor is enhanced greatly when the sample is in the immediate vicinity of the SQUID, small molecules can even be deposited on top of the loop. Such SQUIDs are much smaller in size, with loop sizes varying from $2 \times 2\ \mu m^2$ for micro-SQUIDs to $100 \times 200\ nm^2$ for nano-SQUIDs (Wernsdorfer, 2009; Bouchiat, 2009). The sensitivity to a reversal of 10^{-17} emu was shown for a micro-SQUID (Wernsdorfer, Mailly, and Benoit, 2000), which is likely enough for our needs but the manufacturing of such a device with all the requirements might be very complicated, if not impossible. In addition, the need to cool down the superconducting loop limits the study to cryogenic temperatures.

1.3.3 Fluxgate magnetometer

The third type of commercially widely available magnetometers is fluxgate. A fluxgate magnetometer is a device which measures magnetic fields utilizing the nonlinear magnetic characteristics of the ferromagnetic core material. Commercial fluxgate magnetometers measure magnetic fields $\leqslant 12$ pT[3]. The sensitivity of few cm sized state-of-the art fluxgate magnetometers is in the order of 1 pT/$\sqrt{\text{Hz}}$ (Hinnrichs et al., 2001; Butta and Sasada, 2014) at room temperatures.

Although if placed extremely close to the optically pumped semiconductor these magnetometers might be sensitive to the induced magnetization, the complicated Hanle effect geometry requiring an extreme alignment to within a picoradian of high transverse magnetic fields can be very difficult to achieve practically.

1.3.4 Hall sensors, magnetoresistive and magnetoimpedance magnetometers

Hall sensors are magnetic field sensors widely used in industrial applications such as current-sensing, position, speed and timing detection (Ramsden, 2001), etc. They are miniature in size ($\sim$ several mm^3) pieces of semiconducting materials such as GaAs, Si, InAs, InP, InSb or graphene. In general, these sensors exhibit lower sensitivities than fluxgate magnetometers, the noise level in state of the art experiment

[3] *TFM100-G2 Ultra miniature triaxial fluxgate magnetometer* 2008.

is 200 pT/$\sqrt{\text{Hz}}$ (Grosz et al., 2016). If put in contact with one surface of the sample which is illuminated with a circularly polarized light from the other side, the Hall magnetometer with a sensitivity to 200 pT will be able to resolve spin signal if the thickness of the sample is < 10 μm (estimated according to the Fig 1.2). A typical thickness of a bulk semiconducting substrate is no thinner than 300 μm, and the samples that we have chosen for the study are 500 μm thick, meaning that the most sensitive Hall magnetometers won't be able to resolve the expected magnetization.

Magnetoresitive and magnetoimpedance sensors include anisotropic magnetoresistance (AMR), giant magnetoresistance (GMR) and giant magnetoimpedance (GMI) magnetometers. The sensitivities of state of the art magnetometers are specified in Table 1.2. Still, even in the case of the most sensitive GMI magnetometers, the thickness of the sample has to be smaller than 50 μm estimated, again, with Fig. 1.2 and formula Eq. 1.2.

1.3.5 Magnetic resonance force microscopy

Magnetic resonance force microscopy (MRFM) combines the action of scanning probe microscopy with magnetic resonance imaging (MRI). In a typical MRFM experiment, a tiny cantilever with a magnetic tip attached to the end of it senses the weak magnetic force between the spins in the sample and the magnetic tip. Rugar et al., 2004 has reported a measurement of an individual spin in SiO_2 sample with low spin concentration (between 10^{13} and 10^{14} cm^{-3}). While this is a very promising and very sensitive technique that does not require the sample preparation, it does not yet allow the room temperature measurements: the experiments are performed at 1.6 K in a vacuum chamber to minimize the force noise and reduce the relaxation rate of the spins.

1.3.6 Torque magnetometry

Magnetic torque magnetometry is another technique that uses mechanical sensors to detect, in this case, magnetic torques $\tau = \mu_0 m \times H$. Any fluctuation in position of torque sensors is detected via cavity-optomechanical coupling and extreme torque sensitivities were achieved by Kim et al., 2013 (4×10^{-20} N m $/\sqrt{Hz}$ in vacuum chamber) and by Wu et al., 2017 (1.3×10^{-20} N m $/\sqrt{\text{Hz}}$). Depending on the values of field that are applied in order to deflect magnetized samples due to magnetic torques, they can probe magnetic moments on the order of 3×10^{-14} emu.

Such devices can potentially be effective for the probe of optically created electron spins in semiconductors but it would require a hard work on the preparation of the device with sample of choice combined with the detector.

1.3.7 SERF magnetometer

Atomic magnetometers are one of optical magnetometers that rely on a measurement of the Larmor precession of optically pumped atoms of alkali metals, most commonly potassium atoms. An atomic magnetometer working in a spin exchange relaxation free (SERF) regime has demonstrated magnetic field sensitivities of 0.16 $\mathrm{fT}/\sqrt{Hz}$ (Dang, Maloof, and Romalis, 2010) that has overcome the most sensitive SQUIDs. This regime is achieved by operating at a high alkali-metal densities and in a very low field, on the order of 1 nT or less. Unlike SQUIDs, atomic magnetometers do not require cryogenic temperatures and studies can be made over a wide range of temperatures up to $\sim 450^{\circ}\mathrm{C}$.

The adaptation of such type of magnetometers for materials characterization is still under development. So far, the closest distance between the sample and the alkali cell is around 1 inch (Romalis and Dang, 2011), and the field produced by our semiconductor in a typical optical pumping experiment at such distances ($\sim 6 \times 10^{-20}$ T) is well below the detection limit of SERF magnetometers.

Another drawback of this technique applied to our case is the impossibility of the Hanle effect observation as it requires application of large transverse magnetic fields that aren't compatible with the setup and would certainly destroy the SERF regime.

1.3.8 Magneto-optical magnetometery

The mentioned magneto-optical magnetometry based on Kerr effect (MOKE) or Faraday effect, refers to a magnetization-proportional change in polarization of light upon reflection from (in Kerr geometry), or transition through (in Faraday geometry), respectively, a magnetized media. The change in polarization manifests itself either via the rotation of a linear polarization of light that passes through the magnetized media, or via the change in intensity that results in elliptic polarization. These techniques are successfully used in studying magnetic anisotropy (Su, Chang, and Chang, 2013), single spin dynamics in quantum wells (Atatüre et al., 2007), magnetic vortices in superconductors (Koblischka and Wijngaarden, 1995), non-equilibrium

spin polarized electrons in semiconductors (Baumberg et al., 1994; Kikkawa and Awschalom, 1999; Kato et al., 2004) and orbital magnetism in graphene (Crassee et al., 2011).

The efficiency of the material in generating classical Faraday rotation is described by the Verdet coefficient, that is defined as the proportionality factor between the Faraday rotation θ_F, the applied magnetic field B and the length of the optical path within the material l: $\theta_F = VBl$. The magnetic noise floor achieved in our measurements on magnetic samples (see Chapter 3.2) under an applied magnetic field is on the order of 400 $\mathrm{pT}/\sqrt{\mathrm{Hz}}$. Although such sensitivies compare with less sensitive magnetometers mentioned here, this technique suits better the geometry of our experiment, described in details in 4.4.1, and has proven to work within nonmagnetic semiconductors (Kikkawa and Awschalom, 1999; Kato et al., 2004; Furis et al., 2007; Giri et al., 2013).

One difference of this technique compared to all the others is that the measured magnetization dependent quantity, the Faraday or Kerr rotation, results from the non-destructive interaction of the probe light with the matter. Thus, there is no spatial separation between the sample and the detector, the material itself playing the role of magnetic sensor.

Another advantage of such optical technique where the light interacts with the material directly is that it can energetically resolve the signal depending on the wavelength of probing light as compared to other techniques which sense an averaged magnetic field.

To sum up, these magnetometers appeared to us to be the most convenient for the measurements of optical pumping in non-magnetic (in equilibrium) semiconductors.

In what follows we will concentrate on the chosen approach, which is the magneto-optical Faraday effect magnetometry. The theoretical basics are covered in the next chapter, where we discuss the nature of the effect, the dependence of the Faraday rotation on the wavelength of the probing light, followed by theoretical comparison of performances of different optical detection schemes.

Chapter 2

Magneto-optical Faraday effect: detection schemes

2.1 Magneto-optical Faraday effect basics

A linearly polarized light can be thought to be composed of two circularly polarized left and right components. The Faraday effect results from the difference of velocities with which these two components pass through a material of length L. The rotation of the plane of polarization of so-called probing light expresses via the difference of refractive indices for right ($\mathfrak{n}_+$) and left ($\mathfrak{n}_-$) circularly polarized components (Piller, 1972):

$$\theta_F = \frac{\omega L}{2c}(\mathfrak{n}_- - \mathfrak{n}_+). \tag{2.1}$$

This general expression does not depend on the source of differing velocities and thus is valid both in the case of external magnetic field applied in the direction of light propagation and in the case of optical pumping with circularly polarized light. The presence of an external magnetic field applied in the direction of light propagation produces a Zeeman splitting, creating a difference in the angular frequency for the two components of radiation of value ω_L (Larmor frequency). The equation 2.1 for the Faraday rotation then takes the following form:

$$\theta_F = \frac{\omega L}{2c}[\mathfrak{n}(\omega - \omega_L) - \mathfrak{n}(\omega + \omega_L)] = \frac{\omega \omega_L L}{c}\frac{d\mathfrak{n}}{d\omega} \equiv VBL. \tag{2.2}$$

The Verdet constant V introduced here is a proportionality factor between the Faraday angle, the magnitude of the applied magnetic field and the length of the material.

In semiconductors, there are two Faraday rotation regimes related to two different probe wavelength domains: intraband and interband transitions. The intraband, or free carrier transitions are due to free carriers such as electrons in the conduction band. They appear for small photon energies, well below the band gap, thus for longer wavelengths of the probe light. The interband transitions happen closer to the fundamental absorption edge and involve transitions of electrons from the valence band to the conduction band. The dependence of the rotation angle on the wavelength is different depending on what transitions are involved. For example, in the free carrier absorption region the Faraday rotation angle, through the Verdet coefficient, depends as the square of the probe wavelength (Piller, 1972, Eq. 4):

$$\theta_F \propto V = \lambda^2 \frac{e^3 n}{8\pi^2 c^3 \mathfrak{n} \epsilon_0 m^{*2}}, \tag{2.3}$$

where n is the density of the charged carriers, λ is the wavelength of the probing light, $\mathfrak{n}$ is the refractive index at this wavelength, ϵ_0 is the dielectric constant of vacuum and m^* is the effective mass of the carriers.

As an example, this dependence was observed by Cardona, 1961 in a classic Faraday effect measurement of a 830 μm thick GaAs where the magnetization is induced by means of externally applied longitudinal magnetic field of strength 0.833 T. In this study, a sample of n-type GaAs with a carrier concentration $n = 2.36 \times 10^{18}$ cm^{-3} was characterized for probe wavelengths in the range between 1 and 2.8 microns and for temperatures equal to 100°K and 296°K (see Fig 2.1). Starting from wavelengths above 1.7 μm, the Faraday rotation increases as a square of the probe wavelength, the rotation in this region (corresponds to the energies < 0.75 eV) has been attributed to the free electron in the conduction band transitions (free carriers transitions) that occur in relatively high doped semiconductors.

Typically though, the Faraday rotation in semiconductors is largest in the vicinity of the band edge where there is a rapid change in the dispersion of refractive index. On the same figure 2.1, we start to see the influence of interband transitions which result in the increase of the rotation angle when the probe wavelengths decrease.

Another example of Faraday rotation under the applied magnetic field of 2 T measured on moderately doped GaAs ($n = 3.2 \times 10^{16}$ cm^{-3}) at room temperature and for photon energies above and below the band edge is shown in Fig. 2.2 (Gabriel

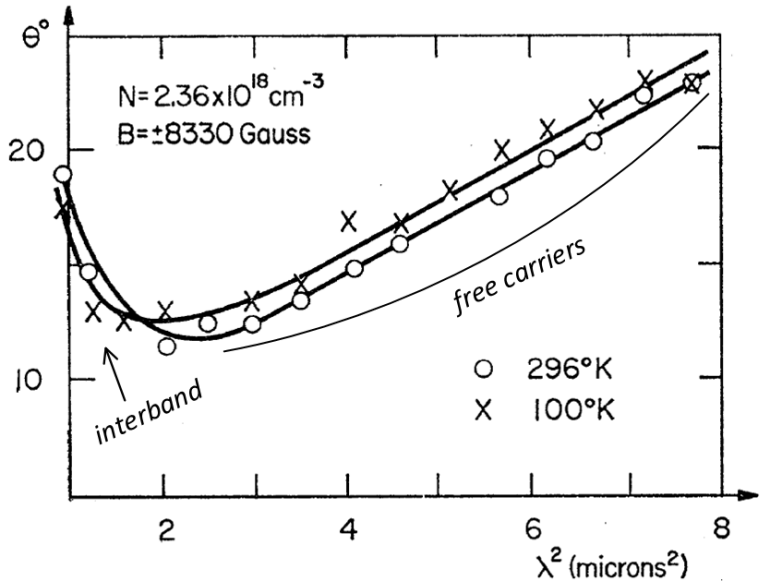

FIGURE 2.1: Faraday rotation angle (in degrees) produced by an n-type GaAs sample ($n = 2.36 \times 10^{18}$ cm^{-3}, $L = 830$ μm) in an external magnetic field of 8330 gauss as a function of the square of the probe wavelength. Adapted from Cardona, 1961.

and Piller, 1967). In this range of photon energies, the main contribution to the Faraday rotation is from the interband transitions. We have added two Y-axes to the original figure from the paper, the Faraday rotation in mrad and the Verdet coefficient axis extracted from the Faraday rotation range, the values of applied magnetic field and the thickness of the sample under study ($L = 32\mu$m). From the Faraday rotation dependence on the photon energy several conclusions can be drawn. First of all, we see that the main singularity in Faraday rotation happens at the energy gap, and corresponds to the rapid change of absorption coefficient. The signal changes sign twice in that small region and attains its maximum and minimum values. Then, the Faraday rotation decreases at both sides of the spectrum. In the last section of Chapter 3 we will describe similar curve and show the functional similarity between the Faraday rotation and the derivative of the absorption coefficient as a function of the probe photon energy.

The two above mentioned experiments are the examples of the classical field-induced Faraday effect which occurs due to the Zeeman splitting of levels in an external magnetic field. On the contrary, in an optically pumped semiconductor experiments there is presumably no band splitting but simply a difference in the density of spin-up and spin-down populations, thus, the refractive index varies much slower with the probe wavelength, which means that we should expect smaller Faraday

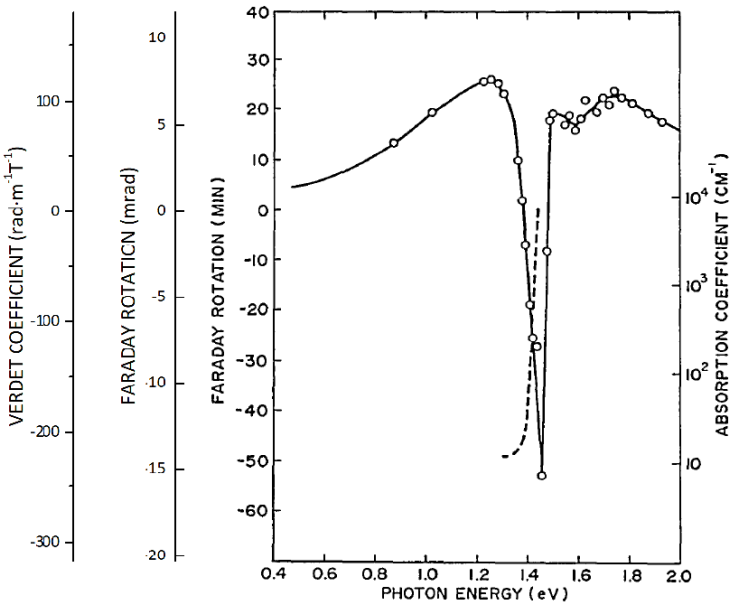

FIGURE 2.2: A spectrum of the Faraday rotation in an n-type ($n = 3.2 \times 10^{16}$ cm^{-3} GaAs crystal. The data are taken with $B = 2$ T (20 kOe) at room temperature. The figure is extracted from Gabriel and Piller, 1967.

rotation angles. Indeed, it will be shown in the course of the work (see Chapter 4) that the depending on the excitation density of the pump, the magnitudes of photo-induced rotation angles are ~ 100 μrad, whereas from the experiments described above typical field-induced rotations are of the order of tens of mrad.

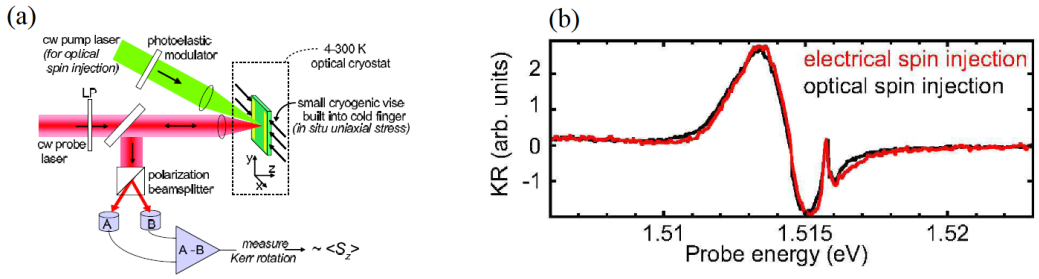

FIGURE 2.3: (a) Kerr rotation microscopy experiment, allowing for imaging electrically and optically injected electron spins in Fe/GaAs devices; (b) Kerr rotation angle dependence on the probe photon energy obtained by means of optical and electrical spin injection into hybrid Fe/GaAs lateral spin transport structures containing 2 μm thick epilayer of Si-doped n: GaAs ($n = 1 - 5 \times 10^{16}$ cm^{-3}) at 4°K (Crooker et al., 2007).

Nevertheless, there is a similarity between the Faraday rotation in the external longitudinal magnetic field and in the optically pumped semiconductors, that can be marked by comparing the previous experiment (Gabriel and Piller, 1967) with an

experiment preformed on 2 μm epilayer of GaAs ($n = 1 - 5 \times 10^{16}$ cm^{-3}) at 4°K by Crooker et al., 2007. The experimental setup as well as the resulting spectrum for the Kerr rotation are described in Fig. 2.3. On the left side of the figure, a schematic of the experimental setup is shown. A 1.58 eV CW pump laser of polarization modulated between σ^+ and σ^- (with a photo-elastic modulator, PEM) is focused to a 4 μm beam spot on the sample, creating the spin polarization. The same is done electrically, via the application of the electrical bias to the Fe contacts. The measurement is conducted at 4°K. The created spin spatial distribution is measured with a linearly polarized tunable Ti:sapphire laser in polar Kerr effect geometry. The rotation of the plane of polarization of the probe light is estimated in arbitrary units with two balanced photo-diodes using lock-in techniques. For each sample studied, the dependencies of the Kerr rotation on the probe energy were measured in order to identify an optimal wavelength resulting in the highest rotations. Such low temperatures result in sharp absorption line-shapes and, thus, larger polarization rotations. Note from Fig. 2.3 (b) that a slight misalignment of the probe wavelength can zero out the signal which is why this wavelength scan is carried out, however, at room temperatures the dependence should soften due to a slower absorption as a function of photon energy.

In the case of optically pumped non magnetic semiconductors the ability of spin-polarized electrons to rotate the polarization plane is no longer characterized by the Verdet constant and the full quantum treatment should be applied to the problem. To our knowledge, there is no established relation between the rotation angles and the created spin density. A group of researches (Giri et al., 2012) has introduced rather attractive concept of Faraday cross section σ_F by analogy with the field induced Faraday effect. According to the authors, the Faraday rotation is linearly dependent on the electron spin density s and on spin polarized area L via proportionality factor σ_F:

$$\theta_F = \sigma_F s L. \tag{2.4}$$

They estimate, for a particular probe photon energy of 18 meV below the band gap and for a doping concentration of 2×10^{16} cm^{-3}, the theoretical value for the Faraday rotation cross section ($\sigma_F = -0.7 \times 10^{-15}$ rad$\times$cm^2) and compare it with a experimental value ($\sigma_F = -(2.5 \pm 0.6) \times 10^{-15}rad\times$cm^2) extracted from combination of independent measurements of photoinduced Faraday rotation and of the

electron spin polarization.

The discussion of the Faraday rotation as a function of the probe photon energy is continued in Chapters 3 for in-field Faraday effect and in Chapter 4 for photoinduced Faraday effect, where the actual experimental data measured on a sample of GaAs are presented.

In the remainder of this chapter we concentrate on the theoretical description of polarization rotation optical detection methods. Polarization rotation measurements have been achieved using a number of optical configurations including a standard linear analyzer, optical bridges (Chang et al., 2011; Li et al., 2014), and modified Sagnac interferometers (Xia et al., 2006). In the following, all three detection schemes will be compared in terms of their ultimate theoretical and practical sensitivities to nanoradian polarization rotations, the analysis of noise sources will be performed and analytical expressions for figures of merit (FOM) for each technique will be given.

2.2 Faraday effect magnetometers studied

In this section the three mentioned detection techniques are going to be presented in details: partially crossed polarizers (PCP), an optical bridge (OB) configuration and a Sagnac interferometer. The theoretical comparison of the three methods is given by deriving analytical expressions for FOM for each technique. The superior performance detection scheme, as it will be shown, is the optical bridge technique, both from the theoretical and practical points of view. While it might seem that complicated in setting up Sagnac interferometer should have a greater performance, it will be shown that it is functionally equivalent to the simplest detection scheme of PCP. Nevertheless, a distinguishing feature of Sagnac interferometer is that it can be reconfigured in different ways to sense different phenomena with particular time and spatial symmetries. The schematic diagrams of various Sagnac interferometer loops are derived from the limitations on the form of Jones' matrices put by the time and spatial symmetries of the chosen medium. The details of the calculations are given hereinafter.

A general description of each technique is given further along with the discussion of main noise sources and derivation of root-mean-squares (RMS), signal-to-noise ratios (SNR) and, subsequently, FOMs are presented with ensuing comparison

of FOMs for PCP, OB and Sagnac interferometer. We assume that the magnetization of the sample along the $\boldsymbol{k}$ vector of light propagation is periodically reversed so that the light is periodically rotated by $\pm\theta_F$. This part of the work is published in Review of Scientific Instruments paper (see Rowe et al., 2017).

2.2.1 Partially crossed polarizers (PCP)

In the first and the most simple experimental technique, so called partially crossed polarizers (PCP), the sample is placed between two almost crossed polarizers: linearly polarized laser and the analyzer (see Fig. 2.4). The analysis is then performed with a half wave plate on a rotation stage that rotates the polarization state of light. Let us define an angle θ with the origin chosen when the polarizers are crossed (*"crossed polarizers condition"*), then according to Malus' law for polarizers, the intensity on the detector is given by

$$I_{det}(\theta) = I_0 \sin^2 \theta, \tag{2.5}$$

with I_0 - initial intensity of the light.

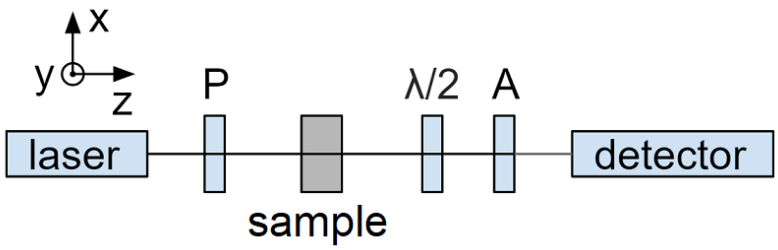

FIGURE 2.4: Schematic of the PCP experiment. Source polarizer is labeled "P", linear analyzer – "A", $\lambda/2$ stands for the half wave plate.

This result can also be deduced using Jones' matrix formalism (Goldstein, 2003), used to describe the transformations in the polarization state of the light in each of the three detection schemes, and particularly useful for the Sagnac interferometer description. According to Jones' matrix calculus, the components of electric field are represented by 2×1 vectors and all the optical components that has some action on the electromagnetic field are described as 2×2 matrices. Applied to the case of PCP here, we can start with defining the electric field emitted by the laser, which has some x and y components E_x and E_y. By convention the wave vector of light is aligned with z direction marked in the Fig. 2.4. The Jones' vector for this field writes

as $\vec{E} = \begin{bmatrix} E_x \\ E_y \end{bmatrix}$, the Jones' matrix for the first polarizer aligned with y-axis ($\mathbf{P}(\pi/2)$), and its operation on the electric field $\vec{E}$ yields:

$$\vec{E_0} = \mathbf{P}(\pi/2)\vec{E} = \begin{bmatrix} 0 & 0 \\ 0 & 1 \end{bmatrix} \begin{bmatrix} E_x \\ E_y \end{bmatrix} = \begin{bmatrix} 0 \\ E_y \end{bmatrix}. \tag{2.6}$$

We define $\vec{E}_0$ as initial electric field of intensity $I_0 = |\vec{E}_0|^2 = |E_y|^2$ especially because the emitted light from the laser is mainly s-polarized.

In the Appendix A general forms of Jones' matrices corresponding to all optical elements used here are given. There we give a generalized form of Jones' matrix for a linear phase retarder $\mathbf{PR}(\phi_x, \phi_y, q)$. Using this notation, the half wave plate whose axis makes an angle $\theta/2$ with the x-axis is represented by matrix $\mathbf{PR}(\pi, 0, \theta/2)$.

When a sample exhibiting the Faraday effect is placed between crossed polarizers this rotates the plane of polarization of light that passes through the sample. A general form of the Jones' matrix describing the polar Faraday effect is (Armitage, 2014):

$$\mathbf{F}(A, B, D) = \begin{bmatrix} A & -B \\ B & D \end{bmatrix}, \tag{2.7}$$

which simplifies in the case of pure rotation to the following form:

$$\mathbf{F}(\theta_F) = \begin{bmatrix} \cos\theta_F & -\sin\theta_F \\ \sin\theta_F & \cos\theta_F \end{bmatrix}. \tag{2.8}$$

The combined action of the sample, the half wave plate and the analyzer aligned with the x-axis (that is perpendicular to the polarizer) is illustrated by writing the following sequence:

$$\begin{aligned} \vec{E}_{det} &= \mathbf{P}(0)\mathbf{PR}(\pi, 0, \theta/2)\mathbf{F}(\theta_F)\vec{E}_0 \\ &= \begin{bmatrix} 1 & 0 \\ 0 & 0 \end{bmatrix} \begin{bmatrix} \cos\theta & \sin\theta \\ \sin\theta & \cos\theta \end{bmatrix} \begin{bmatrix} \cos\theta_F & -\sin\theta_F \\ \sin\theta_F & \cos\theta_F \end{bmatrix} \begin{bmatrix} 0 \\ E_y \end{bmatrix} = \begin{bmatrix} -E_y \sin(\theta - \theta_F) \\ 0 \end{bmatrix} \end{aligned} \tag{2.9}$$

The corresponding intensity on the detector is given by the modulus squared of this vector. In such a way, we find a modified Malus' law for the intensity of light on the detector:

$$I_{det}(\theta) = \vec{E}_{det}^{\top}\vec{E}_{det} = |E_y|^2 \sin^2(\theta - \theta_F) = I_0 \sin^2(\theta - \theta_F) \tag{2.10}$$

The sample introduction has altered the form of the equation 2.5 that can be recovered in the absence of the sample. The intensity on the detectors, without the sample, is minimized for analysis angle $\theta = 0$, in which case the polarizer and the analyzer are crossed.

After introducing the sample with oscillating magnetization, the intensity from Eq. 2.10 is oscillating between $I_{det}(\theta + \theta_F)$ and $I_{det}(\theta - \theta_F)$, and the difference between these two intensities is defined as a magneto-optical (MO) signal, which takes on the following form for small θ_F:

$$\Delta I_{PCP} = I_0\{\sin^2(\theta + \theta_F) - \sin^2(\theta - \theta_F)\} = I_0 \sin 2\theta_F \sin 2\theta. \tag{2.11}$$

There exist different sources of noises that limit the sensitivity of measurements in each of the configurations. An intrinsic photon *shot* noise is always present in experiments with optical detection. It is related to the Poissonian distribution of the arrival times of individual photons at the detector and represents therefore the minimum possible noise with which an optical measurement can be achieved. The RMS shot noise on the magneto-optical signal with PCP is proportional to the square root of the light intensity:

$$N_{PCP,sh} = \sqrt{2I_0\Delta f}\sqrt{\sin^2\theta\cos^2\theta_F + \cos^2\theta\sin^2\theta_F}. \tag{2.12}$$

Another fundamental source of noise is electronic, thermal, or "Johnson" noise that originates from thermal fluctuations of charge carriers in any kind of conductor. The RMS of this kind of noise is independent from light intensity and is measured with the laser switched off. It is desirable to design experiments so that this component is negligible.

Apart from fundamental shot and electronic noises the intensity of the light may fluctuate due to a number of other reasons, including quantum noise associated with the spontaneous emission in the gain medium of the light source, temperature vibrations of the laser cavity, mechanical vibrations of the laser or of the optical components themselves. The resulting RMS source noise is proportional to the intensity of the light via a factor β:

$$\begin{aligned} N_{PCP,so} &= \beta\sqrt{\Delta f}\sqrt{I_{det}^2(\theta + \theta_F) + I_{det}^2(\theta - \theta_F)} \\ &= \beta I_0\sqrt{\Delta f}\sqrt{\sin^4(\theta + \theta_F) + \sin^4(\theta - \theta_F)}. \end{aligned} \tag{2.13}$$

The corresponding shot and source limited SNR are calculated by taking ratio of Eq. 2.11 to Eq. 2.12 or Eq. 2.13, thus giving:

$$SNR_{PCP,sh} = \frac{\sqrt{I_0}\sin 2\theta_F \sin 2\theta}{\sqrt{2\Delta f}\sqrt{\sin^2\theta\cos^2\theta_F + \cos^2\theta\sin^2\theta_F}}, \tag{2.14}$$

and

$$SNR_{PCP,so} = \frac{\sin 2\theta_F \sin 2\theta}{\beta\sqrt{\Delta f}\sqrt{\sin^4(\theta+\theta_F) + \sin^4(\theta-\theta_F)}}. \tag{2.15}$$

2.2.2 Sagnac interferometer

The following experimental setup for measurements of Faraday rotations, considered and implemented in this work, is a modified Sagnac interferometer, schematically depicted in Fig. 2.5. It is a free space static version of Sagnac interferometer based on the work of Kapitulnik, Dodge, and Fejer, 1994. It uses a combination of a polarizer (at angle $\pi/4$ rad to y-axis marked in the figure) and a polarizing beam splitter (PBS) to separate the light into two equal power beams that circulate around the loop and then recombine back at the beam splitter. As opposed to the case of the PCP, the analysis is performed with the help of a variable Faraday rotator instead of the half wave plate. While this configuration does not present sensitivity to just one of four combinations (TP, $\overline{\text{TP}}$, $\text{T}\overline{\text{P}}$, $\overline{\text{TP}}$) of symmetries, the primary function of this component is to set a particular analysis angle, θ. The origin of θ, in analogy with the crossed polarizers condition in PCP, corresponds to the destructive interference of the two beams combined on the detector, the so-called *"dark fringe"* condition.

Using Jones' matrix formalism again, it is possible to describe the evolution of two light components that propagate either in clockwise direction (further on called CW, marked as blue in Fig. 2.5), or in counterclockwise direction (CCW, in red in Fig. 2.5).

We assume, as before, that the initial light polarization emitted by the laser is s-polarized, or polarized along y-direction marked in Fig. 2.5.

The first optical component that the light encounters is a non polarizing 50/50 beam splitter that has the input face marked, and we describe it with 4 Jones' matrices: one for transmission from the input to the output face - **BST**:

$$\mathbf{BST} = \frac{1}{\sqrt{2}}\begin{bmatrix} 1 & 0 \\ 0 & 1 \end{bmatrix}, \tag{2.16}$$

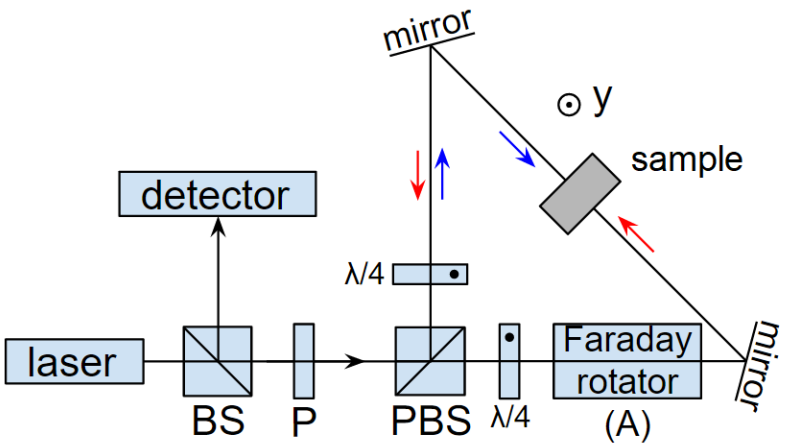

FIGURE 2.5: Schematic of the Sagnac interferometer realized in the work. Designations "P" and "A" stand for linear polarizer and analyzer, similarly to the case of PCP. Beam splitter and polarizing beam splitter are labeled "BS" and "PBS", correspondingly. Two quarter wave plates are marked as $\lambda/4$, the directions of two counter-propagating light beams within the loop are marked with blue for clockwise and red for counterclockwise propagating beams.

whose action on the light is just to halve its intensity. The second matrix is for transmission in the opposite direction, or as we call it, anti-transmission, **ABST**, and as confirmed experimentally, these two matrices are identical, **ABST** = **BST**. The reflection off the beam splitter works as the reflection off a mirror plus it halves the intensity of light, and the corresponding Jones' matrix writes as:

$$\mathbf{BSR} = \frac{1}{\sqrt{2}} \begin{bmatrix} 1 & 0 \\ 0 & -1 \end{bmatrix}. \tag{2.17}$$

Similarly, the last matrix for the light entering from the output face (after completing the Sagnac loop) and reflected towards the detector is named anti-reflection, or **ABSR**, and from the experimental observations, it occurs in anti-phase: **ABSR** $=$ $-$**BSR**.

Next, the polarizer P with its axis rotated by $\pi/4$ rad with respect to the horizontal axis (previously marked as x-axis) has the following Jones' matrix:

$$\mathbf{P}(\pi/4) = \begin{bmatrix} 1/2 & 1/2 \\ 1/2 & 1/2 \end{bmatrix}, \tag{2.18}$$

which can be deduced from the general form given in Appendeix A.

The next optical component and the main component which forms the Sagnac loop is a PBS. It reflects only y-component of the incident light and transmits only

x-component, which results in that its operation is similar to that of polarizer with its axis aligned either with y-direction for the reflection ($\mathbf{P}(\pi/2)$), or with x-direction in transmission ($\mathbf{P}(0)$).

The fast axes of two quarter wave plates ($\lambda/4$ in the figure) are rotated to $\pi/4$ rad with respect to horizontal axis, and the phase shift that is introduced by quarter wave plates by definition is $\pi/2$ rad. In this way we can write the Jones' matrices for the quarter wave plates as $\mathbf{PR}(\pi/2, 0, \pi/4)$.

Although one mirror introduces a π phase shift to one of two orthogonal components of light polarization, when there are even number of mirrors in the loop (for all of geometries considered here there are 2 mirrors in the loop), they do not change the polarization state of light and act as identity matrix.

Both Faraday rotator and the sample introduce some Faraday rotation angle, but the subtle point of this rotation that it changes sign for the beam propagating in the opposite direction, as discussed further in this chapter (see 2.4). With respect to the chosen analysis angle origin, the angle introduced by the Faraday rotator is equal to $\pi/2 - \theta$.

Another important detail to mention is that when the light passes through an optical component via its back face, its Jones' matrix must be transposed (Armitage, 2014). In addition, since the system of coordinates is defined in the reference frame of light, the Jones' matrix for the component under consideration needs to be rotated around y-axis by π radians, which is described by the matrix $\mathbf{Y}_\pi$. If the optical component is reciprocal in space, that results in terms of sort $\mathbf{Y}_\pi^{-1}.\mathbf{P}^T(\pi/4).\mathbf{Y}_\pi$ for the polarizer outside the Sagnac loop taken as an example. For nonreciprocal optical components, such as Faraday rotators, the off diagonal components of the matrix must be reversed. In the case of pure rotation it leads to a simple change of sign of Faraday rotation: $\mathbf{F}(\theta_F) \rightarrow \mathbf{F}(\text{-}\theta_F)$.

Now that we have described and discussed all optical components constituting the Sagnac interferometer setup, we can use the sequences of Jones' matrices to describe the evolution of the CW and the CCW beams:

$$\begin{aligned}\vec{E}_{CW} = \mathbf{ABSR}.\mathbf{Y}_\pi^{-1}.\mathbf{P}^T(\tfrac{\pi}{4}).\mathbf{Y}_\pi.\mathbf{Y}_\pi^{-1}.\mathbf{P}^T(0).\mathbf{Y}_\pi.\mathbf{PR}(\tfrac{\pi}{2}, 0, \tfrac{\pi}{4}).\\ \mathbf{F}(\tfrac{\pi}{2} - \theta).\mathbf{F}(-\theta_F).\mathbf{PR}(\tfrac{\pi}{2}, 0, \tfrac{\pi}{4}).\mathbf{P}(\tfrac{\pi}{2}).\mathbf{P}(\tfrac{\pi}{4}).\mathbf{BST}.\vec{E},\end{aligned} \tag{2.19}$$

where $\vec{E} = \begin{bmatrix} 0 \\ E_y \end{bmatrix}$ as before.

For the light that propagates counterclockwise (CCW), the order of the optical

components is changed, the polarizing matrices responsible for the PBS are different and Faraday rotation sign is reversed:

$$\begin{aligned}\vec{E}_{CCW} = \mathbf{ABSR}.\mathbf{Y}_{\pi}^{-1}.\mathbf{P}^{T}(\tfrac{\pi}{4}).\mathbf{Y}_{\pi}.\mathbf{Y}_{\pi}^{-1}.\mathbf{P}^{T}(\tfrac{\pi}{2}).\mathbf{Y}_{\pi}.\mathbf{Y}_{\pi}^{-1}.\mathbf{PR}(\tfrac{\pi}{2},0,\tfrac{\pi}{4}).\mathbf{Y}_{\pi}.\\ \mathbf{F}(-\tfrac{\pi}{2}+\theta).\mathbf{F}(\theta_F).\mathbf{Y}_{\pi}^{-1}.\mathbf{PR}(\tfrac{\pi}{2},0,\tfrac{\pi}{4}).\mathbf{Y}_{\pi}.\mathbf{P}(0).\mathbf{P}(\tfrac{\pi}{4}).\mathbf{BST}.\vec{E},\end{aligned} \tag{2.20}$$

The resulting interference of the two beams is found by summing up Eq. 2.19 and Eq. 2.20. The modulus square of the resulting Jones' vector arriving at the detector gives:

$$I_{det}(\theta) = \frac{I_0}{8}\sin^2(\theta-\theta_F). \tag{2.21}$$

As this expression is identical in form to Malus' law (Eq. 2.10), the Sagnac interferometer is functionally equivalent to the PCP. Similarly to the PCP case, in the absence of the sample and at analysis angle $\theta = 0$, the intensity on the detector is minimized, which corresponds to the mentioned dark fringe condition. The factor of 8 appears as a result of three 50% power separation on two beamsplitters: first half of power is lost on the beamsplitter before entering the loop, second half is lost at PBS from the two beams completed the loop, and the last half-power is lost on the way to the detector ($2\times2\times2$). Hence factor 8 reduction in MO signal as compared to that in PCP configuration (Eq. 2.11):

$$\Delta I_{Sagnac} = \frac{I_0}{8}\sin 2\theta_F \sin 2\theta. \tag{2.22}$$

Since the RMS source noise is linearly proportional to the intensity of light on the detector, it will also reduce by a factor of 8, so that the source noise SNR won't differ from that in PCP (Eq. 2.15). The shot noise RMS, however, has a square root dependence on the light intensity and will become:

$$N_{Sagnac,sh} = \frac{\sqrt{I_0\Delta f}\sqrt{\sin^2\theta\cos^2\theta_F+\cos^2\theta\sin^2\theta_F}}{2} \tag{2.23}$$

The ensuing shot noise limited SNR in the Sagnac interferometer will be equal to:

$$\mathrm{SNR}_{Sagnac,sh} = \frac{\sqrt{I_0}\sin 2\theta_F\sin 2\theta}{4\sqrt{\Delta f}\sqrt{\sin^2\theta\cos^2\theta_F+\cos^2\theta\sin^2\theta_F}}, \tag{2.24}$$

a factor of $\sqrt{8}$ smaller than that in the PCP. Therefore, if the measurement is shot noise limited, then in the PCP configuration, the SNR will be higher. In the source

noise limited measurement, the two configurations should demonstrate identical performances.

2.2.3 Optical bridge (OB)

The last experimental configuration takes advantage of so-called optical bridge detection system (see Fig. 2.6). The light polarization is now analyzed using a PBS or analagous optical component that separates the Faraday rotated beam into two orthogonal x and y components. Each of the resulting beams impinges onto one of two identical photo-detectors that are connected back-to-back, thereby measuring the difference in intensities of the two beams. Using Jones' matrix formalism, the Jones' vector of the x-component of light is $\mathbf{P}(0).\mathbf{PR}(\pi, 0, \theta/2).\mathbf{F}(\theta_F).\vec{E}$, and the Jones' vector for the y-component is $\mathbf{P}(\pi/2).\mathbf{PR}(\pi, 0, \theta/2).\mathbf{F}(\theta_F).\vec{E}$. The modulus of their difference yields the optical bridge difference signal:

$$I_{bridge} = I_0 \cos 2(\theta + \theta_F). \tag{2.25}$$

From the formula above and in the absence of the sample ($\theta_F = 0$), the signal on the bridge minimizes when analysis angle $\theta = \pi/4$ rad, which is known as *balanced bridge* condition.

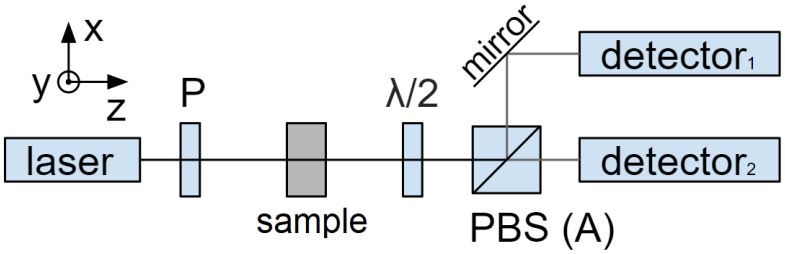

FIGURE 2.6: Schematic of the optical bridge (OB) arrangement. The analyzer in this case is a PBS that separates the beam into two beams of orthogonal polarizations, which are then measured with two matched, back-to-back connected photo-diodes.

As in the cases of the PCP and the Sagnac interferometer, the MO signal is than obtained by taking difference $I_{bridge}(\theta + \theta_F) - I_{bridge}(\theta - \theta_F)$ thus yielding:

$$\Delta I_{OB} = 2I_0 \sin 2\theta \sin 2\theta_F. \tag{2.26}$$

For a fixed Faraday rotation, suppose $+\theta_F$, and so for a fixed moment in time, since laser-related source noise is correlated in each of the two detectors, it is the difference intensity $\Delta I(\theta+\theta_F)$ which is relevant for the source noise calculation rather than the individual intensities on each detector. Still, the noises on the two difference intensities measured at different moments in time, for $+\theta_F$ and $-\theta_F$, are uncorrelated. Thus we write:

$$N_{OB,so} = \beta\sqrt{\Delta f}\sqrt{\Delta I^2(\theta+\theta_F)+\Delta I^2(\theta-\theta_F)} = \beta I_0\sqrt{\Delta f}\sqrt{1+\cos 4\theta_F \cos 4\theta}. \quad (2.27)$$

In contrast to the source noise, the shot noise on each detector is not correlated. The shot noise for a fixed Faraday rotation, $+\theta_F$, is the error propagation sum of the shot noises on each detector:

$$N^{+\theta_F}{}_{OB,shot} = \sqrt{\Delta f}\sqrt{I_0(\cos^2(\theta+\theta_F)+\sin^2(\theta+\theta_F))} = \sqrt{I_0\Delta f}. \quad (2.28)$$

The same result is obtained for a negative Faraday rotation $-\theta_F$, and thus the total shot noise on the MO signal is:

$$N_{OB,shot} = \sqrt{\Delta f}\sqrt{I_0+I_0} = \sqrt{2I_0\Delta f}. \quad (2.29)$$

The source and shot noise SNR are than calculated by taking ratios of Eq. 2.26 to Eq. 2.27 and Eq. 2.29, respectively. This gives:

$$\mathrm{SNR}_{OB,source} = \frac{2\sin 2\theta \sin 2\theta_F}{\beta\sqrt{\Delta f}\sqrt{1+\cos 4\theta \cos 4\theta_F}}, \quad (2.30)$$

and

$$\mathrm{SNR}_{OB,shot} = \frac{\sqrt{2I_0}\sin 2\theta \sin 2\theta_F}{\sqrt{\Delta f}}. \quad (2.31)$$

2.3 Comparison of the theoretical performances of PCP, Sagnac interferometer and OB.

In order to characterize and compare the performances of the considered experimental methods we define a *figure of merit* (FOM) as product of Δf with appropriate squared SNR:

$$\mathrm{FOM} = \Delta f \cdot \mathrm{SNR}^2. \quad (2.32)$$

The total FOM is equal to the reciprocal of the sum of the reciprocals of individual FOM_{source} and FOM_{shot}:

$$\frac{1}{\mathrm{FOM}} = \frac{1}{\mathrm{FOM}_{source}} + \frac{1}{\mathrm{FOM}_{shot}}, \tag{2.33}$$

and is expressed in units of Hz, or s^{-1}.

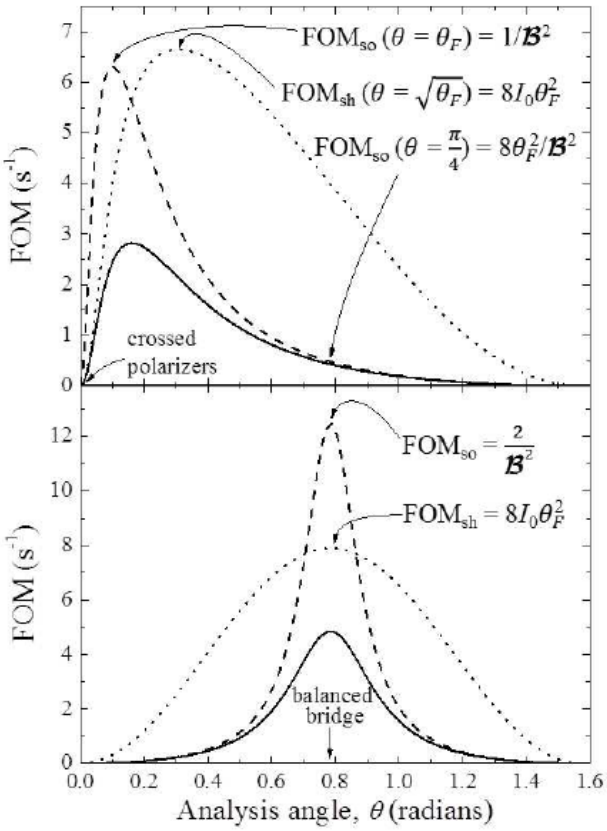

FIGURE 2.7: Figures of merit (FOM) for source noise (dashed lines), shot noise (dotted lines) and total FOM (solid lines) calculated using combination of equations 2.32, 2.14, 2.15, 2.24 ($\times\sqrt{8}$), 2.30, 2.31 and 2.33, by putting $I_0 = 100$, $\beta = 0.4$ and $\theta_F = 0.1$ rad for better comparison. In PCP and Sagnac configurations (top panel), the maximum FOM lies close to crossed polarizer, or dark fringe, condition. However, the FOM_{source} and FOM_{shot} maxima do not appear at the same analysis angle. On the contrary, the OB maximum FOMs (bottom panel) occur at the balanced bridge condition, $\theta = \pi/4$.

Figure 2.7 shows the curves of individual FOMs as well as total FOMs for PCP and Sagnac configurations (top panel) and for the OB configuration (bottom panel). In the calculations, we put $I_0 = 100$, $\beta = 0.4$ and $\theta_F = 0.1$ rad so that FOM_{source} and FOM_{shot} have similar magnitudes for easier comparison of their θ dependencies. The shot noise FOM in the case of PCP and Sagnac maximizes at $\theta = \sqrt{\theta_F}$, whereas the

source noise FOM is maximized for $\theta = \theta_F$. The total FOM maximum lies in the intermediate position, which depends on the relative contributions of source and shot noise FOMs. If one chooses to work in one of these configurations and seek for the position where SNR is maximized, then a preliminary research is required in order to define θ_F that obviously changes from sample to sample, define the optimal θ angle ($\theta \in [\theta_F; \sqrt{\theta_F}]$) and align the analyzer to that position. The additional difficulty might come from the fact that in some samples, such as optically pumped nonmagnetic semiconductors, these angles can be in the nanoradian range and hardly attainable with standard optical components. As a consequence, frequently the analyzer angle is chosen to be equal to $\theta = \pi/4$, where the MO signal is maximized (see Eq. 2.11), but the FOM is lower than its maximum value.

Table 2.1 collects the values of total FOM for the PCP, Sagnac and OB configurations at specific values of analyzer angles, θ, and assuming small Faraday rotation angles $\theta_F \ll 1$. From the table we can see that choosing $\theta = \pi/4$ angle reduces the shot noise limited FOM only by 2, whereas depending on the value of θ_F, an important reduction of source noise limited FOM might occur.

FOM	PCP $\theta = \sqrt{\theta_F}$	Sagnac $\theta = \sqrt{\theta_F}$	PCP $\theta = \theta_F$	Sagnac $\theta = \theta_F$	PCP $\theta = \pi/4$	Sagnac $\theta = \pi/4$	OB $\theta = \pi/4$
Shot	$8I_0\theta_F^2$	$I_0\theta_F^2$	$4I_0\theta_F^2$	$I_0\theta_F^2/2$	$4I_0\theta_F^2$	$I_0\theta_F^2/2$	$8I_0\theta_F^2$
Source	$8\theta_F/\beta^2$	$8\theta_F/\beta^2$	$1/\beta^2$	$1/\beta^2$	$8\theta_F^2/\beta^2$	$8\theta_F^2/\beta^2$	$2/\beta^2$

TABLE 2.1: A comparison of FOM for the three experimental geometries at particular values of the analysis angle, θ. Three values of θ considered, one where shot noise limited FOM is maximized in the case of PCP and Sagnac interferometer, $\theta = \sqrt{\theta_F}$, the second angle is where the source noise limited FOM in the PCP and Sagnac is maximized, $\theta = \theta_F$, and the last one, $\theta = \pi/4$, is where both FOMs are maximized in OB configuration, and where the alignment is simplified for all three techniques.

The lower panel of Fig. 2.7 shows the FOM curves for the case of optical bridge. Remarkably, both noise sources limited FOMs maximize at the same analysis angle position, that corresponds to balanced bridge condition. The maximum source noise FOM for the OB is improved by a factor of $\frac{1}{4\theta_F^2}$ as compared to that for the PCP at $\theta = \pi/4$, a specific characteristic of the OB known as the common mode rejection ratio (CMRR). For this reason, in the OB configuration, a shot noise limited measurement can be achieved even with large light intensities incident on each of the detectors, which is advantageous because of the SNR increases as $\sqrt{I_0}$ in this limit. It should

be noted, however, that the maximum shot noise limited FOM of the optical bridge is exactly equivalent to that obtained in the PCP at $\theta = \sqrt{\theta_F}$.

2.4 Use of Sagnac to differentiate between phenomena of different symmetries

Despite the fact that the Sagnac interferometer configuration has equal or inferior FOM as compared to the PCP and OB techniques, it was nevertheless interesting for us to investigate it in detail. It is usually used to separate the rotations arising due to the Faraday effect, which is a nonreciprocal phenomenon, from those arising due to reciprocal linear birefringence (Spielman et al., 1990). This still can be achieved with other, one path techniques such as PCP or OB, but it would require at least two separate measurements, where, for example, the sample is measured once and then remeasured after π rotation around an axis perpendicular to the light propagation direction. Such separated in time measurements are usually hard to achieve under the exact same experimental conditions, or with the sample which is spatially inhomogeneous. The two path nature of Sagnac interferometers guarantees that the same part of the sample is sensed, since the collinearity of clockwise and counterclockwise propagating beams is ensured by the interference on the detector.

The well-known ability of Sagnac interferometers to distinguish nonreciprocal rotations can be intuitively understood from the the following. Let's take a plane wave traveling in the $+z$-direction, whose electric field can be expressed like $\vec{E} = \vec{E}_0 e^{i(kz-\omega t)}$, and 'reverse' time. This can be accomplished by simply putting $t \to -t$, and the electric field will take form $\vec{E}_0 e^{i(kz+\omega t)}$. The same result can be obtained by the combination of complex conjugation of the amplitude and reversal of the wave vector direction $k \to -k$. That means that, to within a complex conjugation operation, in the Sagnac interferometer, having the CW and CCW beams travel in opposite directions is equivalent of time reversing one of them.

Another ability of Sagnac interferometers is to distinct spatially symmetric from antisymmetric phenomena. Practically, it means that the rearrangement of optical components within the Sagnac loop affects the end result. That applies to a single element if it is not symmetric in space. In other words, if the sample consists of two different plates separated by xy-plane, then the two counter-propagating beams will

sense the sample differently which will change the interference pattern for specifically designed loops. The term "parity" here relates to the inversion operation along the z-direction (normal to the sample plane), or the xy mirror symmetry operation.

A phase shift between two orthogonal components of light may occur not only due to Faraday effect, but during transmission through a number of materials according to the symmetries of their electronic structures. The combinations of two fundamental symmetries – space symmetry, or parity (P) and time reversal symmetry[1] (T) – include:

- TP symmetry, i.e. time and space symmetric, for example, polarization rotations due to linear birefringence;
- $\overline{\text{TP}}$ symmetry, i.e. nonreciprocal and space asymmetric, that is peculiar to magnetoelectric materials;
- $\text{T}\overline{\text{P}}$ symmetry, i.e. reciprocal, but space asymmetric, that is intrinsic to chiral materials;
- and $\overline{\text{T}}\text{P}$, i.e. nonreciprocal but space symmetric, which is the symmetry of Faraday effect occurring in magnetized media.

Further on we present the examples of several Sagnac modifications modeled by performing Jones' calculus on the set of general matrices for each of four symmetries, with measured signals being dependent on only one of four effects. The four different configurations are shown in Fig. 2.8. Up-to-date the only type of Sagnac interferometer developed and used to discriminate between $\overline{\text{T}}\text{P}$ and TP symmetries (Spielman et al., 1990) is a variation of a scheme presented in Fig. 2.8(a).

In order to, first of all, find and then confirm sensitivity to only one at a time of four symmetric phenomena we have relied on the Jones' calculus and examined the advancement of each of the two counter-propagating beams (CW and CCW), same as we did for the actual Sagnac configuration assembled for the comparison of three detection schemes in the previous sections.

We start by listing general forms of 2×2 Jones' matrices for TP (from parity symmetry constraints), $\overline{\text{TP}}$ (a general form of the matrix is given in Mahmood and Zhao,

[1]Here we neglect the presence of dissipation processes and are only interested in time reciprocity concept: "A system may be reciprocal if one can switch source and detector... and get the same result" (Armitage, 2014).

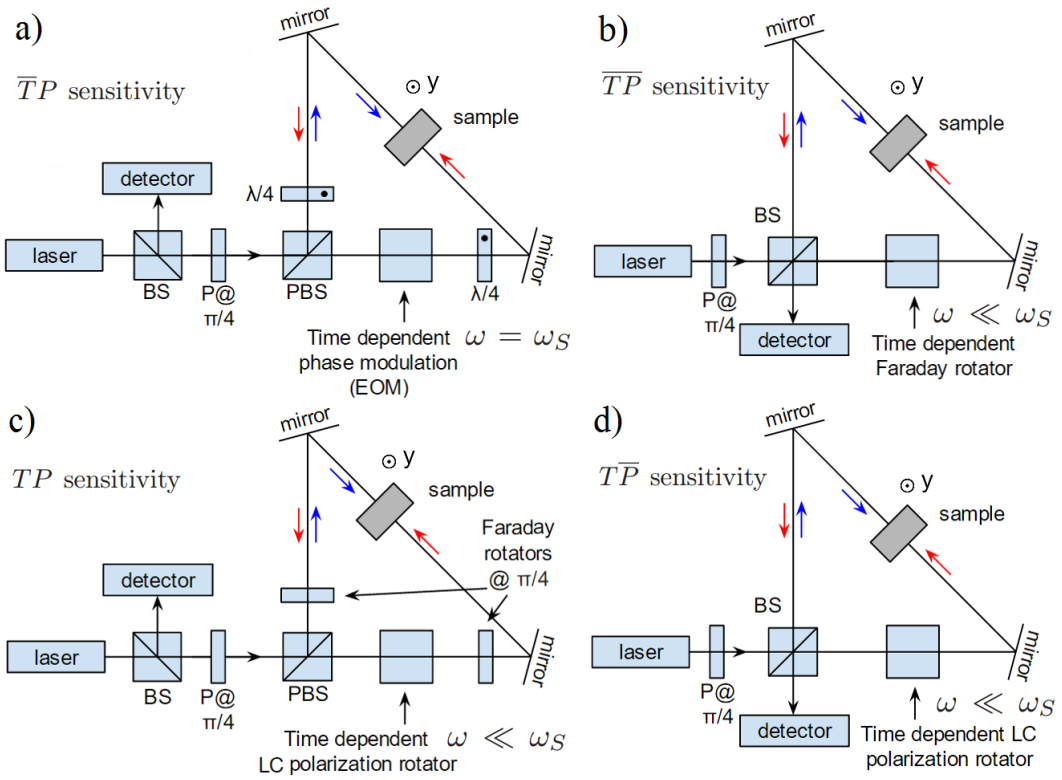

FIGURE 2.8: Four Sagnac interferometer geometries, each sensitive only to polarization rotations of a particular symmetry: (a) $\overline{\text{T}}\text{P}$ symmetry sensitive (analogous to the one used by Xia et al., (b) $\overline{\text{TP}}$ symmetry sensitive, (c) TP symmetry sensitive and (d) $\text{T}\overline{\text{P}}$ symmetry sensitive geometries. Designations for the optical components used are similar to those in the case of practically implemented Sagnac (see Fig. 2.5). An angle that the fast axis of the polarizer P makes with the horizontal axis is marked (and equal to $\pi/4$ everywhere). As opposed to the Sagnac interferometer used for the experiments, here the analyzers are time modulated.

2015), $\overline{\text{T}}\text{P}$ and $\text{T}\overline{\text{P}}$ symmetric phenomena and assign them for the CW propagating beam:

$$\mathbf{M}_{TP} = \begin{bmatrix} A & B \\ B & D \end{bmatrix}; \quad \mathbf{M}_{\overline{TP}} = \begin{bmatrix} A & B \\ B & D \end{bmatrix}; \quad \mathbf{M}_{T\overline{P}} = \begin{bmatrix} A & B \\ -B & D \end{bmatrix}; \quad \mathbf{M}_{\overline{TP}} = \begin{bmatrix} A & B \\ -B & D \end{bmatrix}. \tag{2.34}$$

In the opposite direction, i.e. for the CCW propagating beam, the transformed matrices become

$$\hat{\mathbf{M}}_{TP} = \begin{bmatrix} A & -B \\ -B & D \end{bmatrix}; \quad \hat{\mathbf{M}}_{\overline{TP}} = \begin{bmatrix} A & B \\ B & D \end{bmatrix}; \quad \hat{\mathbf{M}}_{T\overline{P}} = \begin{bmatrix} A & -B \\ B & D \end{bmatrix}; \quad \hat{\mathbf{M}}_{\overline{T}P} = \begin{bmatrix} A & B \\ -B & D \end{bmatrix}. \tag{2.35}$$

which were found by transforming them in the basis of the CCW beam. Important would be to remark that these matrices are written in the reference frame of each of the beams, and they have to be converted into laboratory frame for the calculations. Note also that as a result of this transformation the matrices corresponding to the effects which are nonreciprocal have not changed their forms. These matrices will be used in the calculation of the responses of each of the configuration to the four different symmetric effects.

Figure 2.8 includes schematics for the modeled Sagnac modifications: (a) configuration for sensitivity to $\overline{\text{T}}\text{P}$ symmetry only, similar to the one used by Kapitulnik, Dodge, and Fejer, (b) for $\overline{\text{TP}}$ symmetry sensitivity, (c) for sensitivity to TP symmetry and the last configuration (d) is sensitive to $\text{T}\overline{\text{P}}$ symmetric effects only. As a matter of fact, the Sagnac interferometer configuration used in our experiments (see Fig. 2.5) is not purely magnetic effects sensitive ($\overline{\text{T}}\text{P}$ symmetry), it is, in fact, sensitive to all types of rotations. In order for our Sagnac loop to be able to be sensitive to magneto-optical effects only, an electro-optic modulator (EOM) must be added at one end of the loop (Kapitulnik, Dodge, and Fejer, 1994; Fried, Fejer, and Kapitulnik, 2014, as on Fig. 2.8 a), so that it introduces a time dependent phase shift according to:

$$\phi(t) = \phi_0 \sin \omega t, \text{ where } \omega = \pi / T_S = \omega_S, \tag{2.36}$$

and T_S is the time it takes for light to travel around the loop. The choice of modulation frequency is strict in this case $\omega = \omega_S$, and in order to keep the modulation frequency in the MHz range (supported by commercial EOMs) the loop has to be fibered and of several hundred meters long to increase the period T_S. The Jones' matrix of the EOM is that of a standard linear phase retarder, $\mathbf{PR}(\phi(t),0,0)$ with its axes aligned with x and y axes. In this way, the CW propagating beam that encounters the EOM at a time $t = t'$, will sense a phase lag of $\phi_0 \sin \omega_S t'$, and the CCW beam at the EOM position will experience a phase of $\phi_0 \sin \omega_S (t' + T_S) = -\phi_0 \sin \omega_S t'$.

The calculation procedure is similar to the one used for the description of static Sagnac interferometer: for a sample that induces a Faraday rotation θ_F, we can write the sequences of Jones' matrices similar to Eq. 2.19 and Eq. 2.20, where the constant analysis angle θ is replaced by $\phi_0 \sin \omega_S t$, and this would yield the detected intensity that is similar to that in Eq. 2.21. Importantly, further, the harmonic analysis of this time dependent signal is conducted and the resulting DC, first harmonic (ω) and second harmonic (2ω) components are given in Table 2.2 for a general case using matrices from Eqs. 2.34 and 2.35. In the table, $J_0(\psi)$, $J_1(\psi)$ and $J_2(\psi)$ stand for Bessel functions of zero, first and second order, respectively. It should be noted that the intensity on the detector itself is non-zero for all of the symmetries in each Sagnac configurations. However, by taking a look at the first harmonic column in the Table 2.2, it is this component that is sensitive to only one particular symmetry, therefore the signal-to-measure has to be proportional to the first harmonic. Further, by dividing the ω component of the measured intensity by the 2ω component, we can conveniently get rid of the laser intensity, i.e. normalize the signal, and in the case of pure Faraday rotation ($A = D = \cos\theta_F, B = \sin\theta_F$) that yields the following ratio:

$$\frac{-I_0 \sin 2\theta_F J_1(2\phi_0)/2}{I_0 \cos 2\theta_F J_2(2\phi_0)/2} = \tan 2\theta_F \frac{J_1(2\phi_0)}{J_2(2\phi_0)}. \tag{2.37}$$

In such a way, the Faraday rotation angle can be extracted from the ratio of two signals at frequencies ω and 2ω. This is an example of Phase Generated Carrier technique (PGC), introduced by Dandridge, Tveten, and Giallorenzi, 1982. It should be also mentioned that the DC components of the detected intensity are non-zero in all cases, meaning that the modulation of the signal is crucial for distinguishing between time and parity symmetries of the polarization rotation.

The differences between this and the other three Sagnac configurations are in the nature of the modulator as well as in the frequency of that modulation. In contrast to $\overline{\text{T}}$P case, the other configurations require that the modulation frequency lies in the static limit, where $\omega \ll \omega_S$. In the $\overline{\text{TP}}$ loop, the slow modulation has to be of $\overline{\text{T}}$P symmetry, which can be achieved with a TGG rod placed in a solenoid. Recall that the Jones' matrix for pure Faraday rotation is given by $\mathbf{F}(\phi_0 \sin \omega t)$ for the CW beam and by $\mathbf{F}(-\phi_0 \sin \omega t)$ for the CCW beam according to Eq. 2.8.

In the Sagnac loops sensitive to TP and T$\overline{\text{P}}$ symmetries, time dependent liquid crystal (LC) rotators can be used as modulators. The LC rotators are chiral objects, so

	DC	ω	2ω
Fig. 2.8(a)			
TP	$I_0(A+D)^2(1+J_0(2\phi_0))/16$	0	$I_0(A+D)^2J_2(2\phi_0)/8$
$\overline{\text{TP}}$	$I_0(A+D)^2(1+J_0(2\phi_0))/16$	0	$I_0(A+D)^2J_2(2\phi_0)/8$
$\overline{\text{T}}$P	$I_0\big((A+D)^2+4B^2+((A+D)^2-4B^2)J_0(2\phi_0)\big)/16$	$-I_0B(A+D)J_1(2\phi_0)/2$	$I_0\big((A+D)^2-4B^2\big)J_2(2\phi_0)/8$
T$\overline{\text{P}}$	$I_0(4B^2+(A+D)^2)(1+J_0(2\phi_0))/16$	0	$I_0\big((A+D)^2+4B^2\big)J_2(2\phi_0)/8$
Fig. 2.8(b)			
TP	$I_0\big(4B^2+(A-D)^2\big)(1-J_0(2\phi_0))/16$	0	$-I_0(4B^2+(A-D)^2)J_2(2\phi_0)/8$
$\overline{\text{TP}}$	$I_0\big((A-D)^2+4B^2-((A-D)^2-4B^2)J_0(2\phi_0)\big)/16$	$I_0B(D-A)J_1(2\phi_0)/2$	$-I_0\big(-4B^2+(A-D)^2\big)J_2(2\phi_0)/8$
$\overline{\text{T}}$P	$I_0(A-D)^2(1-J_0(2\phi_0))/16$	0	$-I_0(A-D)^2J_2(2\phi_0)/8$
T$\overline{\text{P}}$	$I_0\big(8B^2-(D-A)(A+4B-D)(1+J_0(2\phi_0))\big)/16$	0	$I_0(D-A)(A+4B-D)J_2(2\phi_0)/8$
Fig. 2.8(c)			
TP	$I_0\big((A-D)^2+4B^2-((A-D)^2-4B^2)J_0(2\phi_0)\big)/16$	$I_0B(D-A)J_1(2\phi_0)/2$	$-I_0\big((A-D)^2-4B^2\big)J_2(2\phi_0)/8$
$\overline{\text{TP}}$	$I_0(A-D)^2(1-J_0(2\phi_0))/16$	0	$-I_0(A-D)^2J_2(2\phi_0)/8$
$\overline{\text{T}}$P	$I_0(-A+2B+D)^2(1-J_0(2\phi_0))/16$	0	$-I_0(-A+2B+D)^2J_2(2\phi_0)/8$
T$\overline{\text{P}}$	$I_0(A-D)^2(1-J_0(2\phi_0))/16$	0	$-I_0(A-D)^2J_2(2\phi_0)/8$
Fig. 2.8(d)			
TP	$I_0(A+D)^2(1-J_0(2\phi_0))/16$	0	$-I_0(A+D)^2J_2(2\phi_0)/8$
$\overline{\text{TP}}$	$I_0\big(8B^2+(A+D)(A+4B+D)(1-J_0(2\phi_0))\big)/16$	0	$-I_0(A+D)(A+4B+D)J_2(2\phi_0)/8$
$\overline{\text{T}}$P	$I_0(4B^2+(A+D)^2)(1-J_0(2\phi_0))/16$	0	$-I_0(4B^2+(A+D)^2)J_2(2\phi_0)/8$
T$\overline{\text{P}}$	$I_0\big((A+D)^2+4B^2-((A+D)^2-4B^2)J_0(2\phi_0)\big)/16$	$I_0B(A+D)J_1(2\phi_0)/2$	$-I_0\big((A+D)^2-4B^2\big)J_2(2\phi_0)/8$

TABLE 2.2: Harmonic components of the intensity signal on the detector for each of the four Sagnac configurations presented in Fig. 2.8 calculated for each of the four phenomena of different symmetry.

they have $\overline{\mathrm{TP}}$ symmetry with a general form of Jones' matrix given in Eq. 2.34 by $\mathbf{M}_{\overline{\mathrm{TP}}}$ with $A = D = \phi_0 \sin \omega t$ and $B = \phi_0 \cos \omega t$. However, so far commercially available LC rotators cannot provide a sinusoidal modulation of a polarization rotation, but a square wave modulation. This complicates the calculations, but the functionality of the Sagnac loops in Fig. 2.8 (c and d) can still be achieved.

Apart from the modulator part, the positions of the detector and all the other optical components constituting the loops are important too, although the connection between the symmetry and the positions of the optical components with the final result is not completely clear yet.

It is worthful to mention that the presented configurations of Sagnac loop are not the only possible configurations allowing the exclusive sensitivity to one of the four symmetries. Here we show an example of another geometry that is sensitive to $\overline{\mathrm{TP}}$ symmetry only, see Fig. 2.9. Unlike the first configuration requiring high modulation frequencies in the MHz range, and therefore, a fibered loop of several hundred meters that might be more difficult to work with, this second solution works with a slowly modulated Faraday rotator and thus can be assembled in free space.

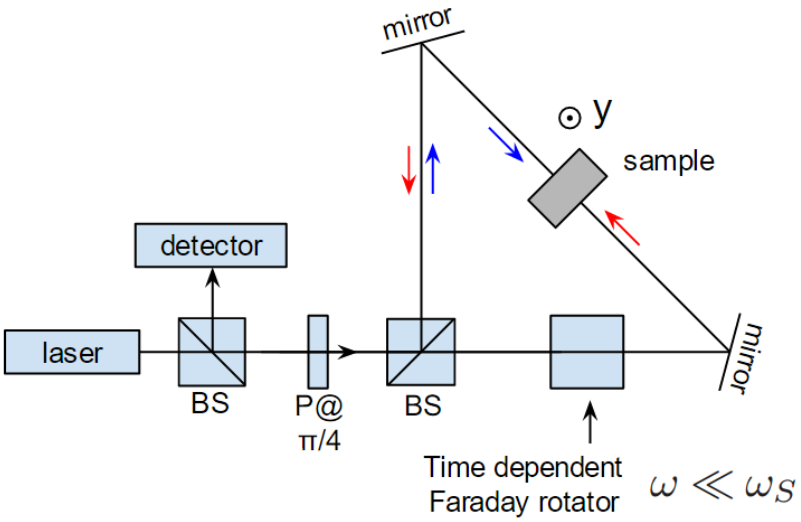

FIGURE 2.9: Another possible Sagnac configuration that is sensitive to $\overline{\mathrm{TP}}$ symmetric effects only, similar to that in Fig. 2.8(a).

The validity of theoretical expressions is confirmed in Chapter 3 by performing a Faraday rotation measurement on :

- a magnetic sample consisted of thin gold and cobalt layers Au/Co(4 nm)/Au grown on a diamagnetic quartz substrate;

- a terbium gallium garnet (TGG) rod exposed to a small, time varying axial magnetic field. This material has been chosen for its high rotatory powers, and Verdet constants reaching -134 rad/(T·m) for 632 nm probe light wavelengths.

Chapter 3

Field-induced Faraday effect measurements

In the course of the thesis, the performances of the PCP and OB configurations were tested first on a ferromagnetic thin film of Au/Co(4 nm)/Au grown on a diamagnetic quartz substrate. The second set of experiments was conducted on a paramagnetic crystal of terbium gallium garnet (TGG), and all three detection schemes (PCP, Sagnac and OB) were implemented. The details of the experimental setups, as well as the results are given in the first two sections of this chapter. In the final section, the chosen detection method, the optical bridge, has been tested in a sample of unintentionally doped GaAs in external magnetic field, and the dependence of this classical Faraday rotation, and deduced Verdet coefficient, on the probe wavelength has been studied experimentally.

3.1 Test of sensitivities on Au/Co/Au multilayers

Figure 3.1 shows the top view of experimental setup in its final state. The main components of the setup are a diode laser of wavelength 780 nm and maximum power of 10 mW, a polarizer, a system of two electromagnets with a ferromagnetic sample placed between them, a half-wave (HW) plate, a polarization beam-splitter and two Si PIN photodiodes (Hamamatsu S3399, sensitivity at 780 nm = 0.45 A/W). The output current passes through a variable gain (1 MΩ, 10 MΩ or 100 MΩ) amplifier, and the final output voltage, amplified by an additional factor of 10, is measured using a commercial, 16-bit data acquisition card. The bandwidth of the amplifier is gain dependent and, for the three gains mentioned here, is equal to 930 Hz, 900 Hz and 235 Hz, respectively. The whole setup is enclosed by a foamed plastic box, that

is suspended in order to be free from the influence of mechanical oscillation of the building.

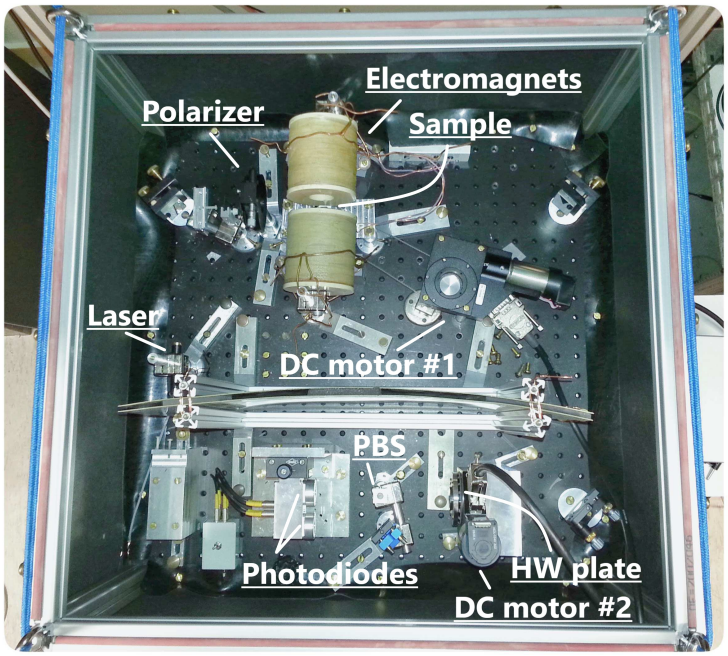

FIGURE 3.1: A photograph of the experimental setup. The transformation from the OB to the PCP configuration is made by shielding one of the detectors.

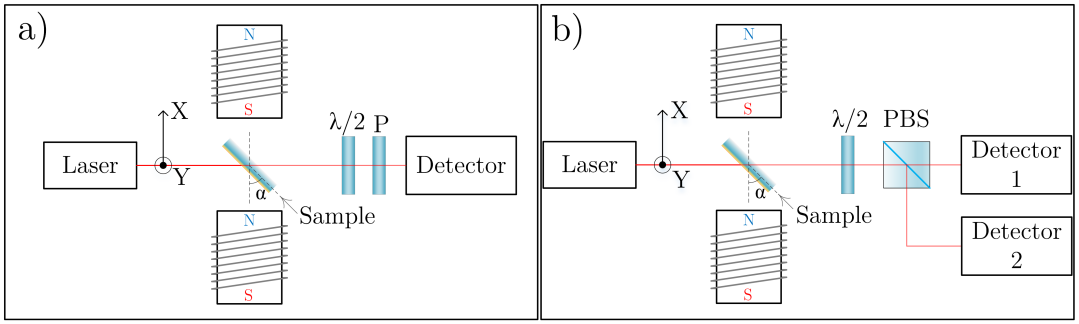

FIGURE 3.2: Schemes of the two experimental setup configurations: (a) PCP. The laser light is s-polarized (‖Y), the analyzer (P) axis is along X and the HW plate (marked as $\lambda/2$) is used to rotate the transmitted polarization. (b) Optical bridge: a PBS is introduced to separate X and Y components of transmitted polarization, whose intensity is then measured individually using two equivalent photodiodes.

Schematics of the two configurations (PCP and OB) are presented in Fig. 3.2. In both cases, the laser light gets polarized along y axis according to the coordinate system shown with the help of the polarizer. Afterwards, within the sample under applied magnetic field (via electromagnets), the polarization is rotated due to the Faraday effect. The magnetic sample made of a thin ferromagnetic layer with

slightly out-of-plane magnetization, can be rotated along its vertical by an angle α, where $\alpha = 0$ corresponds to normal incidence of the laser beam. The sample rotation is achieved with the help of a DC motor, that is marked in Fig. 3.1 as DC motor # 1. After the sample, the HW plate is mounted on the second DC motor (# 2 in Fig. 3.1) that rotates it thereby changing the analysis angle θ. The PBS is mounted next on the beam path and it is used to separate the s- and p- components of light polarization and send them on the two photodiodes, that are connected back-to-back in an earthed, shielded box.

Effect of the sample rotation on Faraday angle.

The sample chosen for experimental confirmation of theoretical dependencies of SNR and RMS for PCP and OB is an Au(5 nm)/Co(4 nm)/Au(20 nm) multilayer thin film which presents an out-of-plane easy axis for the magnetization oriented at an angle γ with respect to the plane of the sample. The MO properties of the sample have been thoroughly studied in Kerr geometry (Hermann et al., 2001). The coercive field is sufficiently low, of the order of 15 mT, that is easily accessible with a pair of closely spaced air-core coils to which an alternating sinusoidal current is applied. The coil axis, and hence the direction of the applied magnetic field, is placed at right angles to the wave vector of the probe beam, and the sample makes an angle α with the direction of the magnetic field.

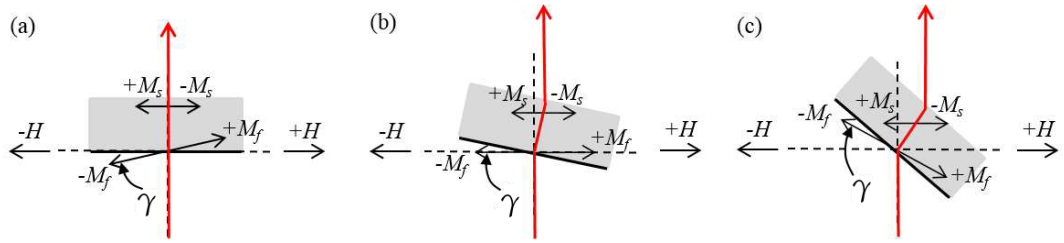

FIGURE 3.3: Schematic representation of sample rotations. The thin film magnetization M_f is inclined at a small angle γ with respect to the sample plane, the magnetization of the diamagnetic quartz substrate M_s is oppositely proportional to the magnetic field. (a) At $\alpha = 0$, the laser beam is not deflected and, therefore, there is no magneto-optical response from the substrate. For non-zero γ, the $\pm M_f$ components along the wave vector $\vec{k}$ (red line) are non-equal and the signal in a form of hysteresis loop can be measured. (b) When the sample is rotated so that $\alpha = \gamma$, the magnetization of the film is perpendicular to the wave vector and does not contribute to the total magneto-optical contrast, whereas now oscillating with the field M_s has parallel to k component within the substrate that is registered as a linear dependence. (c) At $\alpha = \pi/4$ rad both thin film and substrate magnetizations contribute to magneto-optical contrast resulting in tilted hysteresis loops.

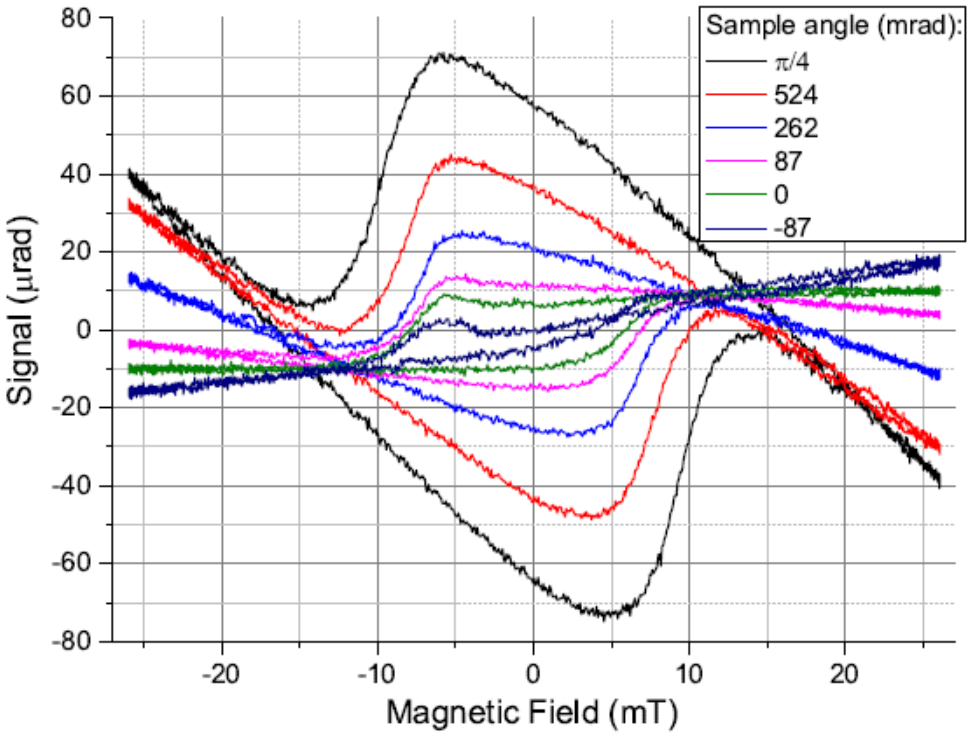

FIGURE 3.4: Experimental data showing the effect of sample rotation. MO contrast reduces from $\theta_F \sim 130$ μrad to $\theta_F \sim 5$ μrad when the sample angle α approaches the angle β of the film magnetization inclination. Diamagnetic response of the quartz substrate adds a linear background slope that vanishes at $\alpha = 0$, i.e. at normal incidence.

The ferromagnetic sample presents a slightly out-of-plane magnetization M_f that forms an angle γ with the sample plane as shown in Fig. 3.3. The diamagnetic response of the substrate M_s is probed only in case of non-perpendicular propagation of the light within the sample that occurs due to refraction at the sample/air interface. Fig. 3.3 qualitatively explains the variation of θ_F as a function of the sample rotation angle α, while Fig. 3.4 provides the experimental proof of that explanation.

At $\alpha = 0$, as in Fig. 3.3 (a), the light beam is not refracted and the magnetization of the diamagnetic quartz substrate is always perpendicular to light propagation wave vector $\vec{k}$, so that the Faraday rotation induced by the substrate is zero. This corresponds to the green curve in Fig. 3.4: it has no negative background slope and a hysteresis loop with non-zero opening showing the existence of a component of thin film magnetization aligned along the $\vec{k}$ vector.

When $\alpha = \beta$, Fig. 3.3 (b), the external magnetic field is aligned with the film magnetization and its components along $\vec{k}$ are zero for both $\pm H$. Here then the MO response (the opening in the hysteresis loop at H = 0) tends towards zero. This occurs for sample rotation angles lying $\alpha \in (-130; -87)$ mrad. Thus the direction

of the easy axis relative to the plane of the sample can be estimated in this way. At this angle, the substrate magnetization, $\pm M_s$, now has non-zero components along $\vec{k}$ and the diamagnetic response of the quartz substrate is presented as a negative slope in the saturation region of the hysteresis curve.

At $\alpha = \pi/4$ rad, both the substrate and the magnetic thin film contribute to the MO response, and since the projections of $\pm M_f$ on $\vec{k}$ are now significantly larger, the rotation angle is also much larger (reaches ~ 130 μrad for the curve with largest opening corresponding to $\alpha = \pi/4$ rad in Fig. 3.4). Rotations of the sample in the probe beam and relative to $\pm H$ are therefore useful in benchmarking the sensitivity of the experiment since θ_F can be continuously varied.

Experimentally, the MO contrast was defined as the voltage difference at $H = 0$ corresponding to the difference between two remnant magnetization states. The noise on each measurement was calculated as standard deviation of the signal from its mean value (that is RMS), and so the SNR were found by taking ratios of MO signals to their noise levels.

Next, the experimentally obtained MO signal and RMS noise dependences on the analysis angle θ are presented in Fig. 3.5 for PCP and OB configurations. The experimental conditions in the PCP arrangement were as follows: the laser power after the sample equal to 12 μW, effective bandwidth of Δf = 93 Hz and $\alpha = \pi/6$. Both $\Delta I/2I_0$ and $N/2I_0$ dependencies are in good agreement with theoretical predictions. From the MO contrast curve (left panel of Fig. 3.5, a) the Faraday rotation angle can be deduced, and in this case it is equal to $\theta_F \approx 120$ μrad. The experimental noise θ dependence can be fit by θ dependence of the source noise described with Eq. 2.13 away from the optimal conditions ($\theta \gg \theta_F$), and so the fitted β factor is calculated to be equal to 2.4×10^{-5}. Meanwhile for $\theta \in [0; 0.15]$ rad the measurement is limited by non optical electronic noise, measured on the signal in the dark. The MO contrast and noise θ dependencies were taken with $I_0 = 1.1\times10^{13}$ photons/s. In the right panel of the Fig. 3.5 one can see that at such photon fluxes and for a fixed analysis angle θ = 0.14 rad, indeed, the measurement is dominated by electronic noise, whereas when the intensity of probe light is increased, the RMS noise varies linearly with intensity as expected for the source noise. The important conclusion to draw is that unless the electronic noise is significantly reduced, the shot noise limited measurement is not possible with the PCP.

A similar set of graphs: MO contrast (left) and RMS noise (middle) analysis angle

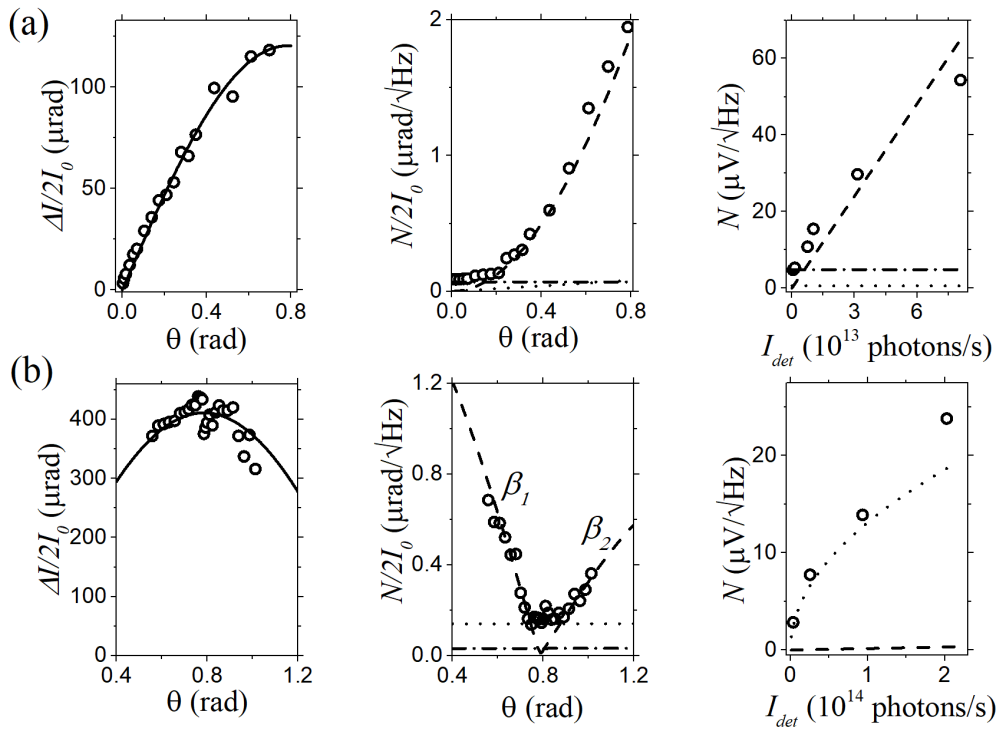

FIGURE 3.5: Experimental results obtained using (a) the PCP and (b) the OB arrangements. The left panels show the measured MO contrast (open circles) dependencies on the analysis angle θ along with theoretical fits using corresponding equations for ΔI. The experimental RMS noise (open circles) dependencies on θ are shown in middle panels with the source (dashed lines), the shot (dotted lines) and the electronic (dash-dotted lines) noise dependencies. The right panels show the intensity on the detectors dependencies of the experimental noise, revealing the source noise (dashed line, linear I_{det} dependence) limited measurement in the case of the PCP, and the shot noise (dotted line, square root variation with I_{det}) limited measurement in the OB configuration.

dependencies, and RMS noise as a function of light intensity (right), is presented for the OB in Fig. 3.5, b. The laser power is equal to 56 μW, Δf = 99 Hz, and sample rotation angle that maximizes the signal ($\alpha = \pi/4$) rad is chosen in this case. The MO signal is fitted with sin(2θ) function and the Faraday rotation angle is calculated from the fit: $\theta_F \approx 205$ μrad. Looking now at the RMS noise graph, the electronic noise is the least important in the case of large intensity on both detectors, and therefore, a measurement limited by optical noise is possible in such case. In addition, because of the differential nature of the detection, the source noise minimizes at the optimal analysis angle (common mode rejection), as can be seen from the figure. As a result, in the vicinity of $\pi/4$ rad angle, the measurement that is shot noise limited is achieved. This is confirmed by studying the intensity variation of the RMS noise at

$\theta = \pi/4$ rad as shown in the right panel of Fig. 3.5 (b). The characteristic square root variation of the RMS is obtained, as expected for shot noise. As θ shifts away from $\pi/4$ rad the correlated source noise from the laser no longer has the same amplitude on each detector and is therefore no longer reduced by the CMRR. Indeed at $\theta = 0$ or $\theta = \pi/2$ rad, one recovers the full RMS source noise on one of the detectors. Thus for some analysis angle $\theta \neq \pi/4$ rad (whose value depends on β) the measurement becomes source noise limited. Using the expected variation (see Eq. 2.27), it is possible to estimate β.

For analysis angles $\theta < \pi/4$ rad the source noise matches experimental data for $\beta = \beta_1 = 2.4 \times 10^{-5}$, the same value as in the PCP measurement. However for $\theta > \pi/4$ another value of $\beta = \beta_2 = 1 \times 10^{-5}$ fits the experimental data better. This suggests that during the sequence of measurements where the analysis angle was varied from 0 to $\pi/2$, the value of β coefficient has dropped. This is consistent with the fact that the laser used here is a non temperature controlled model that is subject to occasional jumps in power or polarization due to mode hopping or some analogous phenomenon.

Finally, the performance of the PCP and OB configurations is demonstrated with a hysteresis loop taken with different experimental configurations: the OB with $\theta = \pi/4$ rad, the PCP with the optimum analysis angle $\theta = 52$ μrad, and with more commonly used PCP configuration with $\theta = \pi/4$ in Fig. 3.6.

The transition between the OB and the PCP for the same analysis angle $\theta = \pi/4$ in practice can be simply obtained by blocking one of the detectors. The effect of this action is remarkable: the RMS noise value ascends from 30 nrad $/\sqrt{\text{Hz}}$ for the OB to 340 nrad$/\sqrt{\text{Hz}}$ for the PCP, which can be noted by comparing plots with $\pi/4$ analysis angle in the Fig. 3.6. This is an excellent demonstration of the ability of the optical bridge to reject the common mode (optical source) noise, which suddenly appears in the measurement with a single detector.

The prior investigation of the noise sources and the MO signals helped us in the identification of the optimal sample-dependent analysis angle for the PCP configuration under this particular experimental conditions, $\theta = 52$ μrad. This angle corresponds to the electronic noise limited measurement and so it is not an optimal optical noise limited angle described in the theoretical calculation earlier (see Chapter 2), nevertheless the value of the RMS noise (55 nrad$/\sqrt{\text{Hz}}$) is comparable with that in the balanced optical bridge. The similarity of performances given by the OB

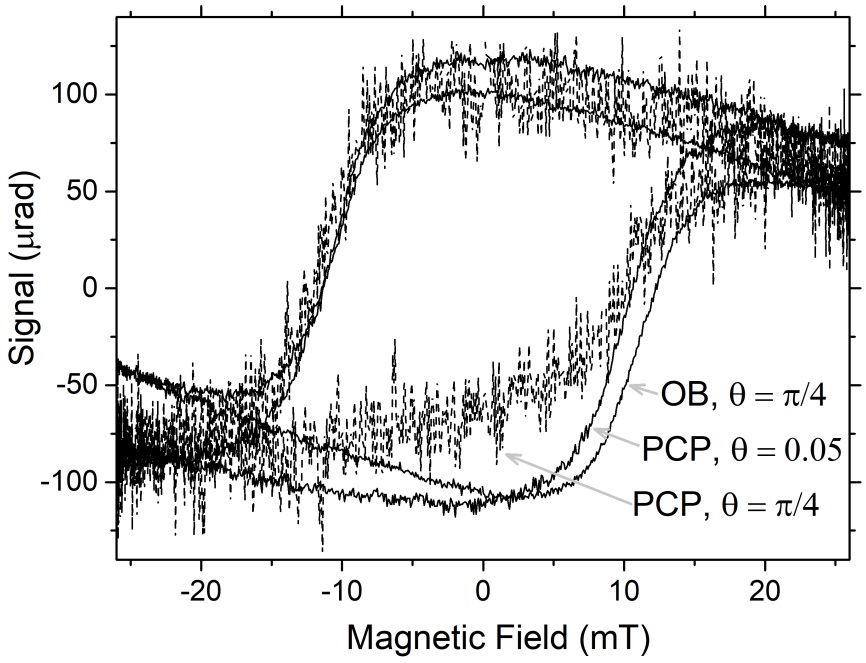

FIGURE 3.6: Hysteresis loop measured on the Au/Co/Au sample with three different experimental configurations with $\alpha = \pi/4$ rad yielding $\theta_F \approx 200$ μrad. The best SNR is obtained with the OB configuration, the RMS noise is equal to 30 nrad/$\sqrt{\text{Hz}}$. As expected from the results summarized in Table 2.1, the RMS noise obtained with PCP for the optimum θ angle is only slightly higher (55 nrad/$\sqrt{\text{Hz}}$). At the compromise angle for the PCP, $\theta = \pi/4$ rad, the RMS noise is much higher (340 nrad/$\sqrt{\text{Hz}}$) than that obtained with the optical bridge at the same angle.

and the PCP at the analysis angles that maximize their SNR values is illustrated in the Fig. 3.6. The resemblance of the two hysteresis loops confirms the results given in Table 2.1 and in Fig. 2.7. Still, in practice, when using PCP it is usual to set $\pi/4$ rad analysis angle as a compromise to the limitations imposed by the electronic noise at the nearly crossed position, to the mechanical difficulty in aligning polarizers to within very small angles and to the θ_F-dependent optimal alignment.

3.2 Test of sensitivities on terbium gallium garnet

In this section, the experimental setups of all three detection schemes and the experimental results are going to be presented. The Sagnac interferometer is mounted for this set of experiments, its photograph is shown in Fig. 3.7. A crystal of terbium gallium garnet (TGG) was chosen as a sample because of its high rotatory power

(Verdet coefficient V = 133.3 rad T^{-1} cm^{-1}) and excellent transparency properties required for the Faraday geometry. An oscillating magnetic field (of frequency 850 Hz) from a coil wired around the TGG rod of length 25 mm gives rise to the oscillating magnetizations within the sample, that are then sensed with the probe laser and demodulated using standard lock-in technique. The laser used in all three experimental setups is a variable power (1-20 mW) 532 nm source, the effective experimental bandwidth is 53 Hz, that results in intensities $2.7 \times 10^{15} < I_0 < 5.3 \times 10^{16}$ photon/s. In the following set of measurements the extracted value of Faraday rotation angle is equal to 38 μrad in all cases.

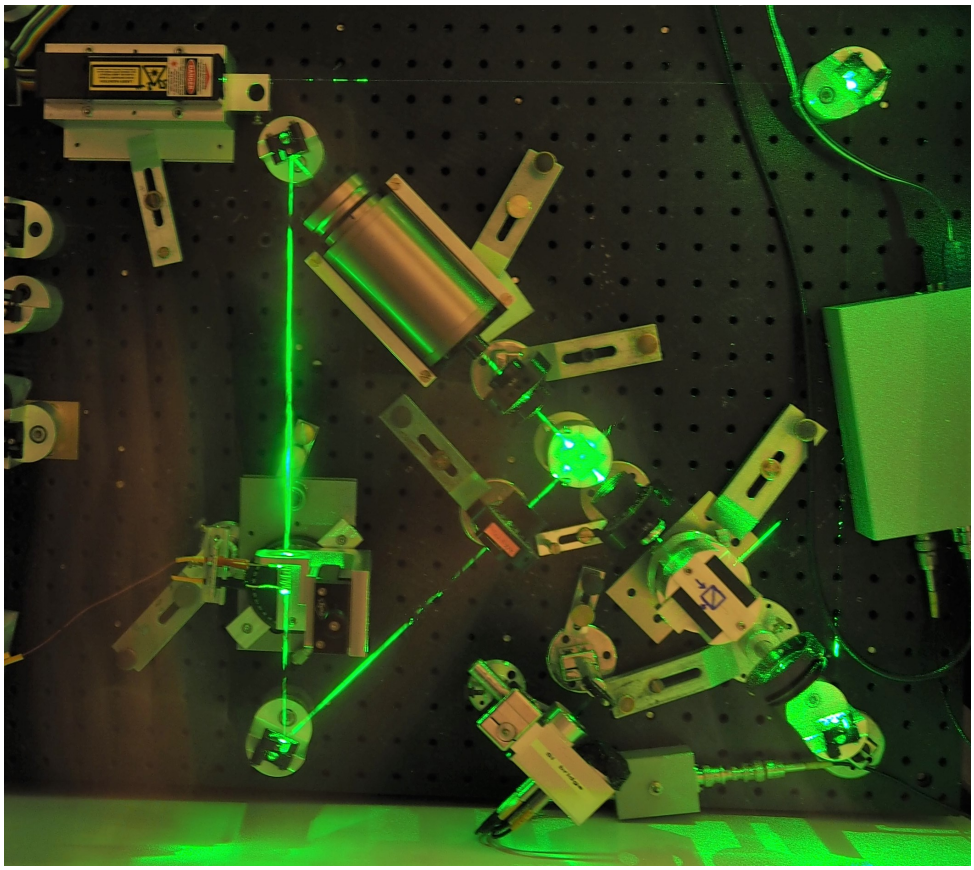

FIGURE 3.7: A photograph of a Sagnac experimental setup taken while pouring liquid nitrogen into the laser beam-path during 8 sec exposure time.

As in the previous section, the data including the MO contrasts and RMS noise θ and I_{det} dependencies are gathered in the Figure 3.8 demonstrating performances of (a) the PCP, (b) the Sagnac interferometer and (c) the optical bridge. The MO contrasts follow the theoretical $\sin 2\theta$ dependencies with the amplitude giving the value of Faraday rotation angle and for all three techniques, for the same amplitude of applied magnetic field, it is equal to θ_F = 38 μrad. The intensities I_0 used for

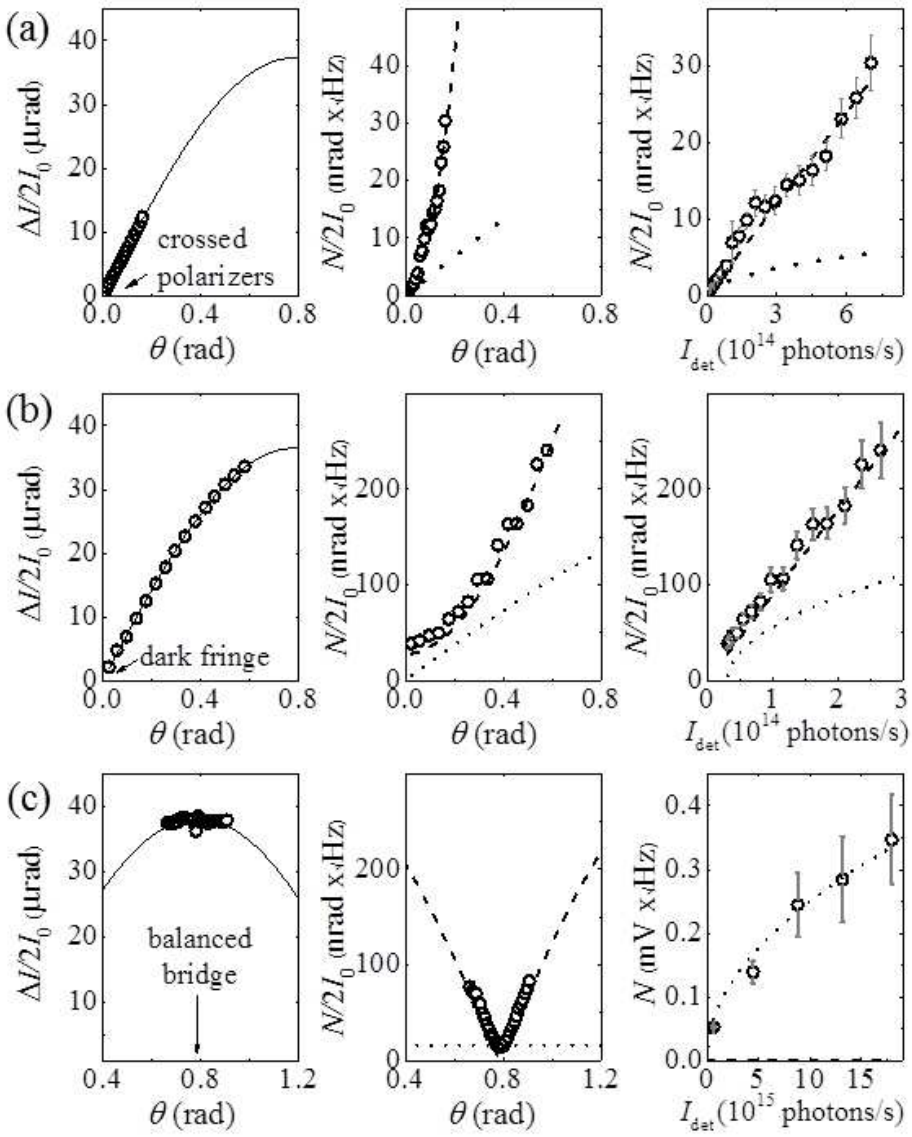

FIGURE 3.8: Experimental results obtained using (a) the PCP, (b) the Sagnac interferometer and (c) the optical bridge configurations.

normalization of the MO curves, as well as the RMS noise curves, equal to, correspondingly, $I_0 \approx 2.3 \times 10^{16}$ photons/s (PCP), $I_0 \approx 7.5 \times 10^{15}$ photons/s (Sagnac) and $I_0 \approx 2.4 \times 10^{16}$ photons/s (OB) , which correspond to 8.6 mW initial power in PCP experiment, 9 mW power in OB and 2.8 mW in the Sagnac experiment. The functional equivalence of the PCP and the Sagnac is visible from the curves as they follow the same part of θ function in Eqs. 2.11 and 2.22. The difference in intensities between the PCP and Sagnac interferometer measurements is evident from the amount of the curve plotted before the saturation of the detector. The MO signal on the bridge follows the $\sin 2\theta$ function in the proximity of its maximum at $\theta = \pi/4$ rad.

The middle panels demonstrate the RMS noise as a function of analysis angle θ, that was calculated as a standard deviation on a statistically large number of points. As an improvement to the previous experimental setup, the electronic noise was no longer the limiting source of noise for any of the experimental configurations and was omitted from the calculations. In the intensity range used here, the PCP and Sagnac interferometer measurements are entirely source noise limited, which is confirmed by intensity dependencies, that are linear in both cases as expected for the source noise (right panels in Fig. 3.8). The values of source noise parameter β extracted from the data are 10^{-7} for the PCP, 0.68×10^{-7} for the Sagnac and 0.3×10^{-7} for the optical bridge. The OB measurement shows similar results to the previous measurement on Au/Co/Au sample, specifically, because of the common mode rejection ratio (CMRR), it is shot noise limited in the area close to the optimum $\pi/4$ rad analysis angle, and it is source noise limited elsewhere. Choosing $\theta = \pi/4$ rad, we then varied the intensity of the laser light, which produced a square root function of the I_{det} that fitted nicely to the shot noise intensity dependence. Knowing the laser intensities, the shot noise estimation contained no adjustable parameters.

Because of the fact that, as we have seen previously, the shot noise RMS is a slower function of the light intensity ($\sim \sqrt{I_{det}}$) as compared to the source noise RMS which is $\sim I_{det}$, in the absence of electronic noise, by decreasing the light intensity and at some critical value of intensity I_{crit} a transition from source noise limited measurement to the shot noise limited measurement must occur. In the limit of $\theta_F \to 0$ and near the crossed polarizers (or dark fringe) condition where $\theta \to 0$, the I_{crit} where $N_{shot} = N_{source}$ is equal to $I_{crit} = 1/\beta^2$. In the Sagnac configuration, because of the $1/8$ decrease of the I_0 due to the loss in the beam splitters with respect to the PCP, this I_{crit} is $\sqrt{8}$ times higher. Using the β parameter found from the experimental fit, for the PCP the shot noise limited measurement can be performed only if we reduce the laser intensity below ≈ 37 μW. For the Sagnac this value is ≈ 100 μW. Thus, in principle, with low light intensities the shot noise limited measurement is achievable with the PCP and the Sagnac, yet the measurements with low light power is not beneficial since it reduces the signal to noise ratio in the shot noise limit.

In the following figure 3.9, the experimentally measured FOM for the PCP (left panel), the Sagnac interferometer (middle panel) and the optical bridge (right panel) are shown, along with theoretical predictions of source (dashed line), shot (dotted line) FOM, and the total FOM (solid line) defined using Eq. 2.33 with $I_0 \approx 5 \times 10^{15}$

photon/s in each case.

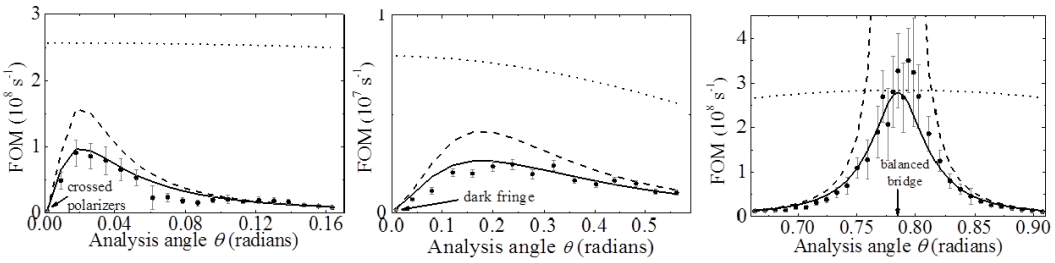

FIGURE 3.9: The experimentally measured FOM as a function of analysis angle θ for the PCP (left), the Sagnac interferometer (middle) and the optical bridge (right) configurations. Theoretical predictions accounting for the finite extinction ratio (or dark fringe) in the PCP configuration (in the Sagnac interferometer configuration) for total (solid line), source (dashed) and shot (dotted) FOM are presented. Shot noise limited measurement is achieved with the optical bridge in the balanced condition.

Let us start with the analysis of performances of the PCP and Sagnac experimental setups. While the shape of both FOM θ curves resembles that theoretically predicted (see Fig. 2.7), it is clear that the curves maximize at some angle distinct from θ_F. This happens because of the finite extinction ratio of the polarizers used in the PCP, or, in the case of the Sagnac, because of the finite fringe visibility. These quantities have been measured and equal to 4×10^{-4} for the polarizers and 4×10^{-2} for the dark fringe of the Sagnac, and they have to be accounted for in the expressions for intensity on the detectors (Eqs. 2.5 and 2.21) by adding them as offsets. This leads to some corrections to the RMS source and shot noises, and, in particular, that has relocated the maxima for the PCP and the Sagnac FOM functions.

The maximum FOM in the Sagnac interferometer is ~ 30 times lower than that obtained with the PCP, which can be explained in part by factor 8 reduction in the shot noise FOM, in part by the larger amount of optical components necessary for the function of the Sagnac (compare Figs. 2.4 and 2.5). Additional reduction may come from the poor extinction ratio arising due to the back reflection of non-interfering photons off various optical elements in the setup.

The FOM obtained with the optical bridge, shown in the right panel of Fig. 3.9, demonstrates the shot noise limited measurement with the balanced bridge condition. As already mentioned, at this analysis angle, the source noise rejection happens which leads to very low RMS noise values around $\theta = \pi/4$ rad. This, in turn, produces large error bars on the FOM, since in the error estimation for the FOM the total RMS noise appears cubed in the denominator: $\Delta\text{FOM} \sim 1/N^3$.

Away from the balanced bridge condition, where the intensity on the detectors is no longer compensated, it is the source noise that starts to dominate. This allows for the estimation of source noise fitting parameter β which is equal in this case to 0.68×10^{-7}. Thanks to common mode rejection of the source noise, the maximum FOM in the bridge is 2 to 3 times higher than the maximum FOM for the PCP configuration for essentially the same light intensity.

The superior FOM of the optical bridge is validated by a 3 nrad Faraday rotation measurement obtained by applying magnetic field of about ~ 0.9 nT to the TGG rod.

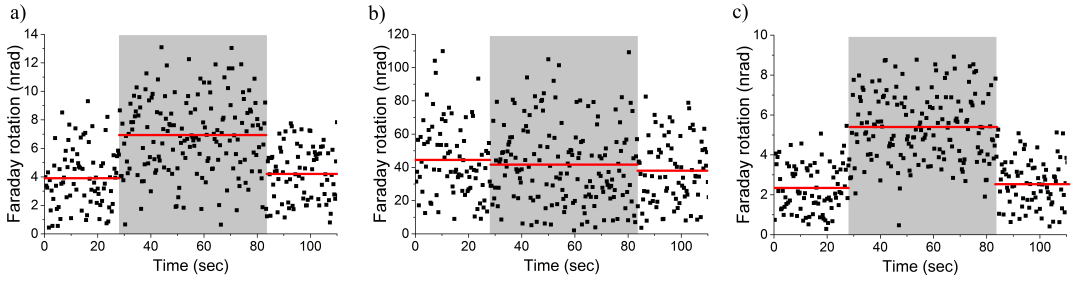

FIGURE 3.10: An attempted measurement of a 3 nrad Faraday rotation during the application of a small magnetic field of value ~ 0.9 nT (on the gray background) in a bandwidth of 1.5 Hz.

In the Fig. 3.10 the evolution of the Faraday rotation angle is shown with the magnetic field switched on only during the times marked by the gray background color. The Faraday rotation is established from Eq. 2.11, Eq. 2.22 and Eq. 2.26, respectively, using the measured MO signal (ΔI), known source intensity (I_0) and the optimal analysis angles $\theta = 0.03$ rad in the case of PCP, $\theta = 0.2$ rad for the Sagnac and $\theta = \pi/4$ rad for the optical bridge. With the measurement bandwidth of 1.5 Hz, the contrast is clearly seen in the case of the optical bridge arrangement. It is still visible with the PCP arrangement, and it is well within the noise level for the measurement with the Sagnac interferometer configuration.

In conclusion of this part of the study, the optical bridge detection scheme has demonstrated the highest FOM of all three considered Faraday rotation measurement techniques and the shot noise limited measurement with the noise floor of 1.3 nrad/$\sqrt{\text{Hz}}$ at high intensity on the detectors where large SNR is achieved. This optical detection method is favored for the subsequent measurements of Faraday rotations in semiconductors.

3.3 Field-induced Faraday effect in GaAs

The investigation of the Faraday rotation angle dependence on the probe light wavelength as discussed in the previous Chapter 2 in bulk sample of GaAs ($n = 5.5 \times 10^{15}$ cm^{-3}) was achieved by the application of an external magnetic field to the sample with non-zero parallel component to the wave vector of light propagation. In the absence of the optical pumping, this experiment is described by $\theta_F = VB_{\parallel}L$ expression, where V is the Verdet constant characteristic to the studied material, $B_{\parallel}$ is the parallel to the light propagation direction component of the external magnetic field, and L is the thickness of the material.

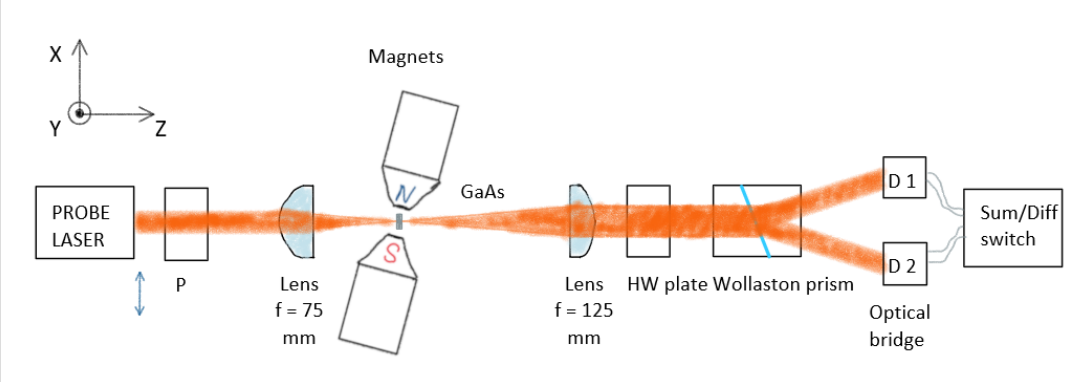

FIGURE 3.11: Experimental configuration for classical in-field Faraday effect measurement. The magnets are tilted at an angle of $\sim 15°$ to produce a longitudinal component along Z-axis, linearly polarized tunable laser source probes the created magnetization. The detection of the rotations is performed with the optical bridge.

In this way, as opposed to the optical pumping experiments, for this type of experiment it is the parallel component of external magnetic field that creates a magnetization in the sample. The production of the parallel component $B_{\parallel}$ of magnetic field is attained by simply rotating the electromagnets by an angle $\sim 15°$ along the Y-direction. As a probe source, a Ti:Sapphire CW laser is used in the wavelength range $\lambda \in [840; 1000]$ nm dictated by the optics within the laser cavity. The measurement is organized as follows: for a specific probe wavelength, the magnetic field is swept in the range [-0.94; 0.92] T, which gives [-0.22;0.22] T range for the parallel component of the applied magnetic field. The Verdet coefficient is derived from the slope of linear approximations of the measured Faraday rotation as a function of the magnetic field parallel component divided by the length of the sample (500 μm). One example of such Faraday rotation magnetic field sweeps is shown in Fig. 3.12 for a probe wavelength of 940 nm where the Verdet coefficient maximizes (V = 46

rad·m^{-1}T^{-1}) in the range of wavelengths studies in the sample. The wavelength of the probe is then varied in the range from 840 nm to 1 μm, the magnetic field sweep is repeated for each wavelength from which the Verdet coefficient spectrum is built.

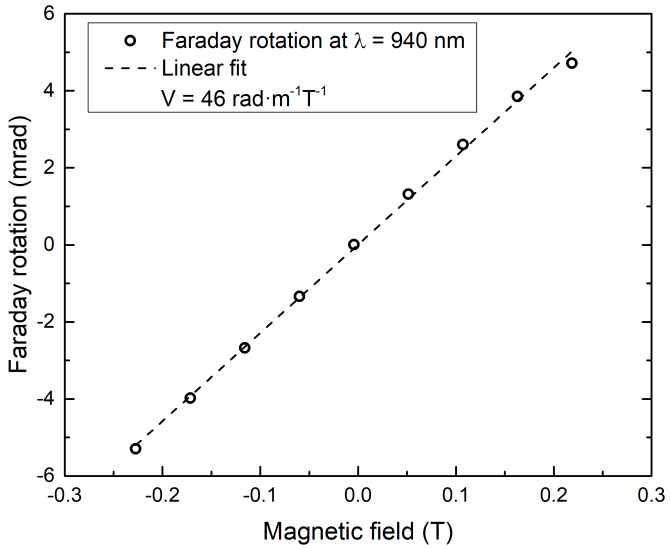

FIGURE 3.12: Faraday rotation angle as a function of the parallel component of the applied magnetic field for the probe wavelength of 940 nm (photon energy = 1.32 eV).

The resulting Verdet coefficient spectrum for the sample of non-intentionally doped GaAs measured at room temperature is presented in Fig. 3.13. This attained spectrum compares very well with the one measured by Gabriel and Piller, 1967 and presented in Fig. 2.2. The rapid variation of the Faraday rotation corresponds to the absorption edge as confirmed by additional measurement of the transmitted light intensity, with absorption coefficient plotted along right Y-axis.

Let us now plot the Verdet coefficient along with the first derivative of that absorption coefficient with intention to confirm in some sense the proportionality described by Eq. 2.2 from Chapter 2. The sign of the Verdet coefficient has been reversed in order to demonstrate the qualitative closeness of the two curves depicted in Fig. 3.14.

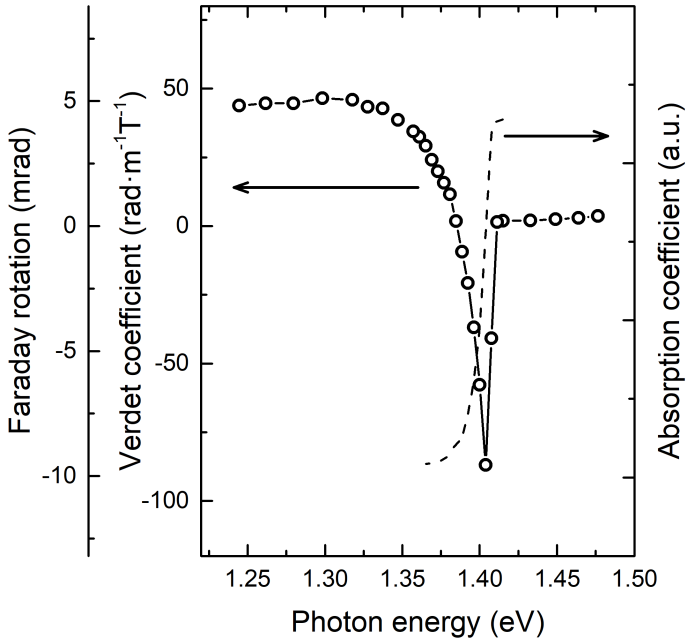

FIGURE 3.13: Verdet coefficient spectrum measured at room temperature on a sample of non-intentionally doped GaAs (n = 5.5×10^{15} cm^{-3}). The second left Y-axis shows the maximum reached Faraday rotation in the experiment in the magnetic field of 0.22 T. The axis on the right side of the figure shows an absorption spectrum in the studied sample.

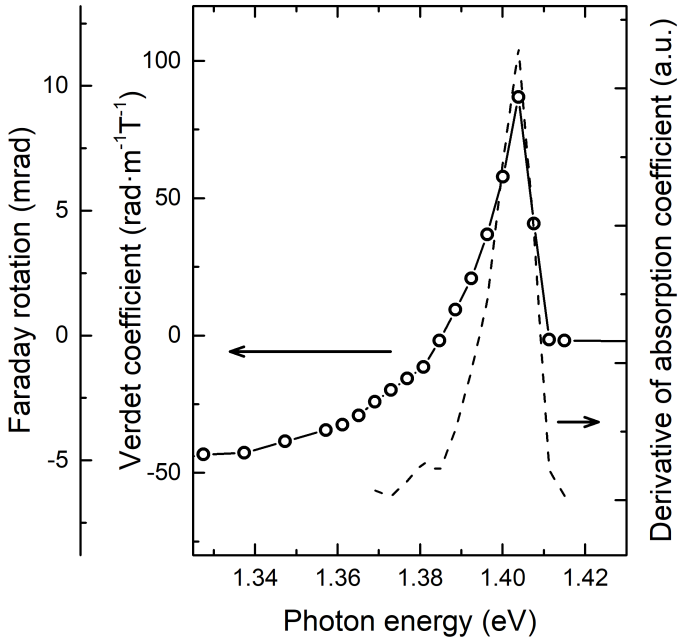

FIGURE 3.14: Reversed Verdet coefficient spectrum measured at room temperature on a sample of non-intentionally doped GaAs (left Y-axis) with the first derivative of the absorption coefficient (right Y-axis).

Chapter 4

Detection of spin of electrons in GaAs

This chapter will discuss the details of optical pumping in direct band gap GaAs including optical selection rules, provide the expressions for the steady-state electronic polarization and for the polarization of photoluminescent signal. The polarized photoluminescence experiment is then performed on the sample of GaAs ($n = 5.5 \times 10^{15}$ cm^{-3}). Furthermore, it will discuss briefly the Hanle effect which will be then observed in experiments on the photoinduced Faraday rotation, where in the transverse magnetic field the signal will decrease according to a Lorentzian function. The same sample of GaAs will be then used in a series of Faraday rotation measurements. The experimental setup and the measurement procedure will be explained carefully. The first set of Hanle data is presented along with the necessary modifications to increase the magnitude of the apparent rotation. The photoinduced Faraday rotation as a function of probe wavelength will then be presented and compared with the classical field-induced Faraday rotation. The Hanle effect curve for a specifically chosen probe wavelength will be presented finally, from which the spin lifetime is calculated.

4.1 Optical spin orientation in GaAs

In the process of optical pumping, developed by Alfred Kastler (1957), photons of a particular energy are used to raise, or "pump", electrons from one level to another. When applied to the case of semiconductors a photon of energy $\hbar\omega > E_g$ is absorbed with a creation of electron in the conduction band and a hole in the valence band of

the semiconductor. During the process the energy, crystal momentum and angular momentum of the photon are redistributed between the electron and the hole.

Further we will concentrate on describing briefly the theory of optical pumping in direct semiconductors by the example of GaAs.

Let us take a look first at the electronic band structure of GaAs near the center of the Brillouin zone ($\boldsymbol{k}$=0, Γ point) (see Fig. 4.1). GaAs is a representative of direct band gap semiconductors meaning that the maximum of the valence band and the minimum of the conduction band occur at the same point in the reciprocal space, at Γ-point, and the energy difference between them is called the band gap (E_g), which for GaAs at room temperature is equal to 1.42 eV[1]. The $\boldsymbol{k}$=0 conduction band state is s-type with orbital momentum l=0 and spin s=1/2 (total angular momentum j = 1/2) thus doubly degenerate in spin. The corresponding valence band state consists of 3 sub-bands, two of which are degenerate at $\boldsymbol{k}$=0, *heavy* and *light* holes (HH and LH) sub-bands. Their total angular momentum j = 3/2. The third band is called *split-off* (SO) band and it is shifted in energy by Δ_{SO} = 0.34 eV and has j = 1/2. The reason for this shift lies in the concept of spin orbit interaction, which is crucial for spintronics as it allows the spin filtering in non magnetic semiconductors and it increases for materials with heavy atoms.

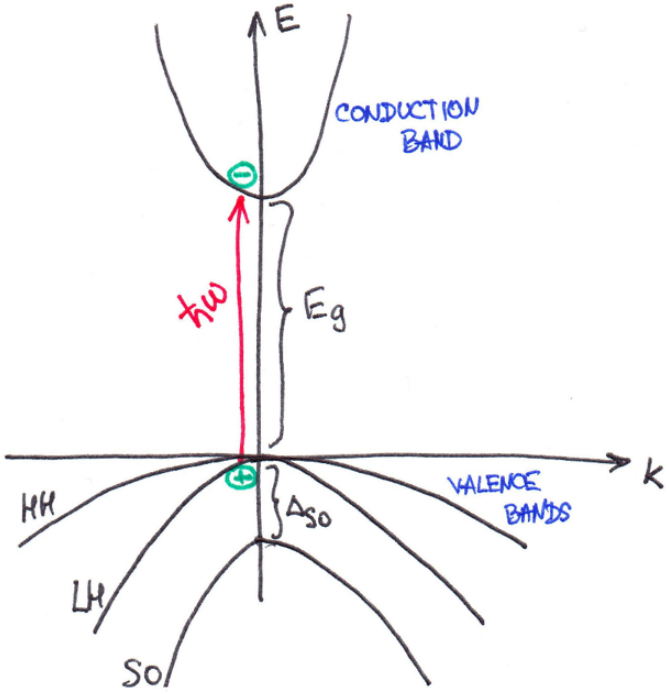

FIGURE 4.1: Electronic band structure of GaAs near Γ-point

[1] *GaAs - Gallium Arsenide: Band structure and carrier concentration*.

4.1.1 Electron polarization in the steady-state regime

Since the photon momentum $\hbar k = 2\pi\hbar/\lambda$ is small on the scale of the Brillouin zone, on the band diagram it can be represented as a vertical arrow of length $\hbar\omega$. The ends of the arrow give the initial energies of the electron and the hole. The photon of energy $\hbar\omega < E_g$ will not be absorbed by the structure; the photon of energy comprised between $E_g < \hbar\omega < E_g + \Delta_{SO}$ will generate an electron accompanied by a heavy or a light hole, whereas $E_g + \Delta_{SO} < \hbar\omega$ transitions will involve holes from all three sub-bands.

Along with the energy and momentum conservation the angular momentum carried out by the photon is transmitted to the electron-hole pair and this is what defines the optical spin orientation. Photons of right (σ^+) or left (σ^-) circularly polarized light have a projection of the angular momentum on the $\boldsymbol{k}$-vector of light propagation that equals to +1 or -1. The distribution of this angular momentum between the electron and the hole is dictated by *optical selection rules* that result from the restrictions imposed on the electric-dipole operator (interaction of an electron with the electromagnetic field) by the symmetries of the wave functions in crystals.

For direct optical transitions it is possible to calculate the optical selection rules knowing the symmetries of the states and using the fact that in an electric-dipole transition the orbital angular momentum can change only by ± 1. Such possible transitions are shown in Fig. 4.2 for σ_+ and σ_- polarized light and their relative intensities are noted close to each transition under σ_+ polarized light.

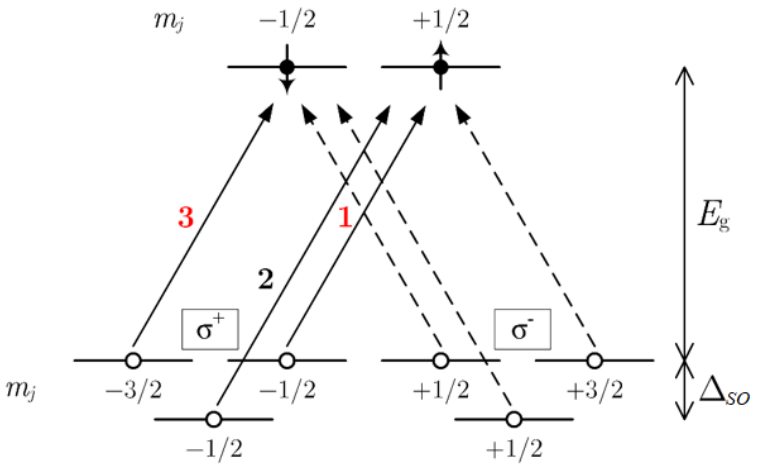

FIGURE 4.2: Relative intensities of optical transitions for GaAs

From this diagram two main conclusions can be drawn:

- If we sum up the relative intensities of all three transitions the two spin states in the conduction band will be populated equally. Thus illuminating GaAs with photons of energy well above $E_g + \Delta_{SO}$ results in no net electron polarization.
- If the photon energy lies in the region $\hbar\omega \in [E_g; E_g + \Delta_{SO}]$ then there will be three times more electrons with spin in the direction opposite to light propagation direction (spin-down) than electrons with spin aligned with the propagation direction (spin-up). Initial polarization defined as

$$P_i = \frac{N_+ - N_-}{N_+ + N_-}, \tag{4.1}$$

where N_+ and N_- are relative populations of spin-up and spin-down electrons, in the case of GaAs will be equal to:

$$P_i = \frac{1-3}{1+3} = -1/2, \text{ or } -50\%. \tag{4.2}$$

Thus we can think of the initial polarization as a step function of photon energy that changes from $-1/2$ to 0 at $\hbar\omega = E_g + \Delta_{SO}$.

During the lifetime of photoexcited electrons, τ, their spin polarization may decrease due to several spin relaxation processes that can be intrinsic to the crystal (SOI, electron-hole, electron-phonon interactions, hyperfine-coupling with the magnetic field from nuclei) or extrinsic (precession around an external magnetic field applied perpendicular to the axis of light propagation). If a semiconductor is continuously illuminated with circularly polarized light, the steady state electron (minority carrier) concentration n and the concentration of electronic spins s are expressed via the lifetime of electrons τ and the spin lifetime τ_s and electron-hole photoexcitation rate G that depends on the laser characteristics:

$$\begin{aligned} n &= G\tau \\ s &= P_i G \tau_s \end{aligned} \tag{4.3}$$

The steady-state electron polarization is by definition the ratio of the electron concentration to the electron spin concentration that can be rewritten as a function of initial polarization and the ratio of the lifetimes:

$$P_{EL} \equiv \frac{s}{n} = \frac{P_i G \tau_s}{G\tau} = P_i \frac{\tau_s}{\tau} \tag{4.4}$$

Let us introduce *spin relaxation* time associated with all the intrinsic spin relaxation processes, which we will call T_1. Generally, there are two reasons for electron spin to return to equilibrium: recombination and spin relaxation. In the light of this the spin lifetime can be represented as the combination of the time scales associated with recombination (τ) and spin relaxation (T_1):

$$\frac{1}{\tau_s} = \frac{1}{\tau} + \frac{1}{T_1} \tag{4.5}$$

Equation 4.4 can then be rewritten using spin relaxation time, which is equivalent to the speed of depolarization:

$$P_{EL} = \frac{P_i}{1 + \tau/T_1} \tag{4.6}$$

Now we can interpret this expression as follows: if $T_1 \gg \tau$, in which case $\tau_s = \tau$, then the spin of the electron is conserved at all times right until the moment of recombination and the electronic polarization remains at its maximum value P_i; if $T_1 < \tau$, which is the most frequent case, then the steady-state electronic polarization is smaller than the initial polarization: $P_{EL} < P_i$ because of spin relaxation. In the case characteristic for indirect band gap semiconductors, where $T_1 \ll \tau$, the ratio τ_s/τ as well as the electronic polarization become immeasurably small.

The effect of a magnetic field applied perpendicularly to the k-vector of light propagation leads to a decrease in the electron polarization following a Lorentzian line shape, from which the electron spin lifetimes are easily extracted, and will be discussed further in more details (see Section 4.3).

4.1.2 Polarization of the photoluminescence

In a reverse process the photoexcited electron and hole recombine with emission of a photon. This process establishes *polarized photoluminescence* (PL) technique and is governed by the same selection rules as optical orientation. In this case for 100% polarized spin-down electrons there will be three times more σ_+ polarized photons and the light polarization will be $P_{PL} = 50\%$ for emitted photons of energy $\sim E_g$. However the electron polarization does not reach 100% and therefore the final polarization of emitted light expresses as:

$$P_{PL} = P_i P_{EL} = P_i^2 \frac{\tau_s}{\tau} \tag{4.7}$$

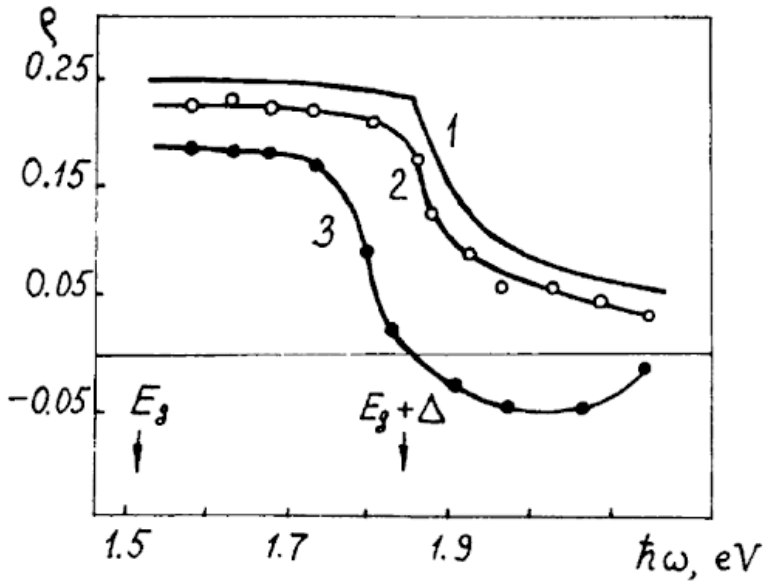

FIGURE 4.3: Dependence of the PL polarization on the photon energy in p-GaAs crystals of different doping densities at 4.2°K (Ekimov and Safarov, 1971). Curve 1 corresponds to a theoretical calculation, whereas curves 2 and 3 are experimentally taken for doping concentrations of 4×10^{19} cm $^{-3}$ and 7.8×10^{16} cm^{-3}. At such low temperatures the band gap energy E_g = 1.52 eV, the split off energy Δ_{SO} = 0.33 eV.

The above results are valid for excitation with photons of energy equal to E_g, however it is interesting to look at what happens when the photon energy increases. A work by Ekimov and Safarov, 1971 investigates the dependecies of photoluminescent polarization on the energy of the pump for two samples of different doping densities. Figure 4.3 shows a theoretical (curve 1) and experimental (curve 2 and 3 for doping concentrations 4×10^{19} cm $^{-3}$ and 7.8×10^{16} cm^{-3}) dependencies of the photoluminescence polarization as a function of photon energy $\hbar\omega$. Theoretical curve 1 calculated by Dyakonov and Perel corresponds to the case where $T_1 \gg \tau$. In such a way the difference between theoretical curve 1 and experimental curves 2 and 3 close to the band edge is due to spin relaxation. The decrease of the polarization for photon energies close to $\hbar\omega = E_g + \Delta_{SO}$ is not actually related to the transitions from split-off band, as they make only small contribution to the overall polarization, but it is caused by the light-hole band transitions, which, at higher energies can no longer be approximated by Γ-point states. Curve 3, on the contrary, does not agree with the spin relaxation free theoretical curve, there is a reverse in sign of polarization even before the start of split-off transitions. Such behavior is explained by

Dyakonov and Perel, 1971 relaxation mechanism characteristic for noncentrosymmetric semiconductors. It was shown that the splitting in the conduction band for crystal momenta $k > 0$ results in spin relaxation of electrons excited with some kinetic energy ("hot" electrons). This mechanism is suppressed in semiconductors with high impurity concentration (example of curve 2) due to very rapid momentum relaxation on impurities. This shows how important are different parameters of a semiconductor and the study of polarization as a function of different parameters such as doping concentration, temperature, external fields, stress, reveal new information or confirm existing theories.

4.2 Optical pumping. Detection via polarized photoluminescence

Preliminary to the Faraday detection methods, the GaAs sample has been tested with a polarized photoluminescence technique. The experimental setup for this type of measurement has been mounted by the members of our group and described in details by Favorskiy et al., 2010; Cadiz et al., 2014. Briefly, a laser source of a chosen wavelength λ = 780 nm and 1 mW power, is linearly polarized before passing through a liquid crystal polarization rotator. Depending on the control voltage on the liquid crystal rotator, the output polarization state of the beam is switched between σ^+ and σ^- polarization. The laser is focused on the sample with a x50 objective, the radius of a diffraction limited gaussian spot is equal to 0.5 μm. Luminescence from the sample is analyzed with the quarter wave plate and the second liquid crystal rotator. Once the reflected laser beam is removed with a long pass filter, the luminescence light is analyzed with a spectrometer.

In order to get the polarization spectrum and to get rid of the residual birefringence in the optical path, the control voltages applied to the liquid crystal rotators are switched between σ^+ and σ^- polarizations, both in the excitation arm and in the luminescence detection arm. The signals measured for various combinations of these polarizations are denoted by σ^{++}, σ^{+-}, σ^{--} and σ^{-+}. The photoluminescence polarization is described by the following combination of the four signals:

$$P_{PL} = \frac{\sigma^{++} - \sigma^{+-} + \sigma^{--} - \sigma^{-+}}{\sigma^{++} + \sigma^{+-} + \sigma^{--} + \sigma^{-+}} \tag{4.8}$$

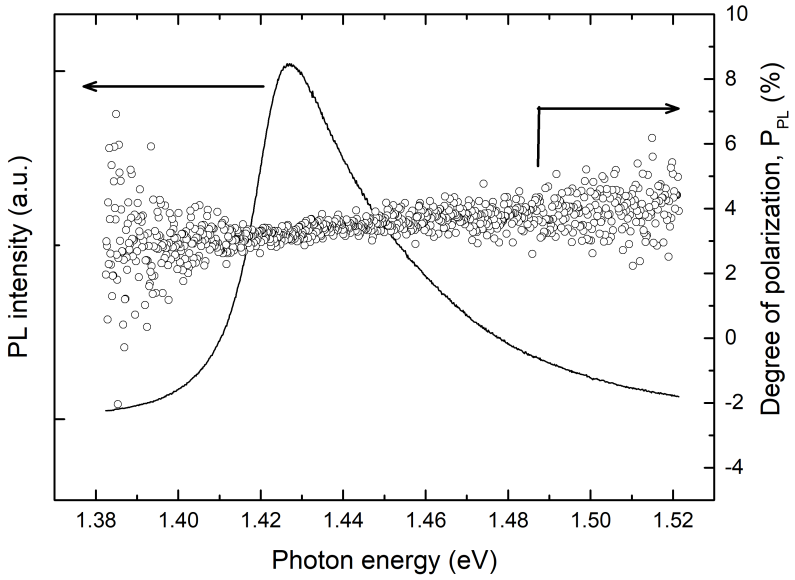

FIGURE 4.4: Spectrum of the intensity of the photoluminescence signal (on the left) and the degree of polarization of the PL signal, P_{PL} (on the right), measured in n-type bulk GaAs sample with $n = 5.5\times10^{15}$ cm^{-3} at room temperature.

For each of the four polarization combinations, we have chosen 5 seconds of acquisition time. The results of the conducted PL experiment are shown in the Fig. 4.4 that includes the PL intensity spectrum on the left Y-axis, as well as the spectrum of the degree of polarization of the photoluminescence signal, defined using Eq. 4.8 (the right Y-axis). By integrating the four signals in the range of photon energies $\hbar\omega \in [1.39; 1.51]$ eV we estimate the averaged degree of photoluminescence polarization to be equal to 3.4 %. According to the selection rules for GaAs (described by Eqs. 4.1 and 4.2), the modulus of the initial degree of polarization P_i is equal to 0.5. We can then relate the degree of photoluminescence polarization with the electron steady-state polarization (see Eq. 4.7), and find P_{EL} = 6.8 %. Subsequently, the ratio of the relaxation times, τ_s/τ, equals to 0.137.

4.3 Hanle effect

It is a convenient method to confirm the spin related nature of the signal and to extract some relevant information about the spin. The Hanle effect, first discovered by Wood and Ellett, 1923, later described by Hanle, 1924, consists in the depolarization of electron spin in transverse magnetic field. It happens due to the precession

of individual spins around the direction of the applied magnetic field with Larmor frequency ω_L, and, under steady-state optical pumping conditions, this results in the decrease of the average degree of spin polarization as a function of applied field, and, hence, in the decrease of the apparent rotation. The line shape of the dependency of the Faraday rotation (or any spin related signal such as the degree of spin polarization, for example) on the magnitude of applied transverse magnetic field $B_\perp$ is given by the Lorentzian distribution centered at zero-field:

$$\theta_F(B) = \frac{\theta_F(0)}{1 + {}^{B_\perp}/_{B_{HWHM}}}, \tag{4.9}$$

where θ_F is the maximum rotation attained in the absence of external magnetic fields and B_{HWHM} is a characteristic half-width of the depolarization curve at half-maximum ($\theta_F(0)/2$), that is defined as:

$$B_{HWHM} = \frac{\hbar}{g\mu_B\tau_s}. \tag{4.10}$$

Here $\hbar$ is the Planck constant, g is the electron Landé factor, μ_B is the Bohr magneton, and τ_s is the spin lifetime, discussed in Eqs. 4.4 and 4.5. In this way by performing Hanle type experiment, i.e. by applying the transverse magnetic field strong enough to decrease the measured signal, the electron spin lifetimes can be extracted, this technique is effectively and widely used in experiments on electron spin orientation in semiconductors (Parsons, 1969).

4.4 Optical pumping. Detection via Faraday effect

This part of the work concentrates on the details of experiments conducted on semiconductor crystal of GaAs while optically pumping it with circularly polarized light and detecting Faraday rotation of the probe light using the optical bridge detection scheme.

4.4.1 Experimental setup description

A scheme of the experimental setup on optically pumped semiconductors as used for GaAs sample is sketched in Fig. 4.5. The two major parts of it are the optical pumping and magneto-optic Faraday effect detection parts. The optical pumping part consists of a pump laser of wavelength λ = 785 nm, a combination of a HW

plate (which rotates the initial linear polarization of the pump light for it to make an angle $\pi/4$ radians with the y-axis marked in the figure) and a Babinet-Soleil (BS) compensator used to alternate the polarization of the pump laser between right circular σ^+, linear π^+ (aligned with the input to the BS compensator), left circular σ^- and linear π^- (perpendicular to the input polarization). In theory, that should result in a slow modulation of a non-equilibrium degree of spin polarization from $+P_{EL}$ for the σ^+ polarization, through 0 when the incident polarization on the sample is linear, to $-P_{EL}$ for the σ^- polarization and back to 0 for linear perpendicular polarization.

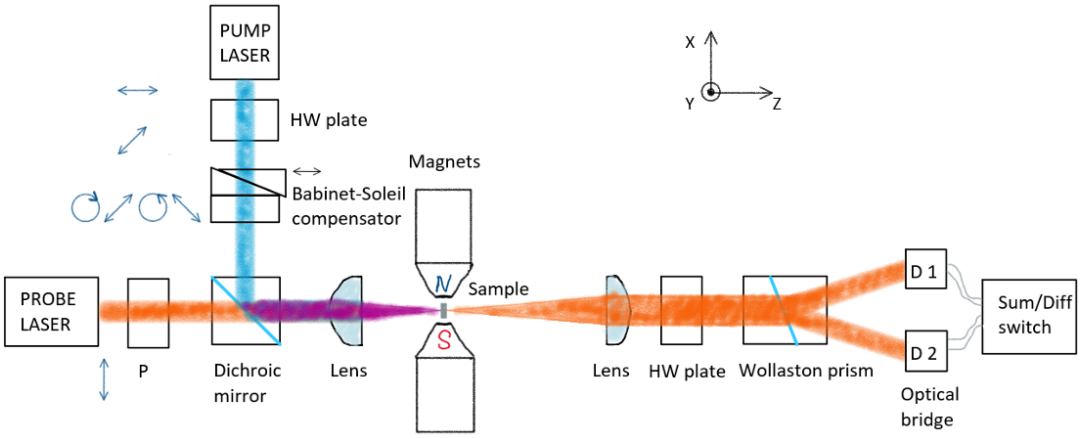

FIGURE 4.5: A generalized scheme of the experimental setup for the Faraday effect measurements of optically pumped semiconductors. The two lasers displayed here work in the continuous-wave (CW) operation mode: the first one is the pump laser, needed to create a non-equilibrium electron spin population, and the second one is the probe laser for the Faraday rotation measurements, both are at normal incidence with the sample. The former is absorbed by the sample, while the latter is transmitted and detected using the optical bridge detection scheme.

The corresponding change in magnetization is sensed with the other significant part of the experiment - magneto-optic detection of Faraday effect. This part involves a probe laser with tunable wavelength, a polarizer right after the laser to insure the linear polarization of the light entering the sample. This polarization is then rotated in accordance with the polarization of the pump light getting to the sample, and the rotation of the plane of polarization is detected using an optical bridge detection scheme under optimum, balanced condition, which is discussed previously in Chapters 2 and 3 in details. A plano-convex lens is used to focus both probe and pump light on the sample surface for an increase in the apparent density of electron spin-population and, in the case where the beam sizes of the pump and the probe lasers are comparable, an increase in rotation angle due to the Faraday effect.

Right after the second lens which collimates the transmitted probe beam, another HW plate is mounted on a motorized rotation stage to balance the optical bridge. A Wollaston prism replaces a PBS used in the previous experiments (see Chapter 2) and separates the beams of orthogonal polarizations (along X- and Y-axes on the scheme). Finally, two identical photo-diodes (D1 and D2) that we connect in a different manner and monitor either the sum (diodes connected in parallel) or the difference of currents ("anti-parallel", or back-to-back connection). The change-over of the connection type from the sum current (corresponds to I_0 from Eq. 2.26) to the difference current (I_{bridge}) is automatized and made by a specifically designed switch.

When there is some non-zero signal measured, the next step is to make sure the signal is spin-related. This is made by conducting the Hanle effect measurement where an external magnetic field from the electromagnets is applied in the direction which is transverse to the beam propagation direction. An issue of magnets not being perfectly perpendicular to the beams direction and thus inducing the classical Faraday effect rotation, is simply overcome by balancing the bridge for each value of applied transverse magnetic field.

The further details of each of the optical component and on the measurement process are given in the subsections below.

4.4.2 Calibration of the Babinet-Soleil compensator

In order to perform Faraday rotation measurements on optically pumped semiconductors, two laser sources are needed. First of all, an appropriate light source for the optical pumping is required to create the non equilibrium electron spin polarization in the semiconductor. The energy of the photons thus has to be slightly higher than the band gap energy, the exact range of required energies depends on the choice of a semiconductor material as well as on the temperature and the doping densities. As discussed in Chapter 1, this light gets absorbed to some extent in the sample, and depending on its polarization state and on the properties of the sample, the electron spin population is introduced (P_{EL}). In the present experiments the polarization of pump light is modulated at low frequencies (of ~ 1 Hz) between σ^+, π^+, σ^- and π^- polarizations with the help of BS compensator. Its principal axes (the fast axes of two birefringent wedges and a compensator plate constituting the BS compensator) are aligned along Y- and Z-directions marked in the Fig. 4.5. In order for it to

function properly, the input linearly polarized light has to form a $\pi/4$ radians angle with the axes of BS. This is the reason for a HW plate that is placed in front of the BS, it rotates the linear polarization of pump light. Before actual measurements, the displacements of BS compensator that correspond to a specific output polarizations (σ^+, π^+, σ^- and π^-) have to be found. During this calibration process, an additional polarizer is usually crossed with the output polarization from the HW plate in the absence of the BS compensator. The compensator is then placed in between and the position of the moving wedge is scanned with the help of the piezomotor (PI C866) through the range of positions [0;18] mm with the typical precision of 0.1 μm. A resulting transmitted intensity dependency on the introduced phase shift ϕ between the two orthogonal polarizations of light (aligned with the axes of the BS) is as follows:

$$I = I_0 \sin^2 \phi/2, \tag{4.11}$$

where I_0 is the incident intensity of light.

The Fig. 4.6 demonstrates the transmitted intensity during the BS calibration process for four different laser wavelengths: 840, 885, 942 and 1000 nm. By definition, zero-order position is when the total path length in the wedges is equal to that in the compensator plate, this way a 0 phase shift is introduced to the light polarization, thus this position is wavelength-independent. By superimposing the four calibration curves for different wavelengths, the zero-order position is easily found to be approximately equal to 4 mm, which corresponds to the maximum transmitted intensity, meaning that in this particular calibration process the polarizer at the output of the BS compensator was in fact aligned with the input polarizer. For the chosen wavelength, the period of sinusoidal function is then found, from which positions of circular polarization outputs are deduced, which correspond to the displacements at half transmitted intensity amplitude. The respective linear polarizations correspond to the minimum and maximum of the sinusoidal dependence.

If we choose to work in the vicinity of the zero-order displacement, that would mean that the retardation is 0 and π radians for linear polarizations (π^+ and π^-) and $\pi/2$ and $3\pi/2$ radians for circular σ^+ and σ^- polarizations. We have chosen to work further from the zero order displacements because of the blur on the static part of the BS compensator (stretched between 1 and 5 mm of the BS displacement) that appeared from the previous experiments with UV excitation.

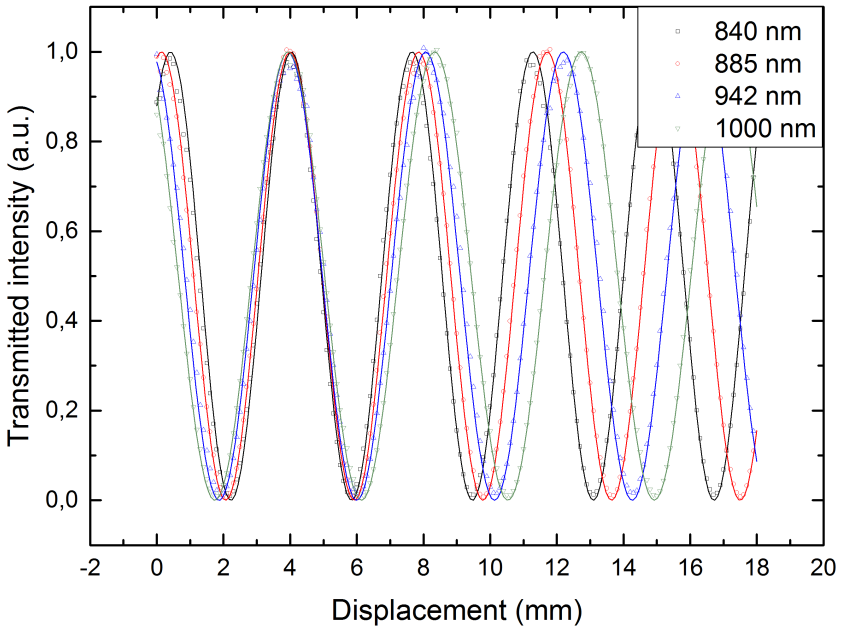

FIGURE 4.6: The dependences of transmitted light intensity on the moving wedge displacement during the calibration of the Babinet-Soleil compensator process. Four different wavelengths are tested, and four displacements corresponding to required polarizations are deduced for each of the wavelengths.

4.4.3 Measurement procedure

The second laser is used to probe the created magnetization, which is proportional to the spin polarization. The polarization of the probe light is linear and gets rotated within the sample, the rotation angle θ_F being proportional to the magnetization, and, hence, to the electron spin polarization P_{EL}. Let's assume that right circular pump light polarization is seen by the detection system as a negative rotation angle θ_F and left circular polarization results in a positive θ_F rotation. In theory, the MO contrast is the difference in the bridge responses for Faraday rotations of $\pm\theta_F$ signals corresponding to σ^+ and σ^- pump polarizations, and is defined by Eq. 2.26. Applied to the case of optical pumping, that would result in taking difference between the difference signal on the bridge at the moment when the pump polarization is σ^+, i.e. $I^{\sigma+}_{bridge} = I_0 \cos 2(\theta - \theta_F)$, and the bridge signal corresponding to σ^- pump polarization, $I^{\sigma-}_{bridge} = I_0 \cos 2(\theta + \theta_F)$.

However, when the position of the BS compensator is changed, the total intensity of light coming to the detectors may change depending on the pump polarization and the normalization must be performed for each of the four BS positions. In practice we register and combine eight signals corresponding to various pump light polarizations: four bridge signals $I^{\sigma+}_{bridge}$, $I^{\pi+}_{bridge}$, $I^{\sigma-}_{bridge}$ and $I^{\pi-}_{bridge}$, that are the differences of currents in two detectors, which we then normalize using four detected sum signals $I^{\sigma+}_0$, $I^{\pi+}_0$, $I^{\sigma-}_0$ and $I^{\pi-}_0$. The change from the difference signal to the sum signal is done with the special switch and the order in which the measurements are preformed is as follows: the BS compensator moves to its first, σ^+, position, where the bridge difference signal $I^{\sigma+}_{bridge}$ is measured, followed by a quick switch to the sum signal and $I^{\sigma+}_0$ is measured; the BS compensator is then moved to its second position and the procedure is repeated with the help of the switch. By taking an example of σ^+ polarization, the normalized signals take the following form: $I^{\sigma+}_N \equiv I^{\sigma+}_{bridge}/I^{\sigma+}_0 = \cos 2(\theta - \theta_F)$.

The following combination of normalized signals helps to get rid of any parasitic constant rotations components:

$$\begin{aligned}(I^{\sigma+}_N - I^{\pi+}_N) - (I^{\sigma-}_N - I^{\pi-}_N) &= (\cos 2(\theta - \theta_F) - \cos 2\theta) - (\cos 2(\theta + \theta_F) - \cos 2\theta) \\ &= 2 \sin 2\theta \sin 2\theta_F.\end{aligned} \tag{4.12}$$

The analysis angle θ and Faraday rotation θ_F dependencies of the resulting combination is of the same form as the MO contrast in Eq. 2.26, and for small Faraday rotations $\theta_F \ll 1$ and for a fixed analysis angle corresponding to the balanced bridge condition, $\theta = \pi/4$ radians, we can find from Eq. 4.12 the Faraday rotation angle to be:

$$\theta_F = \frac{1}{4}\big((I^{\sigma+}_N - I^{\pi+}_N) - (I^{\sigma-}_N - I^{\pi-}_N)\big). \tag{4.13}$$

It is rather important to note that in this work the Faraday rotation angle is given in radians, which is accomplished by measuring two quantities: differential bridge signal and the sum intensity signal one after the other, required for normalization of the signal. This might not be beneficial as we do not do simultaneous measurements in the system which might fluctuate and thus introduce some artificial noise to the measurement. Such separated in time measurement can not be done, for example, when a time resolved Faraday rotation (TRFT) spectroscopy is performed (Kikkawa

and Awschalom, 1999), or, when using a photoelastic modulator (PEM) as in works by Crooker et al., 2007, for example. We have attempted the measurements with the PEM during the course of the thesis work. It was used in combination with a PGC technique, discussed earlier in application to the Sagnac interferometer (see Eq. 2.37 from Chapter 2), which actually allows for the simultaneous measurement of differential and intensity signal in the first and second harmonics, leading to the instant normalization of Faraday rotation. However, the PEM was inducing some parasitic dark signal at 50 kHz that has prevented us from increasing the sensitivity of the measurement. The optical bridge performance has shown better results in comparison with this technique.

The function of a dichroic mirror is to bring the two laser beams to the same spot on the sample surface, and so the dichroic mirror in Fig. 4.5 transmits the probe laser light and reflects the pump laser light. The alignment procedure is done at this point by looking at the sample surface with a camera installed above the optical components while tuning the position of the mirror attached to a 5 axis manual-adjustment mount.

With this state of the experimental setup it was possible to resolve small Faraday rotations less than 1 μrad in magnitude that will be shown in the next section. Further setup development and some major modifications to the experimental setup will be discussed along with presenting the results.

4.5 Experimental results for photoinduced Faraday rotation in GaAs

The measurements of optically pumped GaAs sample of doping density $n = 5.5 \times 10^{15}$ cm^{-3} and 500 μm thickness have started in the experimental setup configuration represented schematically in Fig. 4.7. The probe laser used was a solid state laser of wavelength λ = 970 nm ($\hbar\omega$ = 1.28 eV), which lies in the transparency region, away from the absorption edge. At this stage of experimental setup development the two lasers were not collinear on the sample making an angle $\sim 12^\circ$ and two separate lenses of focal lengths f_1 = 150 mm and f_2 = 125 mm were used to focus the laser beams on the sample. A very rough alignment of the two beams was performed by looking at the near infrared card put close to the sample surface while blocking and unblocking one of the lasers.

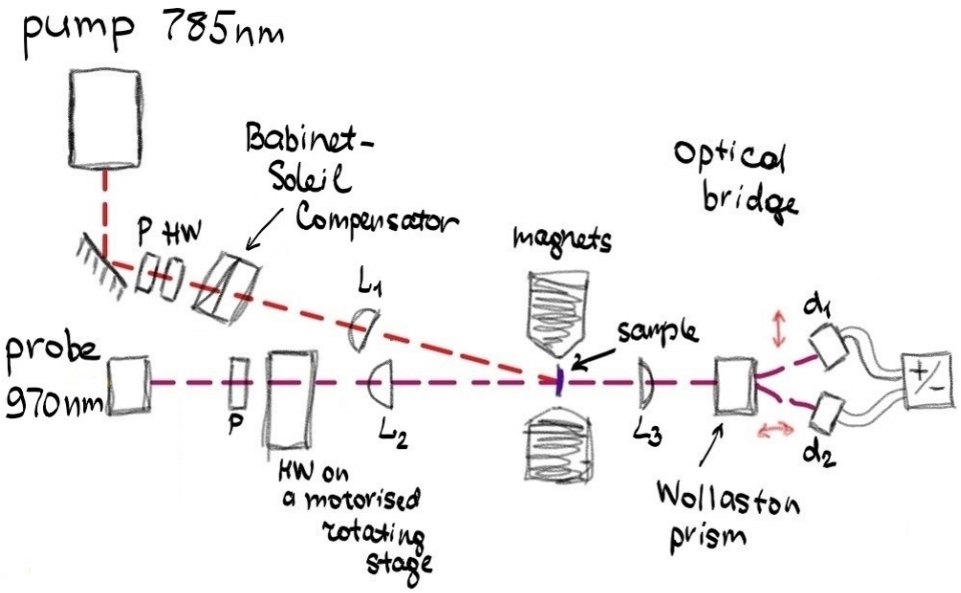

FIGURE 4.7: The experimental setup state at the moment of first successful Hanle curve measurement. The laser beams are not collinear which rendered the alignment procedure difficult diminishing the Faraday rotation angles.

Transverse magnetic fields from an electromagnet of maximum value B = 0.25 T were applied symmetrically in order to observe the Hanle effect of depolarization of spin ensemble. The room temperature Faraday rotation Hanle data are shown in Fig. 4.8. The poor quality of the laser that we used in this experiment and the alignment of the laser beams "by eye" have prevented us from getting clean data within reasonable acquisition times, so each data point is accumulated for at least 2 hours and the points with the smallest error bars are taken overnight. The maximum Faraday rotation angle obtained in this measurement is equal to 0.93 ± 0.14 μrad in the absence of applied magnetic field. The data within the error bars fit a Lorentzian distribution centered at 0 applied field, and the half-width is found to be B_{HWHM} = 0.13 T.

The 970 nm solid state laser was replaced by less noisy temperature controlled 1.3 μm laser. Although this wavelength is not well adapted as a probe wavelength for GaAs, we still have found the same order of magnitude Faraday rotation angles, and we believe this is mainly due to the next modification to the setup, which was to make the two laser beams incidence on the sample normal. There were several reasons to do this, first of all, to eliminate the concern of changing Fresnel coefficients with polarization of the pump. Secondly, by doing so we simplified and improved significantly the alignment procedure. Finally, the normal incidence for both beams

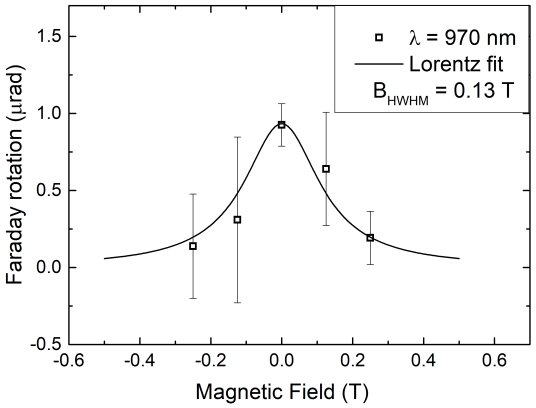

FIGURE 4.8: Faraday rotation as a function of applied transverse magnetic field measured in bulk GaAs of doping density $n = 5.5 \times 10^{15}$ cm^{-3} at room temperature for probe wavelength λ = 970 nm. The data is fitted with a Lorentz function centered at 0 field.

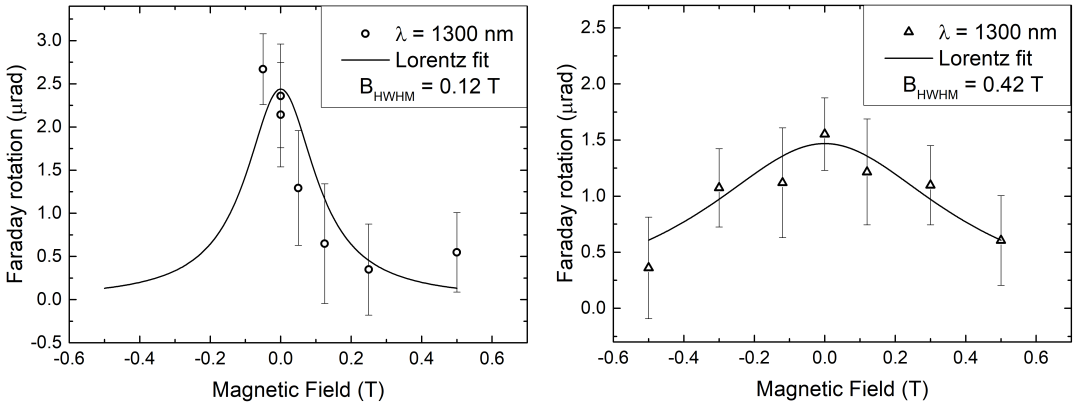

FIGURE 4.9: Faraday rotation as a function of applied transverse magnetic field measured in bulk GaAs of doping density $n = 5.5 \times 10^{15}$ cm^{-3} at room temperature for probe wavelength λ = 1300 nm. The data is fitted with a Lorentz function centered at 0 field. The estimated Hanle halfwidth is (a) 0.12 T and (b) 0.42 T.

is practical in the case of putting the sample in a cryostat.

From this moment on, the experimental setup looked like that represented in the Fig. 4.5 used with 785 nm laser as the pump laser source and 1.3 μm ($\hbar\omega$ = 0.95 eV) laser as a probe source. The updated geometry of the experiment has allowed us to use the smallest focal length (f = 75 mm) lens as an input lens, which resulted in slightly smaller sizes of the beams on the sample surface ($\sigma \sim 50$ μm). According to the Verdet coefficient versus photon energy dependence this particular choice of wavelength should lead to smaller Faraday rotations, but the better alignment of the laser beams and their smaller sizes have resulted in even larger rotations. The following two Hanle curves measured at different moments in time and possibly at random places on the sample surface and with differing alignment quality, are

shown in Fig. 4.9. This shows how crucial is the alignment of the two lasers characteristic to experiments with combined laser beams. The difference in the calculated Hanle halfwidths for the two measurements (0.12 T and 0.42 T) suggests the inhomogeneity of the sample surface.

The final experimental configuration

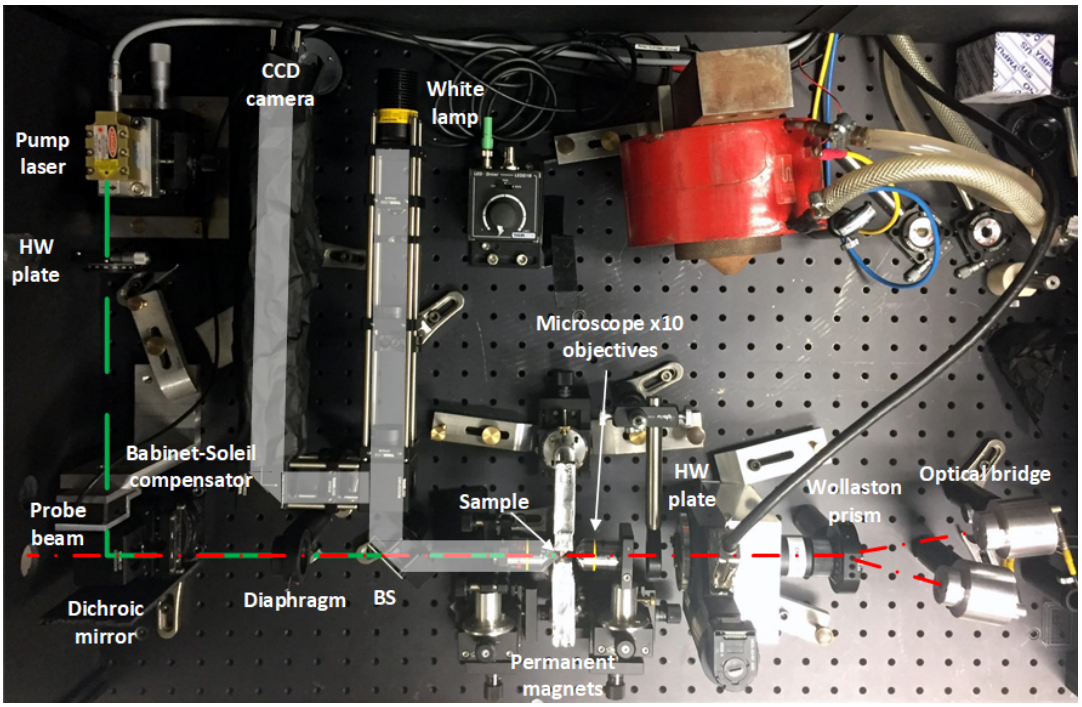

FIGURE 4.10: The final configuration of the experimental setup. The probe laser is a Ti:Sapphire CW tunable wavelength laser that comes through a hole in the box where the setup is mounted. Uncorrelated light from the white lamp is used at the moment of the laser beams alignment on the sample when the image of the two lasers is recorded with a CCD camera.

A photograph of the final experimental configuration is shown in Fig. 4.10. The most important steps toward larger rotation angles with respect to the previous results were the addition of the imaging optics that made it much simpler to align the lasers and actually verify their collinearity, and the use of microscope x10 objectives to focus the beams onto the exact same spot on the sample. The spot size achieved is of the order of 8 μm for both lasers as evidenced from the images on the CCD camera.

The probe laser used in this configuration is a CW Ti-Sapphire laser used within the range of wavelength $\lambda \in [880; 900]$ nm. The pump laser is the same 785 nm source of power = 50 mW of modulated polarization between circular and linear

as described in the section 4.4.3. The Faraday rotation induced by optical pumping has been scanned in the mentioned wavelength range, and the resulting spectrum is plotted in Fig. 4.11 with the absorption spectrum on the right Y-axis. The two data sets represent Faraday rotation in zero field (squares) and Faraday rotation under the applied transverse magnetic field of value 0.235 T (circles) from one permanent magnet positioned close to the sample.

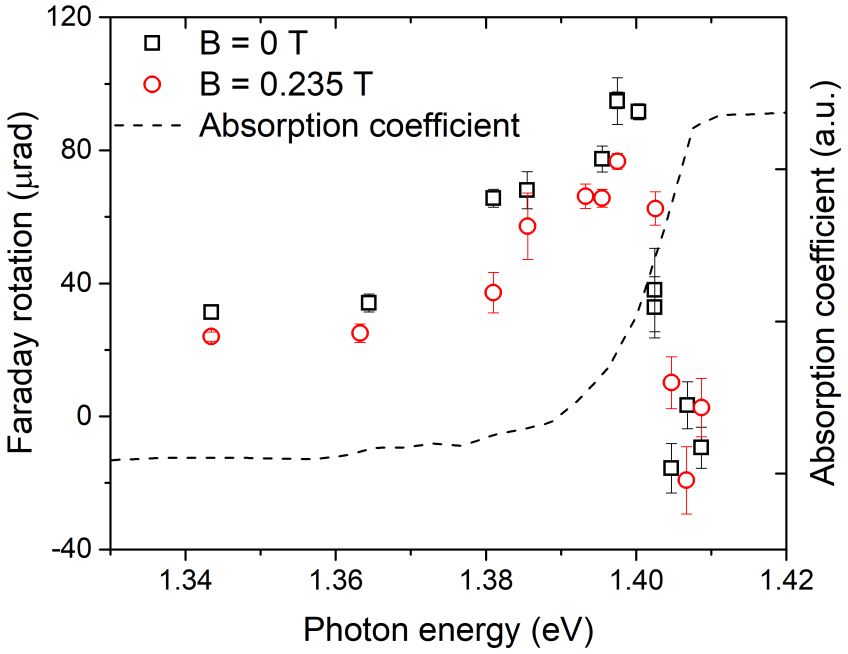

FIGURE 4.11: Photoinduced Faraday rotation angles in sample of GaAs ($n = 5.5 \times 10^{15}$ cm^{-3}). The data are taken in zero magnetic field (squares) and in 0.235 T transverse applied field (circles). The absorption coefficient spectrum is plotted along the right Y-axis.

We can see already that for all photon energies the change in rotation angles in the field is constant, which signifies independence of the Hanle effect on the probe photon energy. It shows that the precession in the applied transverse field is indeed just the spin related effect. If we multiply the Faraday rotation spectrum by 1.3 coefficient, it falls nicely on top of the zero-field spectrum.

Now we want to compare the Faraday rotation induced by optical pumping and the classic version of Faraday rotation in a longitudinal magnetic field measured and described previously (see Chapter 3) and plot them together with the absorption coefficient (see Fig. 4.12). To bring the classical Faraday rotation measured in the field of 0.22 T on the same scale as the photoinduced Faraday rotation we had to divide it by the factor 100. In Chapter 3 we have already demonstrated the striking similarity of the field-induced Faraday rotation with the first derivative of absorption

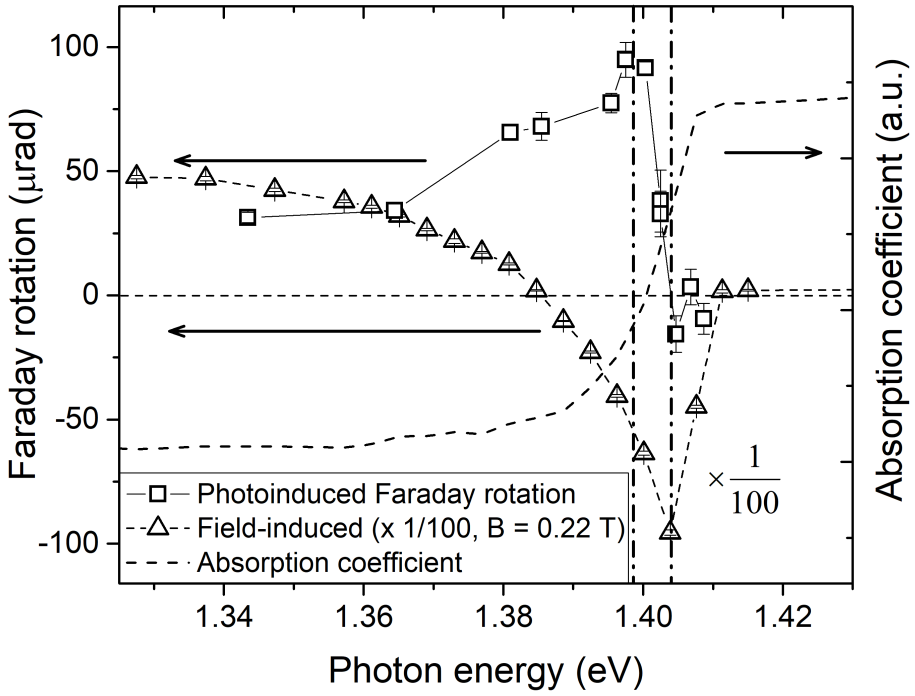

FIGURE 4.12: Comparison of photoinduced Faraday rotation angles (squares) and field-induced Faraday rotation angles (triangles) in sample of GaAs ($n = 5.5 \times 10^{15}$ cm^{-3}). The absorption coefficient (dashed line) is shown on the right Y-axis. The two vertical dash-dotted lines mark the peaks of the Faraday rotation spectra (at 1.399 eV and 1.404 eV) of differing nature.

coefficient. The photoinduced Faraday rotation, however, does not follow the field-induced Faraday rotation curve. Its peak value ($\sim$ 1.399 eV) is shifted from the peak of field-induced rotation ($\sim$ 1.404 eV) by $\sim$ 5 meV. This shift might be interpreted as follows. Let us look at the temperature dependence of the energy band gap for GaAs (from *Temperature dependence of the energy gap (GaAs)*):

$$E_g = 1.519 - \frac{5.405 \cdot 10^{-4} \cdot T^2}{T + 204}(\text{eV}), \tag{4.14}$$

where T is a temperature in degrees K ($0 < T < 10^3$). The energy shift of -5 meV when switching from field-induced Faraday effect experiment to the photoinduced one, corresponds to a rise in the temperature of $\Delta T = 10$ K from room temperature. Considering the power densities of pump light that is present in the photoinduced Faraday experiment only, it is probable that this shift is due to the local heating of the lattice induced by the optical pumping process.

In contrast to the field-induced rotation again, the decay of photoinduced Faraday rotation curve is much slower in the range of energies close to the band gap, and it does not change sign for decreasing probe photon energies. Such differing from the classical Faraday rotation dependence could be expected taking into account the fact that the formula from Eq. 2.2 does not describe the case of optical pumping, so the straightforward relation between the Faraday rotation in this case and the refraction index derivative does not necessarily remain true. This difference has been treated elsewhere (Giri et al., 2012), but the details are still not clear.

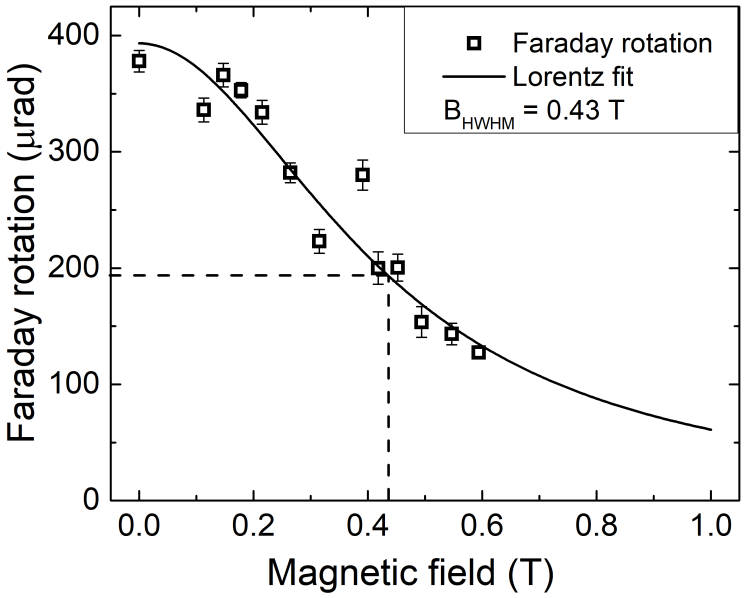

FIGURE 4.13: Hanle effect measurement on Faraday rotation under optical pumping conditions performed on the sample of GaAs. The characteristic halfwidth of the Lorentzian distribution is calculated from the fit: B_{HWHM} = 0.43 T.

By scanning the probing energies we were able to find the optimum wavelength for Hanle type measurements, $\lambda = 888$ nm, which corresponds approximately to the maximum angle along the spectrum. This procedure is often done in the literature for even sharper absorption coefficient spectra (at low temperatures Yang et al., 2015; Crooker et al., 2007; Furis et al., 2007). In contrast with previous Hanle curves (see Figs. 4.8 and 4.9), the magnetic field is generated with two permanent magnets on each side of the sample dictated by the new geometry of the experiment, one magnet is fixed and another one is mounted on a moving translation stage, thus we were able to draw only one half of the Hanle curve, as shown in Fig. 4.13. By bringing the magnets closer together the field is increased to its maximum value of 0.6 T. The progress in the alignment procedure has allowed us to make the integration

times much shorter (30 sec) and the measurement much faster, in addition to an important increase in the values of the rotation angles which grew from 1 μrad to 100 μrad and to slightly less than 400 μrad after a realignment and an examination of the collinearity of the laser beams. Figure 4.13 also shows a Lorentzian fit of the Faraday rotation data taken under the optical pumping conditions in an unintentionally doped sample of GaAs, from which a value of Hanle halfwidth can be estimated: $B_{HWHM} = 0.43$ T. Recalling the relation between the spin relaxation time and the Hanle halfwidth: $\tau_s = \frac{\hbar}{\mu_B g B_{HWHM}}$ described in Eq. 4.10, the spin lifetime can be thus extracted from the Hanle measurement: $\tau_s = 88$ ps.

In the PL experiment described in Section 4.2, we have identified the ratio of $\tau_s/\tau = 0.137$. Although combining the results from two distinct experiments must be taken with cautious, the excitation densities in the two experiments are comparable. The pump laser in the PL experiment has power of 1 mW and is focused to a beam of radius 0.5 μm, the beam size in the photoinduced Faraday rotation measurement is larger (3 μm) but it is compensated by larger excitation powers ($\approx$ 50 mW). So knowing the spin lifetime we can try to deduce the carrier lifetime $\tau = 0.64$ ns, and using Eq. 4.5 the spin relaxation time T_1 can be estimated as well: $T_1 = 77$ ps. Looking at the values for lifetimes in n-type GaAs for different doping densities (see Fig. 4.14), our extracted lifetime τ of 0.64 ns seems short for electron concentration that we have ($n = 5.5 \times 10^{15}$ cm^{-3}). But considering our experimental conditions: pump laser of power $P_{\text{pump}} = 50$ mW, concentrated in a volume $\mathbb{V} = \sigma^2/\alpha$, where α is an absorption coefficient of GaAs at photon energy $E = 1.58$ eV, and σ is a diameter of the laser spot, we can estimate the carrier generation rate G to be:

$$G = \frac{P_{\text{pump}}}{eE}\frac{\alpha}{\sigma^2} \approx 10^{28}\text{cm}^{-3}\text{s}^{-1}. \tag{4.15}$$

Using this generation rate and the value for the lifetime τ we can then estimate the density of carriers in the steady state regime:

$$\Delta n = \Delta p = G\tau \approx 6 \times 10^{18}\ \text{cm}^{-3} \gg n = 5.5 \times 10^{15}\ \text{cm}^{-3}, \tag{4.16}$$

which turns out to be much larger than the equilibrium electron density in the sample. It indicates strong injection regime, in which we should be expecting the lifetimes to be a lot shorter than they normally are. Still, on the graph of lifetimes versus doping densities from the literature (Fig. 4.14), our found point marked by an arrow

in figure and defined by the lifetime of 0.64 ns and the concentration Δn of 6×10^{18} cm^{-3} falls nicely on top of the predicted curve for the room temperature hole lifetimes.

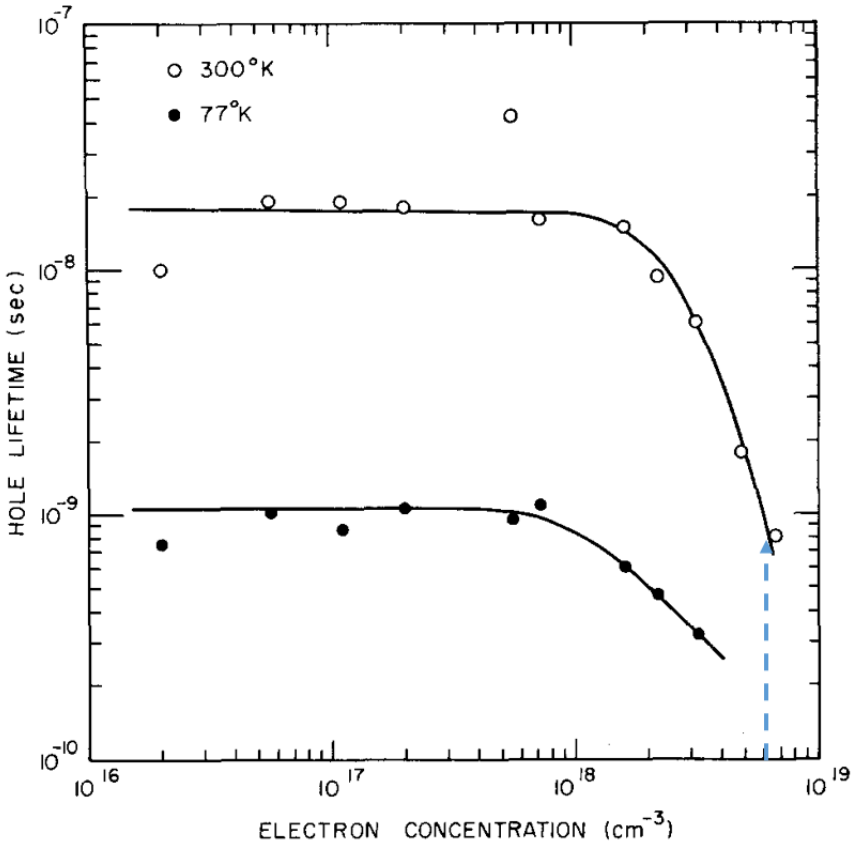

FIGURE 4.14: Doping dependence of hole lifetime in n-type GaAs (graph extracted from Hwang, 1971).

Chapter 5

Conclusions and perspectives

In this work, the experimental measurement technique based on the magneto-optical Faraday effect has been investigated with the intention to study spin dynamics in non-magnetic semiconductors when pumped with circularly polarized light. Among three possible optical detection techniques of electron spin: polarized photoluminescence, spin polarized photoemission spectroscopy and magnetometry based on MOKE or Faraday effect, we have shown that the use of the magneto-optical techniques has several potential advantages.

From the comparison of different magnetometers in terms of their sensitivity and ease of use in application to the optically pumped semiconductors, the MOKE magnetometer has been chosen as the most appropriate technique, capable of working within nonmagnetic semiconductors as justified by the literature (Giri et al., 2013; Kikkawa and Awschalom, 1999; Kato et al., 2004; Furis et al., 2007).

Three detection schemes with which the Faraday rotation measurement is usually achieved have been compared: partially crossed polarizers, a modified Sagnac interferometer and an optical bridge. The functional equivalence of partially crossed polarizers with Sagnac interferometer has been confirmed by comparing the figures-of-merit, although the practical performance of the Sagnac interferometer is compromised by lost photons at each of the required beam splitters. Four modifications of the Sagnac interferometer has been proposed, that, combined with the PGC detection method, are capable to differentiate between the physical phenomena of various time and space symmetry. Due to the common mode rejection ratio of the optical source noise in the balanced optical bridge, it is able of photon shot noise limited measurements with large photon intensities on each of the two detectors. The noise floor for the Faraday rotation measurement of 1.3 nrad$/\sqrt{\text{Hz}}$ has been demonstrated

in the optical bridge configuration in the measurement of field-induced Faraday rotation in a TGG crystal.

With the optical bridge technique under balanced condition, a classical in-field Faraday rotation measurement has been performed on a sample of unintentionally doped bulk GaAs ($n = 5.5 \times 10^{15}$ cm^{-3}). The probe photon energy has been changed and the variation of the Verdet constant is registered and compared with the equivalent experiment from the literature (Gabriel and Piller, 1967).

Furthermore, the polarized photoluminescence experiment has been carried out on the same GaAs sample, from which the ratio of spin to carrier lifetimes has been found. A series of steady-state pump and probe measurements has been realized where the probe photon energy dependency of the Faraday rotation is studied experimentally first, in order to tune to the peak magnitude of the rotation angle. When the probe energy that maximizes the signal has been found, a transverse to the light direction of propagation magnetic field is applied and the Hanle effect of depolarization of spin population is observed. From this measurement, the value of Hanle half-width is found (0.43 T) and the spin lifetime τ_s = 88 ps is calculated.

Although there are established experimental techniques that are successfully used to study spin dynamics in GaAs, our built magnetometer is potentially better suited to study spin dynamics in indirect semiconductors, such as Silicon. Due to its small atomic number, a spin-orbit coupling is weaker in silicon as compared with other semiconductors, that results in slower spin-orbit induced spin relaxation. In addition, the most important spin relaxation mechanism in widely studied GaAs, the Dyakonov-Perel mechanism, is simply absent in silicon as it possesses an inversion symmetry. This suggests that the electron spins in silicon could be transported over longer times and larger distances.

There are several theoretical studies aiming to calculate optical selection rules involving phonon interactions for indirect band gap materials (Li and Dery, 2010; Cheng et al., 2011) that we discuss in more details in Appendix B, yet little things are studied experimentally. The polarized photoluminescence signal due to the indirect nature of the band gap in silicon is immeasurably small (Roux, 2008), the attempted photoemission spectroscopy has not revealed any signal at the fundamental band gap (Favorskiy, 2013). Due to the relation of the measured magnetization to the spin population and not to the polarization, the magneto-optic magnetometer can in principle be able to detect spin in silicon.

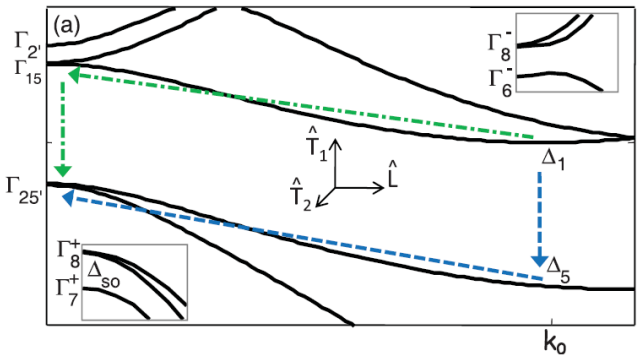

FIGURE 5.1: Band structure of silicon along Δ direction in the reciprocal space with symmetries of all states included in the calculation by Li and Dery.

However, due to the weak spin-orbit interaction in atomically light silicon and the assistance of phonon modes in the fundamental optical transitions, the range of wavelengths capable of inducing non-equilibrium spin population is very narrow (Cheng et al., 2011) around the fundamental band gap energy E_g = 1.12 eV (the aspects of optical pumping the fundamental gap of silicon are described in Appendix B). In addition, as it is shown in the thesis, the Faraday rotation angles are maximized close to the band edge too, and the accurate prior investigation of the dependence of Faraday rotation on the probe energy is required. In this case, we would need two tunable wavelength lasers: the probe and the pump, which would be very close in wavelength. This, in turn, could lead to practical difficulties in finding the filter of the exact cut off wavelength. In addition, according to one of the most important practical realizations of the work, the imaging optics is very important for the alignment of the lasers, but in the far infrared it is also more expensive. Finally, compared with GaAs, silicon has much smoother absorption coefficient wavelength dependency, which should result in smaller Faraday rotation.

Appendix A

Generalized form of Jones matrices for phase retarders, polarizers, mirrors and beam splitters

A.1 Phase retarder

The general form of Jones' matrix for a linear phase retarder introducing ϕ_x phase delay to the x-component of polarization and ϕ_y phase delay to the y-component of light polarization (relative retardation between fast and slow axes of $\phi_x - \phi_y$):

$$\mathbf{PR}(\phi_x, \phi_y, q) = \begin{pmatrix} e^{i\phi_x}\cos^2 q + e^{i\phi_y}\sin^2 q & (e^{i\phi_x} - e^{i\phi_y})\cos q \sin q \\ (e^{i\phi_x} - e^{i\phi_y})\cos q \sin q & e^{i\phi_x}\sin^2 q + e^{i\phi_y}\cos^2 q \end{pmatrix}, \tag{A.1}$$

where q is the angle that fast axis makes with x-axis.

A.2 Linear polarizer

The general Jones' matrix for a linear polarizer is given by

$$\mathbf{P}(\theta_P) = \begin{pmatrix} \cos^2\theta_P & \sin\theta_P \cos\theta_P \\ \sin\theta_P \cos\theta_P & \sin^2\theta_P \end{pmatrix}. \tag{A.2}$$

Angle θ_P here is the angle between the fast axis of a polarizer and x-axis.

A.3 Mirrors

A Jones' matrix for a perfect metallic mirror at normal incidence is used throughout the work:

$$\mathbf{M} = \begin{pmatrix} 1 & 0 \\ 0 & -1 \end{pmatrix}. \tag{A.3}$$

From the expression it can be seen that a π shift is introduced between x- and y-components of light, however a successive action of two mirrors results in the identity matrix. In all Sagnac geometries presented here we use two mirrors inside loops and therefore their matrices can be omitted from the calculations.

Appendix B

Optical pumping in silicon

The first experiment on the optical spin orientation of electrons in solids was conducted by Georges Lampel in 1968 (Lampel, 1968). For this purpose he used Si^{29} which was illuminated with unpolarized light at first and then with circularly polarized light. The polarization of the electrons was estimated to be - 0.4%, which is due to unfavorable ratio of spin relaxation time and electron lifetime, but it was sufficient for polarizing the lattice nuclei via interaction between nuclear spin and spin of free carriers. The enhancement in nuclear spin polarization was detected by the conventional NMR technique.

This result has launched numerous researches of optical pumping in semiconductors. They were conducted mainly in direct, III-V semiconductors, because of the efficiency of polarized photoluminescence technique: in GaSb by Parsons, in alloys GaAlAs by Ekimov and Safarov, in GaAs by Zakharchenya et al.

In silicon, however, because of the indirect nature of the band gap the polarized photoluminescence technique turned out to be inefficient. The details are going to be discussed in the following sections.

B.1 Band structure of Silicon. Symmetries of states at Γ point. Selection rules for direct transitions.

Let us take a look at the energy band diagram of silicon, illustrated in Fig. B.1. The difference with GaAs is quite obvious: the bottom of conduction band does not coincide with the top of the valence band. It implies that in indirect optical transitions the created electron and hole have different crystal momenta and phonon emission or absorption processes are required to conserve the total wave vector. This makes the optical pumping, as well as the radiative recombination in indirect band

gap semiconductors, less probable to occur, that, in turn, suggests that the electron lifetime is much longer than that in direct semiconductors.

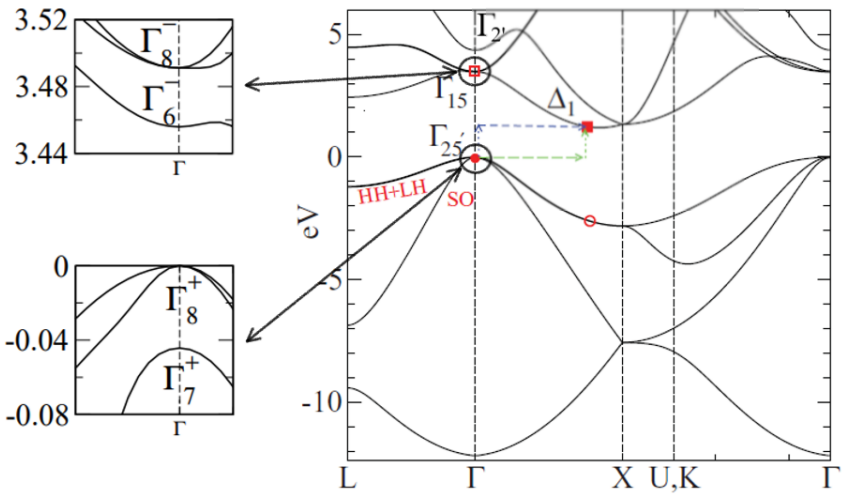

FIGURE B.1: Silicon band structure, calculated from an empirical pseudopotential method. In blue and green are the two important paths for optical transitions at the band edge. Dotted lines represent photons, while dashed lines represent phonons. The figure is taken from Cheng et al., 2011.

Figure B.1 shows the energy band diagram of silicon along the main directions in the reciprocal space calculated using an empirical pseudopotential model (Cheng et al., 2011). Some basic information on the parameters of the band structure at 300 K is listed below:

- E_g = 1.12 eV - the fundamental indirect band gap;
- E_X = 1.2 eV - the energy difference at X point in the reciprocal space;
- E_L = 2.0 eV - the energy difference at L point in the reciprocal space;
- $E_{\Gamma 1}$ = 3.4 eV - the first direct band gap (at Γ point in the reciprocal space);
- $E_{\Gamma 2}$ = 4.2 eV - the second direct band gap.

At the Γ point, the highest valence band states are *p*-like and in the absence of SOI transform according to the representation Γ'_{25} in the notation by Bouckaert, 1936 (BSW notation). After the application of SOI the energy shift between degenerate HH and LH bands and SO band appears as it is shown on the lower inset of Fig. B.1. It is equal to Δ_{SO} = 44 meV, that is much smaller than in GaAs. As a result of SOI, the symmetry operations of the states include symmetry operations of the spin wave function, and in the double group notations (Cohen and Chelikowsky, 2012) the HH

and LH bands belong to Γ_8^+ representation, and the SO band belongs to Γ_7^+. The valence band states become spin mixed states and their eigenstates can be written using basis functions of the group representation Γ'_{25}: $\{yz, zx, xy\} = \{\mathcal{X}, \mathcal{Y}, \mathcal{Z}\}$ as:

$$
\begin{aligned}
\Gamma_8^+ \text{ states: } \left|\frac{3}{2}, +\frac{3}{2}\right\rangle &= -\frac{1}{\sqrt{2}}|\mathcal{X} + i\mathcal{Y}\rangle|\uparrow\rangle, \\
\left|\frac{3}{2}, -\frac{3}{2}\right\rangle &= \frac{1}{\sqrt{2}}|\mathcal{X} - i\mathcal{Y}\rangle|\downarrow\rangle, \\
\left|\frac{3}{2}, +\frac{1}{2}\right\rangle &= \sqrt{\frac{2}{3}}|\mathcal{Z}\rangle|\uparrow\rangle - \frac{1}{\sqrt{6}}|\mathcal{X} + i\mathcal{Y}\rangle|\downarrow\rangle, \\
\left|\frac{3}{2}, -\frac{1}{2}\right\rangle &= \frac{1}{\sqrt{6}}|\mathcal{X} - i\mathcal{Y}\rangle|\uparrow\rangle + \sqrt{\frac{2}{3}}|\mathcal{Z}\rangle|\downarrow\rangle, \\
\Gamma_7^+ \text{ states: } \left|\frac{1}{2}, +\frac{1}{2}\right\rangle &= \frac{1}{\sqrt{3}}|\mathcal{Z}\rangle|\uparrow\rangle + \frac{1}{\sqrt{3}}|\mathcal{X} + i\mathcal{Y}\rangle|\downarrow\rangle, \\
\left|\frac{1}{2}, -\frac{1}{2}\right\rangle &= \frac{1}{\sqrt{3}}|\mathcal{X} - i\mathcal{Y}\rangle|\uparrow\rangle - \frac{1}{\sqrt{3}}|\mathcal{Z}\rangle|\downarrow\rangle.
\end{aligned}
\tag{B.1}
$$

The first two lines in Eq. B.1 correspond to the states in HH band, the second two to the LH band and the last two to the SO band; up and down arrows signify spin direction.

The conduction band states at the center of Brillouin zone are also p states with Γ_{15} symmetry in the BSW notation. There is an energy shift between the conduction band states at Γ point of Δ_{SO}^C = 32 meV according to Nastos et al., 2007, shown in the upper inset in Fig. B.1. In the double group notation (Cohen and Chelikowsky, 2012) the lower two states have Γ_6^- symmetry and the higher four states have Γ_8^- symmetry. These electronic states written with basis functions of Γ_{15} representation

- $\{x, y, z\}$ are:

$$
\begin{aligned}
\Gamma_6^- \text{ states: } \left|\frac{1}{2}, +\frac{1}{2}\right\rangle &= \frac{1}{\sqrt{3}}|z\rangle|\uparrow\rangle + \frac{1}{\sqrt{3}}|x+iy\rangle|\downarrow\rangle, \\
\left|\frac{1}{2}, -\frac{1}{2}\right\rangle &= \frac{1}{\sqrt{3}}|x-iy\rangle|\uparrow\rangle - \frac{1}{\sqrt{3}}|z\rangle|\downarrow\rangle, \\
\Gamma_8^- \text{ states: } \left|\frac{3}{2}, +\frac{3}{2}\right\rangle &= -\frac{1}{\sqrt{2}}|x+iy\rangle|\uparrow\rangle, \\
\left|\frac{3}{2}, -\frac{3}{2}\right\rangle &= \frac{1}{\sqrt{2}}|x-iy\rangle|\downarrow\rangle, \\
\left|\frac{3}{2}, +\frac{1}{2}\right\rangle &= \sqrt{\frac{2}{3}}|z\rangle|\uparrow\rangle - \frac{1}{\sqrt{6}}|x+iy\rangle|\downarrow\rangle, \\
\left|\frac{3}{2}, -\frac{1}{2}\right\rangle &= \frac{1}{\sqrt{6}}|x-iy\rangle|\uparrow\rangle + \sqrt{\frac{2}{3}}|z\rangle|\downarrow\rangle.
\end{aligned}
\tag{B.2}
$$

We can look at the **direct optical transitions** at the center of Brillouin zone of Si to start with. Such transitions are analogous to the transitions in GaAs and have been studied thoroughly by Nastos et al., 2007.

In order to divide forbidden and allowed transition and determine the relative intensities of the latter we need to look at the terms of the form $\langle CB|\boldsymbol{p}|VB\rangle$, where CB and VB are electronic states in conduction and valence bands, correspondingly, and the electron momentum operator $\boldsymbol{p}$ describes the direct optical transitions in electric-dipole approximation.

According to matrix-element theorem from group theory (Yu and Cardona, 2010) allowed transitions, or non zero components of matrix elements for electric-dipole transitions, can be found: $\langle x|p^y|\mathcal{Z}\rangle = \langle y|p^z|\mathcal{X}\rangle = \langle z|p^x|\mathcal{Y}\rangle = \langle y|p^x|\mathcal{Z}\rangle = \langle z|p^y|\mathcal{X}\rangle = \langle x|p^z|\mathcal{Y}\rangle$.

The density matrix formalism is introduced at this point to conduct a link between the degree of spin polarization (P_i), and the symmetries of closely located states, and the expression for density matrix itself is the sum over:

$$
\rho = \sum_{\bar{n}\in VB} p^+ \left|VB_{\bar{n}}\right\rangle\left\langle VB_{\bar{n}}\right| p^- \tag{B.3}
$$

And the spin matrix associated with spin momentum :

$$
S_z = \sum_{\bar{m}\in CB} \left|CB_{\bar{m}}\right\rangle\left\langle CB_{\bar{m}}\right|\sigma_z \tag{B.4}
$$

The average degree of spin polarization (P_i) has the following expression:

$$\langle S_z \rangle = \frac{\text{trace}[\rho S_z]}{\text{trace}[\rho]} \tag{B.5}$$

For σ^+ circular polarization of pump light the initial polarization for excitation energies just above the first direct gap (when only $\Gamma_8^+ \rightarrow \Gamma_6^-$ direct transitions included) equals to

$$P_i[\Gamma_8^+ \rightarrow \Gamma_6^-] = \frac{1}{6} \tag{B.6}$$

When the excitation energy lies between $\hbar\omega \in [E_{\Gamma 1} + \Delta_{SO}^C; E_{\Gamma 1} + \Delta_{SO}]$ the $\Gamma_8^+ \rightarrow \Gamma_8^-$ transitions start to contribute to the total polarization, which in this case equals to

$$P_i[\Gamma_8^+ \rightarrow \Gamma_6^-, \Gamma_8^-] = \frac{1}{4} \tag{B.7}$$

(for more details see Roux, 2008). For excitation energies exceeding $\hbar\omega > E_{\Gamma 1} + \Delta_{SO}$, i.e. by considering overall transitions from $\Gamma_{25}' \rightarrow \Gamma_{15}$ band, the polarization drops to 0.

This was one example of how the inclusion of bands plays a significant role in the final polarization value. Because of the different symmetries and the closeness of the states, the important state mixing affects the degree of spin polarization. If we go further up to the next conduction band with representation Γ_2' and consider transitions $\Gamma_8^+ \rightarrow \Gamma_7^-$ we find that the polarization changes sign and equals to (Bona and Meier, 1985):

$$P_i[\Gamma_8^+ \rightarrow \Gamma_2'] = -\frac{1}{2} \tag{B.8}$$

Due to low SOI in silicon, fine tuning of the pump laser is required in order to reproduce the theoretical calculations. At such energies the mixing of states comes into play and experimentally that precludes from observing the right polarization ratios.

B.2 Selection rules for indirect optical transitions in silicon

The six conduction band minimuma: $\{X, \bar{X}, Y, \bar{Y}, Z, \bar{Z}\}$ lie along $\overrightarrow{\Gamma X}$ directions and transform according to the representation Δ_1 with basis functions {x,y,z}. In the process of optical pumping the indirect band gap the k-vector of light is usually by convention aligned with the Z axis, and the two conduction valleys along Z-direction are called longitudinal, or Z-valleys, the other four valleys are called transverse, X and Y-valleys. The values of electron polarization differ from different kind of valleys.

Now we are going to look at phonons, which, being an exclusive solids related phenomenon, play an important role in the case of indirect optical transitions. In silicon, there are 4 distinct phonon branches: transverse-acoustic (TA), longitudinal-acoustic (LA), transverse-optical (TO) and longitudinal-optical (LO). The dispersion curve of these four phonon branches is shown in Fig.B.2. The solid line representing calculations using adiabatic bond charge model (ABCM) fit the experiments (in circles) well. At the Brillouin zone center in silicon, i.e. at Γ point, optical phonons are degenerate with non-zero frequency (15.5 THz corresponding to 64 meV of energy), while acoustic phonons are degenerate with zero frequency. At k_0 point the associated energies of all 4 branches differ and equal to (in ascending order): $\hbar\Omega_{\boldsymbol{k}_c^0,TA}$ = 19 meV, $\hbar\Omega_{\boldsymbol{k}_c^0,LA}$ = 43 meV, $\hbar\Omega_{\boldsymbol{k}_c^0,LO}$ = 53 meV, $\hbar\Omega_{\boldsymbol{k}_c^0,TO}$ = 57 meV.

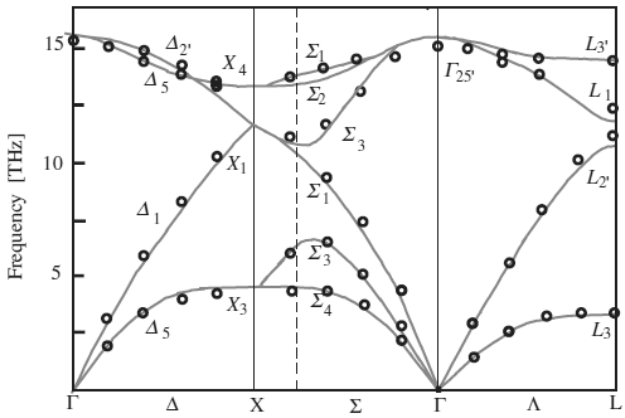

FIGURE B.2: Phonon dispersion curves along high-symmetry axes. The solid lines represent calculations using adiabatic bond charge model (ABCM) (Weber, 1977), while the circles are data points from Nilsson and Nelin, 1972 obtained by thermal-neutron spectroscopy. The figure is taken from Yu and Cardona, 2010.

Like electronic states, phonons can have symmetry properties with respect to the space symmetry of the crystal. In silicon along Δ-direction, the LA phonon mode

transforms according to the representation Δ_1 (basis function {z}), the LO phonon mode - according to the representation Δ_2' (basis function $\{x^2 - y^2\}$), and TA/TO phonon modes - according to Δ_5 representation with basis functions $\{x, y\}$.

In contrast to vertical transitions that include photons only, which makes the calculation of selection rules straightforward, in silicon the light absorption process is accompanied by the emission or the absorption of phonons, and so they need to be included in the derivation of optical selection rules. The indirect optical transition matrix elements are calculated using second-order perturbation theory and include electron-phonon and electron-photon interactions. (contain not only the electric-dipole operator but also the matrix elements of the electron-phonon interaction.) Accordingly, the transition occurs between the initial state $\left|i\right\rangle = \left|c\boldsymbol{k}_c\right\rangle$ and the final state $\left|f\right\rangle = \left|v\boldsymbol{k}_v\right\rangle$, where c and v stand for the conduction and valence band and reciprocal wave vectors equal to: $\boldsymbol{k}_v = 0, \boldsymbol{k}_c = \boldsymbol{k}_0$. This transition can be viewed as two successive scattering mechanisms with some kind of short-lived intermediate state in between. The energy in the overall absorption process is conserved, however, because of the small lifetime of this intermediate state, and due to the Heisenberg uncertainty, the energy may not be conserved in the transition to the intermediate state. In other words, the lifetime of the electron in the intermediate state is considered so short that the energy change can be greater than the photon energy $\hbar\omega$. The transition probability in the indirect optical absorption process is expressed in terms of electron-photon, or radiation-matter, interaction Hamiltonian H_l^{rm} and electron-phonon Hamiltonian H_λ^{ep} where l is the light polarization and λ corresponds to a particular phonon branch.

$$I_{\lambda,l} \propto \left| \sum_{n,m} \left[\frac{\left\langle f\right| H_\lambda^{ep} \left|n\right\rangle \left\langle n\right| H_l^{rm} \left|i\right\rangle}{E_i - E_n - \hbar\Omega_\lambda} + \right.\right. \\ \left.\left. + \frac{\left\langle f\right| H_l^{rm} \left|m\right\rangle \left\langle m\right| H_\lambda^{ep} \left|i\right\rangle}{E_i - E_m - \hbar\omega} \right] \right|^2 . \tag{B.9}$$

Two of the large amount of possible paths are considered in the paper by Li and Dery, 2010 and illustrated in the Fig. B.3. The term in the first line of the Eq. B.9 includes, among others, a transition represented by green arrows in the figure, where the directions of the arrows must be reverted in the case of the photon absorption processes (the paper deals with photoluminescence, which is the photon emission

process). In this process the electron from the initial state $|i\rangle$ in the conduction band is transitioned to the intermediate state $|n\rangle$ via an interaction with light (direct vertical arrow), followed by a phonon-assisted transition to the final state $|f\rangle$. The second line term includes the transition represented by blue arrows, where the electron first interacts with phonons that bring it to the intermediate state $|m\rangle$ from where it is transitioned to the final state by a photon.

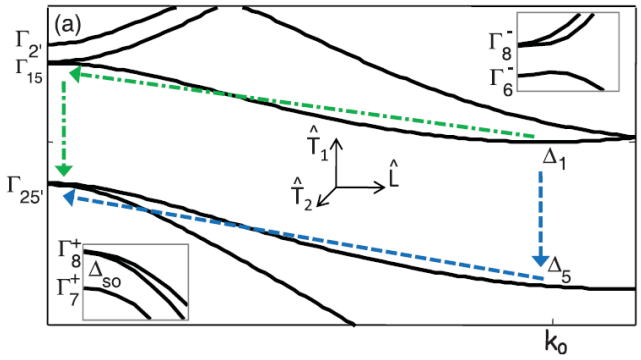

FIGURE B.3: Band structure of silicon along Δ direction in the reciprocal space with symmetries of all states included in the calculation by Li and Dery.

An important question emerges here: what are these intermediate states n and m and what symmetries do they have? It is natural to suggest that they are composed of all the real states at either $\boldsymbol{k}_v$ or $\boldsymbol{k}_c$ but taken with their own weights. For example, the Γ_6^- state would contribute to the virtual state n at Γ point with weight proportional to $I_n[\Gamma_6^-] \propto \left|\frac{1}{E_{\Gamma 1}-E_g}\right|^2 = \left|\frac{1}{3.4-1.12}\right|^2 = 0.192$, the contribution of Γ_8^- state is not so different: $I_n[\Gamma_8^-] \propto \left|\frac{1}{E_{\Gamma 1}+\Delta_{SO}^c-E_g}\right|^2 = \left|\frac{1}{3.4+0.032-1.12}\right|^2 = 0.187$. The weight of Γ_2' contribution is also considerable as it is close to Γ_{15} bands, and as we have seen in the previous, it leads to the polarization of different sign, and so the weight is $I_n[\Gamma_2'] \propto \left|\frac{1}{E_{\Gamma 2}-E_g}\right|^2 = \left|\frac{1}{4.2-1.12}\right|^2 = 0.105$.

The paper by Li and Dery calculates the degree of circular polarization of luminescence due to the recombination of spin-up electrons across the indirect band gap. Their calculation considers intermediate states to be real states in the conduction band at Γ point and in the valence band at $\boldsymbol{k}_0$ point. However, only the closest states (Γ_{15} and Γ_2' for LO-assisted transition) are involved which makes the overall picture incomplete in our opinion, in addition the corresponding transitions in their model are taken as equally weighted which contradicts our beliefs.

Cheng et al. claims that a single operator for both photon and phonon assisted processes can be built which makes it possible to not rely on the intermediate states

and their symmetries at all in the calculation of transition probabilities and keep the derivation in a general form. However, the justification of such method is not fully clear since, as we have seen for direct transitions, even in the conduction band at Γ point the symmetries of different electronic states lead to contrasting initial polarizations.

Despite all the differences of the discussed papers, the values of the calculated initial polarizations seem to be very close, as is shown in Table B.1. The LA phonon mode not taken into consideration does have small intensity but presents a large P_i.

TABLE B.1: Relative intensities I_r of phonon-assisted transitions and degrees of spin polarization P_i calculated from numerical models (EPM and ABCM) from the papers by Li and Dery, 2010 and Cheng et al., 2011. Transition intensities I_r are all normalized with respect to the TO intensity from transverse valleys. LA phonon is omitted from one of the papers due to negligible intensity. The calculations are given for σ^- light.

	Phonon mode		TA	LA	LO	TO
Li and Dery	X valley	I_r	0.086	–	0.115	1
		P_i	-36%	–	5.3%	-32.3%
	Z valley	I_r	0.092	–	0.23	1.41
		P_i	0.7%	–	50.1%	0.01%
	Total	I_r	0.53	–	0.92	6.82
		P_i	-23.5%	–	27.7%	-18.8%
Cheng et al.	X valley	I_r	0.045	0.014	0.174	1
		P_i	-32%	4%	6%	-28%
	Z valley	I_r	0.028	0.029	0.345	1.588
		P_i	0%	-51%	50%	-1%
	Total	I_r	0.238	0.116	1.388	7.167
		P_i	-25%	-24%	28%	-16%

When calculating the numbers in the Table B.1 authors considered the mere band edge transitions that included only HH and LH valence bands and phonon absorption processes. In practical conditions, first of all, it should be challenging to distinguish contributions from various phonon branches. The contributions from different valleys might be looked at separately in strained silicon with lifted valley degeneracy. Still, the comparison of theoretical investigations with experiments would be easier with some total P_i. In addition, due to non zero laser line-widths and weak absorption, the band edge transitions will be difficult to investigate.

B.3 Carrier and spin injection

The carrier and spin injection rates are investigated in the Cheng et al.'s paper for temperatures in the range 0 - 500 K and for photon energies starting from -57 meV below the band edge which corresponds to absorption of TO phonon. The absorption processes are frozen below $\approx$ 70 K, and above 70 K the injection rates increase nearly linearly with temperature for each of the phonon modes. The injection rates to longitudinal (Z) and transverse (X) valleys as well as total injection rate at temperatures 77 K and 300 K are shown in Fig. B.4 (a). All injection rates increase with photon energy that is in consistence with increasing joint density of states (JDOS) with photon energy.

The spin injection rates, however, change very little from 77 K to 300 K [see Fig. B.4 (b)]. The ensuing P_i is proportional to the ratio of spin injection rate to carrier injection rate and is included in the Fig. B.4 (b) too.

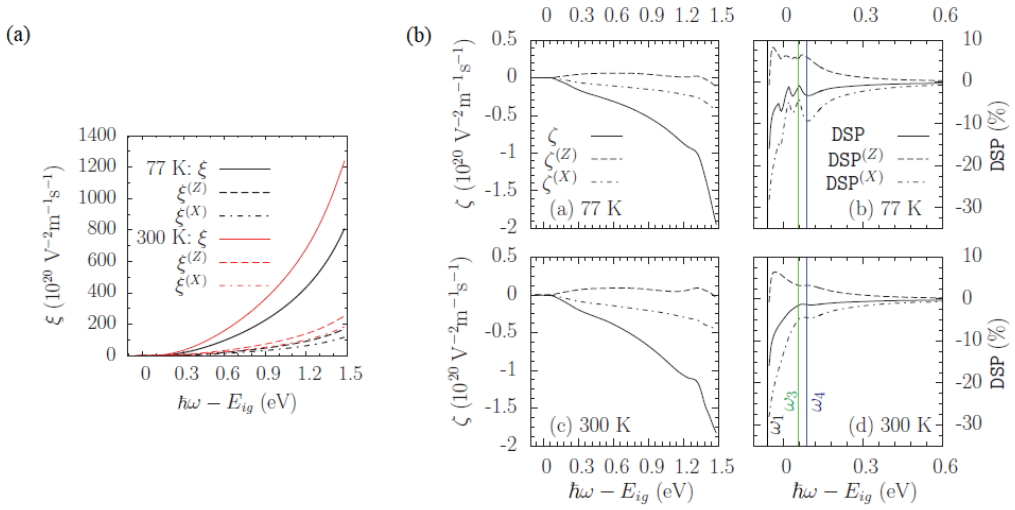

FIGURE B.4: Carrier (a) and spin (b) injection spectra

The maximum value of P_i both at 77 K and at 300 K equals to -15% and that is at the injection band edge where $\hbar\omega \approx E_g - \hbar\Omega_{TO}$. When the energy of photon increases different absorption and emission of phonon processes come into play, whence the fine structure of P_i curve which could be seen better at 77 K. they can have different signs and values depending on what phonon and what valley we consider. In addition, away from the band edge the important band mixing takes place, all of it makes the absolute value of P_i to disappear quickly, at $\hbar\omega = E_g$ the P_i

is less than 5% for both temperatures and it is less than 1% for $\hbar\omega \approx E_g + 0.22$ eV at 300 K and for $\hbar\omega \approx E_g + 0.28$ eV at 77 K.

B.4 Discussion of spin relaxation processes in silicon

For better functionality of spintronic devices the spin transfer over long distances and thus longer times is desirable. In year 2007 a remarkable experiment on spin propagation through a 350 μm undoped silicon wafer at liquid nitrogen temperatures was demonstrated (Huang, Monsma, and Appelbaum, 2007).

Among the four most important spin relaxation mechanisms: Elliott-Yafet, Dyakonov-Perel, Bir-Aronov-Pikus mechanisms and hyperfine-interaction mechanism, in lightly doped centrosymmetric semiconductors, the most prominent one is the Elliott-Yafet mechanism.

According to it, the spin relaxes due to momentum scattering off impurities and phonons. Cheng, Wu, and Fabian, 2010 analyses the process using a pseudopotential and ABC models and finds the temperature dependence of spin relaxation time $T_1 \sim T^{-3}$. Different set of experimental data from studies by Appelbaum, Huang, and Monsma, 2007; Huang, Monsma, and Appelbaum, 2007; Lépine, 1970; Lancaster, Wyk, and Schneider, 1964 is fit by the dependence which confirms that in bulk silicon the Elliott-Yafet mechanism is the dominant at ambient temperatures.

$T_1 \sim T^{-3}$ dependence is derived using a pseudopotential modeling of the phonon-induced spin relaxation of conduction electrons in silicon.

According to the graph, at room temperature, the spin relaxation time is about 10 ns, electron lifetime from *Electrical properties of Silicon (Si)* approximates to 0.2 μs, and thus the spin lifetime τ_s is about 10 ns. This corresponds to a spin diffusion length of 2 μm. And although the spin lifetime in silicon is longer than in other semiconductors, it is the ratio of times τ_s/τ that counts for polarized luminescence measurement (Eq. 4.7).

B.5 Attempts to measure optical orientation in silicon

Due to the small ratio of lifetimes $\tau_s/\tau < 10^{-3}$ and weak luminescence, the photoluminescence technique is not very well applied to the case of silicon. There were certainly attempts to measure photoluminescence from Silicon. Frederic Roux 2008,

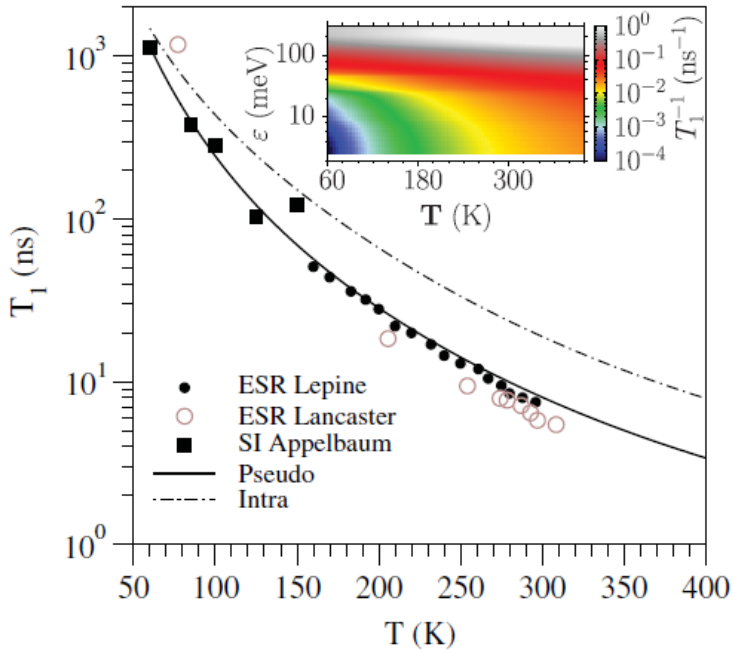

FIGURE B.5: Spin relaxation due to Elliott-Yafet relaxation mechanism for low doping densities in silicon.

during his thesis work in the laboratory of Condensed Matter Physics at Ecole Polytechnique, performed the polarized photoluminescence experiment on silicon samples of various doping concentrations, at room and nitrogen temperatures. Despite all the measures taken, such as increasing τ_s/τ ratio by diminishing electron lifetime by playing with different doping densities or by introducing deep centers of recombination via doping with gold, no polarization signal larger than 10^{-3} (the detection limit) was observed. It became clear at this point that the classical method of polarized photoluminescence is not suitable for silicon and one should find a distinct method to study spin in silicon.

The following approach that was proposed and implemented in our laboratory consisted in studying the polarization of the conduction electrons by means of spin-resolved low-energy photoemission spectroscopy. In a photoemission experiment, the sample is exposed to light which induces emission of electrons, whose energy and spin can be further analyzed. The relevant time scale in this case is the escape time, which is much shorter than the lifetime. Preliminary to all measurements the samples are activated to negative electron affinity by Cesium and Oxygen adsorption, which enables photo excitation very close to the band gap. A tunable laser is used to pump different energetic levels: from near the fundamental gap excitation

(1.12 eV) towards excitation with UV light of 4.8 eV. The polarization of 13 % was measured by F. Roux for excitation with light of 3.33 eV energy at 120 K and almost 10 % polarization was measured at room temperatures (300 K) with excitation light of 3.28 eV. Both peaks are situated around 3.1 eV of electron energy, in the vicinity of the direct gap $E_{\Gamma 1}$, that might involve indirect as well transitions to X- and L-valleys.

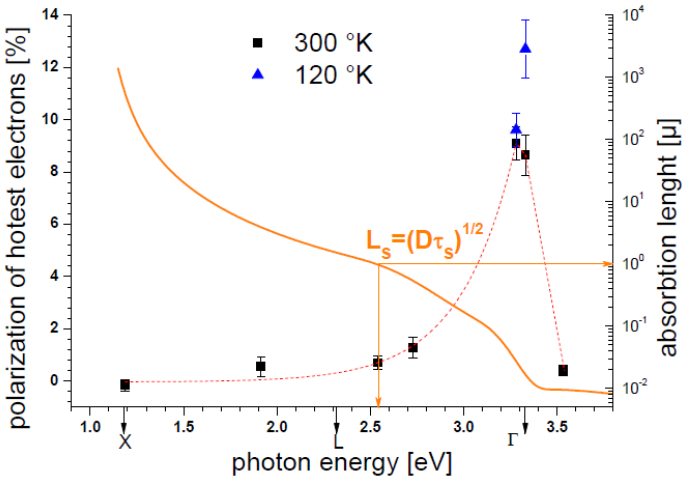

FIGURE B.6: The maxima of electron polarization as a function of excitation energy at 300 K and 120 K in the photoemission experiment conducted on Si (Roux, 2008).

The difficulty of the study of electrons close to the band gap lies in longer absorption depths and the fact that electrons are created throughout the whole sample and they relax their spin when diffuse to the surface before being emitted into the vacuum and analyzed. The technique becomes more effective for photon energies of absorption depth smaller than the diffusion length of electrons. In this case the electrons are more likely to conserve their spin at the moment of emission.

Low polarization values $\sim -0.4\%$, as presented in Fig. B.7, near the fundamental gap were obtained by Igor Favorskiy (2013) who followed the work of Frederic Roux. The detailed discussion of direct transitions $E_{\Gamma 1}$ and $E_{\Gamma 2}$ is given. Samples of different thickness are examined with an idea to spatially limit electron diffusion, but as can be seen from the figure, there is no clear variation in the P_i with thickness. Yet no confirmation of spin nature of the small signal was performed, such as Hanle experiment which is not compatible with the experimental setup.

Apart from optical attempts to create and detect spin, there were a lot of experiments on electrical injection, manipulation and detection of spin of electrons

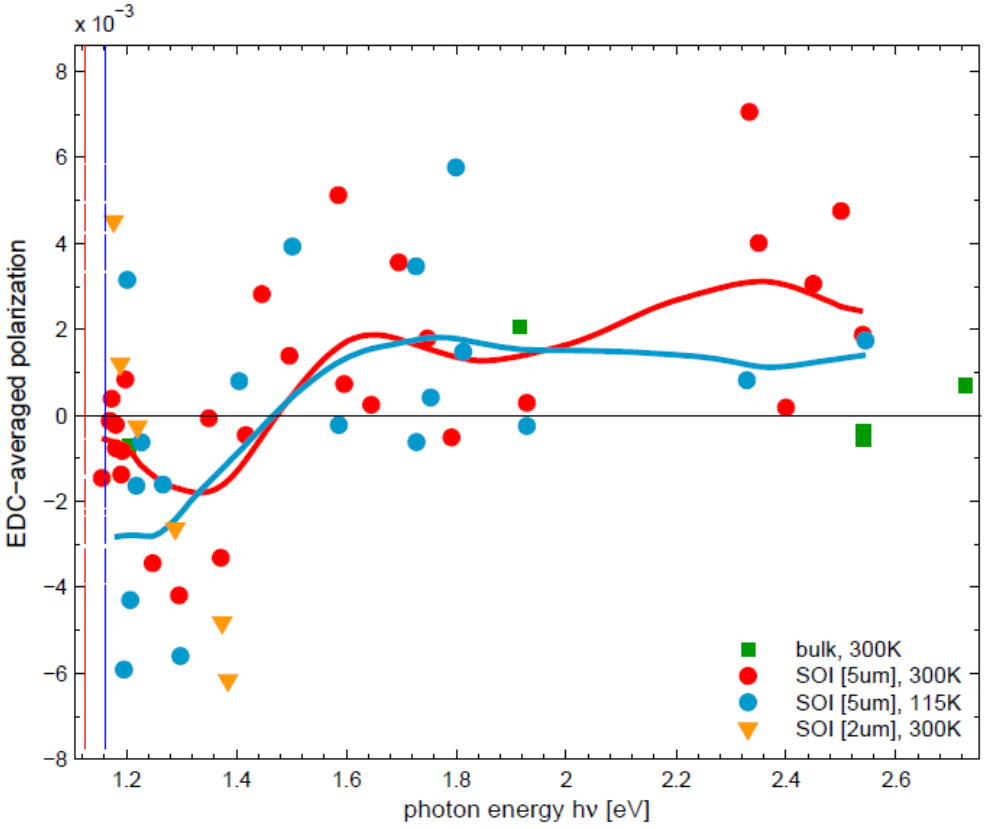

FIGURE B.7: P_{EL} from photoemission experiments. Silicon samples of different thickness are measured. Solid lines represent running average interpolations (Favorskiy, 2013)

in silicon. In 2007, spin injection and detection was demonstrated (Appelbaum, Huang, and Monsma, 2007) across 10 μm undoped silicon with lower bound estimation for the spin lifetime of 1 ns at temperature 85 K. The previous obstacle of impedance mismatch between high-conductive ferromagnet and a much more resistive semiconductor, that prevented from observation of electrical spin injection, was overcome by spin-dependent hot-electron filtering through ferromagnetic thin films. Later that year the same group (Huang, Monsma, and Appelbaum, 2007) reported spin transport at 60 K through a 350 μm undoped silicon and the spin lifetime was estimated to be 500 ns this time.

Jonker et al., 2007, demonstrate electrical injection from the Fe contact using Al_2O_3 tunnel barrier contact and detection of polarized photoluminescence at low temperatures (5, 50 and 80 K). The studied heterostructures include Si n-i-p structures, GaAs quantum well (Si/AlGaAs/GaAs/AlGaAs structure) and some reference samples with different type of tunnel contact, such as In/Al_2O_3 non-magnetic metal contact to confirm that the circular polarization of luminescence is due to the

tunneling from Fe and not due to field-induced effects in Si. The degree of circular polarization of luminescence from Si heterostructure reaches 3.7% at 5 K, 2.1% at 50 K and 2% at 80 K. By approximating values of spin relaxation time T_1 and electron lifetime τ from the literature to 10 μs and 0.1 ms, correspondingly, and by using Eq. 4.4 in their case, they get the values of initial polarizations of 30%. Its absolute value agrees with theoretical paper by Li and Dery although their result was never reproduced by an independent group of experimentalist.

The progress to room temperatures was made by Dash et al. They demonstrated electrical injection and detection of spin in n- and p-type silicon, along with the confirmation of the spin nature of the signal by performing Hanle type measurements(experiment). The extracted spin lifetimes are greater than 140 ps for conduction electron in heavily doped n-type silicon ($n = 1.8 \times 10^{19}$ cm^{-3}) and greater than 270 ps for holed in heavily doped p-type silicon ($p = 4.8 \times 10^{18}$ cm^{-3}).

All electrical injection experiments indicate that it is possible to achieve spin polarization of electrons in silicon, although there are a lot of interface physics complications that interfere with the pure spin phenomena. The difficulty of sample preparation holds back from effortless analysis of doping densities dependences.

Bibliography

Appelbaum, Ian, Biqin Huang, and Douwe J. Monsma (2007). "Electronic measurement and control of spin transport in silicon". In: *Nature* 447, pp. 295–298. DOI: 10.1038/nature05803. URL: https://www.nature.com/articles/nature05803.

Armitage, NP (2014). "Constraints on Jones transmission matrices from time-reversal invariance and discrete spatial symmetries". In: *Physical Review B* 90.3, p. 035135.

Atatüre, Mete et al. (2007). "Observation of Faraday rotation from a single confined spin". In: *Nature Physics* 3.2, p. 101.

Baumberg, JJ et al. (1994). "Spin beats and dynamical magnetization in quantum structures". In: *Physical review letters* 72.5, p. 717.

BF-4 Magnetic Field Induction Sensor (2009). Schlumberger. URL: https://www.slb.com/resources/other_resources/product_sheets/rd/bf_4.aspx.

Bona, G. L. and F. Meier (1985). "Observation of the spin-orbit splitting at the valence band edge of silicon by spin-polarized photoemission". In: *Solid State Communications* 55.9, pp. 851–855.

Bouchiat, V (2009). "Detection of magnetic moments using a nano-SQUID: limits of resolution and sensitivity in near-field SQUID magnetometry". In: *Supercond. Sci. Technol.* 22. DOI: https://doi.org/10.1088/0953-2048/22/6/064002. URL: http://iopscience.iop.org/article/10.1088/0953-2048/22/6/064002.

Bouckaert, LP (1936). "LP Bouckaert, R. Smoluchowski, and E. Wigner, Phys. Rev. 50, 58 (1936)". In: *Phys. Rev.* 50, p. 58.

Butta, M and I Sasada (2014). "Method for offset suppression in orthogonal fluxgate with annealed wire core". In: *Sensor Letters* 12.8, pp. 1295–1298.

Cadiz, F et al. (2014). "All optical method for investigation of spin and charge transport in semiconductors: Combination of spatially and time-resolved luminescence". In: *Journal of Applied Physics* 116.2, p. 023711.

Cardona, Manuel (1961). "Electron effective masses of InAs and GaAs as a function of temperature and doping". In: *Physical Review* 121.3, p. 752.

Chang, Chia-Yu et al. (2011). "Sensitive Faraday rotation measurement with auto-balanced photodetection". In: *Review of Scientific Instruments* 82.6, 063112. DOI: http://dx.doi.org/10.1063/1.3602927. URL: http://scitation.aip.org/content/aip/journal/rsi/82/6/10.1063/1.3602927.

Cheng, J. L. et al. (2011). "Theory of optical spin orientation in silicon". In: *Phys. Rev. B* 83 (16), p. 165211. DOI: 10.1103/PhysRevB.83.165211. URL: https://link.aps.org/doi/10.1103/PhysRevB.83.165211.

Cheng, JL, MW Wu, and Jaroslav Fabian (2010). "Theory of the spin relaxation of conduction electrons in silicon". In: *Physical review letters* 104.1, p. 016601.

Chuang, Pojen et al. (2015). "All-electric all-semiconductor spin field-effect transistors". In: *Nature nanotechnology* 10, pp. 35–39. URL: https://www.nature.com/articles/nnano.2014.296.

Clarke, John (1997). "High-Tc squids". In: *Current Opinion in Solid State and Materials Science* 2.1, pp. 3–10.

Cohen, Marvin L and James R Chelikowsky (2012). *Electronic structure and optical properties of semiconductors*. Vol. 75. Springer Science & Business Media.

Crassee, Iris et al. (2011). "Giant Faraday rotation in single-and multilayer graphene". In: *Nature Physics* 7.1, p. 48.

Crooker, SA et al. (2004). "Spectroscopy of spontaneous spin noise as a probe of spin dynamics and magnetic resonance". In: *Nature* 431.7004, p. 49.

Crooker, SA et al. (2007). "Optical and electrical spin injection and spin transport in hybrid Fe/GaAs devices". In: *Journal of applied physics* 101.8, p. 081716.

Cryogenic Limited - S700X SQUID Magnetometer (2018). Cryogenic Ltd. URL: http://www.cryogenic.co.uk/products/s700x-squid-magnetometer.

Dahbashi, Ramin et al. (2014). "Optical spin noise of a single hole spin localized in an (InGa) As quantum dot". In: *Physical review letters* 112.15, p. 156601.

Dandridge, Anthony, Alan B Tveten, and Thomas G Giallorenzi (1982). "Homodyne demodulation scheme for fiber optic sensors using phase generated carrier". In: *IEEE Transactions on microwave theory and techniques* 30.10, pp. 1635–1641.

Dang, HB, AC Maloof, and MV Romalis (2010). "Ultrahigh sensitivity magnetic field and magnetization measurements with an atomic magnetometer". In: *Applied Physics Letters* 97.15, p. 151110.

Dash, Saroj P et al. (2009). "Electrical creation of spin polarization in silicon at room temperature". In: *Nature* 462.7272, p. 491.

Datta, Supriyo and Biswajit Das (1990). "Electronic analog of the electro-optic modulator". In: *Applied Physics Letters* 56.7, pp. 665–667. DOI: 10.1063/1.102730. eprint: https://doi.org/10.1063/1.102730. URL: https://doi.org/10.1063/1.102730.

Díaz-Michelena, Marina (2009). "Small magnetic sensors for space applications". In: *Sensors* 9.4, pp. 2271–2288.

Dyakonov, MI and VI Perel (1971). "Spin orientation of electrons associated with the interband absorption of light in semiconductors". In: *Soviet Journal of Experimental and Theoretical Physics* 33, p. 1053.

Ekimov, AI and VI Safarov (1970). "Optical orientation of carriers in interband transitions in semiconductors". In: *JETP Lett* 12.198, pp. 1–1.

— (1971). "Influence of spin relaxation of 'hot'electrons on the effectiveness of optical orientation in semiconductors". In: *ZhETF Pis Red* 13, p. 700.

Electrical properties of Silicon (Si). Ioffe Institute. URL: http://www.ioffe.ru/SVA/NSM/Semicond/Si/electric.html.

Favorskiy, I et al. (2010). "Circularly polarized luminescence microscopy for the imaging of charge and spin diffusion in semiconductors". In: *Review of Scientific Instruments* 81.10, p. 103902.

Favorskiy, Igor (2013). "Optical pumping in Silicon thin films". PhD thesis. Ecole Polytechnique.

Fermon, C and Myriam Pannetier-Lecoeur (2013). "Noise in GMR and TMR Sensors". In: *Giant Magnetoresistance (GMR) Sensors*. Springer, pp. 47–70.

Fried, Alexander, Martin Fejer, and Aharon Kapitulnik (2014). "A scanning, all-fiber Sagnac interferometer for high resolution magneto-optic measurements at 820 nm". In: *Review of Scientific Instruments* 85.10, p. 103707.

Furis, M et al. (2007). "Local Hanle-effect studies of spin drift and diffusion in n: GaAs epilayers and spin-transport devices". In: *New Journal of Physics* 9.9, p. 347.

GaAs - Gallium Arsenide: Band structure and carrier concentration. Ioffe. URL: http://www.ioffe.ru/SVA/NSM/Semicond/GaAs/bandstr.html.

Gabriel, Cedric J and Herbert Piller (1967). "Determination of the optical Verdet coefficient in semiconductors and insulators". In: *Applied optics* 6.4, pp. 661–667.

Giri, Rakshyakar et al. (2012). "Giant photoinduced Faraday rotation due to the spin-polarized electron gas in an n-GaAs microcavity". In: *Physical Review B* 85.19, p. 195313.

Giri, Rakshyakar et al. (2013). "Nondestructive measurement of nuclear magnetization by off-resonant faraday rotation". In: *Physical review letters* 111.8, p. 087603.

Goldstein, Dennis H (2003). *Polarized Light, revised and expanded*. CRC press.

Grosz, Asaf et al. (2016). "A high-resolution planar Hall effect magnetometer for ultra-low frequencies". In: *IEEE Sensors Journal* 16.9, pp. 3224–3230.

Hanle, Wilhelm (1924). "Über magnetische beeinflussung der polarisation der resonanzfluoreszenz". In: *Zeitschrift für Physik* 30.1, pp. 93–105.

Hermann, C et al. (2001). "Surface-enhanced magneto-optics in metallic multilayer films". In: *Physical Review B* 64.23, p. 235422.

Hinnrichs, Colmar et al. (2001). "Dependence of sensitivity and noise of fluxgate sensors on racetrack geometry". In: *IEEE transactions on magnetics* 37.4, pp. 1983–1985.

Huang, Biqin, Douwe J. Monsma, and Ian Appelbaum (2007). "Coherent Spin Transport through a 350 Micron Thick Silicon Wafer". In: *Phys. Rev. Lett.* 99 (17), p. 177209. DOI: 10.1103/PhysRevLett.99.177209. URL: https://link.aps.org/doi/10.1103/PhysRevLett.99.177209.

Hwang, CJ (1971). "Doping dependence of hole lifetime in n-type GaAs". In: *Journal of Applied Physics* 42.11, pp. 4408–4413.

Jaklevic, RC et al. (1964). "Quantum interference effects in Josephson tunneling". In: *Physical Review Letters* 12.7, p. 159.

Jansen, Ron (2012). "Silicon spintronics". In: *Nature Materials* 11.5, p. 400.

Jonker, Berend T. (1999). "Polarized optical emission due to decay or recombination of spin-polarized injected carriers". Pat. 5,874,749.

Jonker, Berend T et al. (2007). "Electrical spin-injection into silicon from a ferromagnetic metal/tunnel barrier contact". In: *Nature Physics* 3.8, p. 542.

Josephson, B.D. (1962). "Possible new effects in superconductive tunnelling". In: *Physics Letters* 1.7, pp. 251 –253. ISSN: 0031-9163. DOI: https://doi.org/10.1016/0031-9163(62)91369-0. URL: http://www.sciencedirect.com/science/article/pii/0031916362913690.

Kapitulnik, A., J. S. Dodge, and M. M. Fejer (1994). "High-resolution magneto-optic measurements with a Sagnac interferometer". In: *J. Appl. Phys.* 75.10. URL: https://doi.org/10.1063/1.356814.

Kastler, Alfred (1957). "Optical Methods of Atomic Orientation and of Magnetic Resonance*". In: *J. Opt. Soc. Am.* 47.6, pp. 460–465. DOI: 10.1364/JOSA.47.

000460. URL: http://www.osapublishing.org/abstract.cfm?URI=josa-47-6-460.

Kato, Y. K. et al. (2004). "Observation of the Spin Hall Effect in Semiconductors". In: *Science* 306.5703, pp. 1910–1913. DOI: 10.1126/science.1105514. eprint: http://www.sciencemag.org/content/306/5703/1910.full.pdf. URL: http://www.sciencemag.org/content/306/5703/1910.abstract.

Kikkawa, JM and DD Awschalom (1999). "Lateral drag of spin coherence in gallium arsenide". In: *Nature* 397.6715, p. 139.

Kim, P. H. et al. (2013). "Nanoscale torsional optomechanics". In: *Applied Physics Letters* 102.5, p. 053102. DOI: 10.1063/1.4789442. eprint: https://doi.org/10.1063/1.4789442. URL: https://doi.org/10.1063/1.4789442.

Koblischka, MR and RJ Wijngaarden (1995). "Magneto-optical investigations of superconductors". In: *Superconductor Science and Technology* 8.4, p. 199.

Koo, Hyun Cheol et al. (2009). "Control of Spin Precession in a Spin-Injected Field Effect Transistor". In: *Science* 325.5947, pp. 1515–1518. ISSN: 0036-8075. DOI: 10.1126/science.1173667. eprint: http://science.sciencemag.org/content/325/5947/1515.full.pdf. URL: http://science.sciencemag.org/content/325/5947/1515.

Lampel, Georges (1968). "Nuclear Dynamic Polarization by Optical Electronic Saturation and Optical Pumping in Semiconductors". In: *Phys. Rev. Lett.* 20 (10), pp. 491–493. DOI: 10.1103/PhysRevLett.20.491. URL: http://link.aps.org/doi/10.1103/PhysRevLett.20.491.

Lancaster, G, J A van Wyk, and E E Schneider (1964). "Spin-lattice relaxation of conduction electrons in silicon". In: *Proceedings of the Physical Society* 84.1, p. 19. URL: http://stacks.iop.org/0370-1328/84/i=1/a=304.

Lépine, Daniel J (1970). "Spin resonance of localized and delocalized electrons in phosphorus-doped silicon between 20 and 30 K". In: *Physical Review B* 2.7, p. 2429.

Li, Jiaming et al. (2014). "Shot-noise-limited optical Faraday polarimetry with enhanced laser noise cancelling". In: *Journal of Applied Physics* 115.10, 103101. DOI: http://dx.doi.org/10.1063/1.4867743. URL: http://scitation.aip.org/content/aip/journal/jap/115/10/10.1063/1.4867743.

Li, Pengke and Hanan Dery (2010). "Theory of Spin-Dependent Phonon-Assisted Optical Transitions in Silicon". In: *Phys. Rev. Lett.* 105 (3), p. 037204. DOI: 10.

1103/PhysRevLett.105.037204. URL: https://link.aps.org/doi/10.1103/PhysRevLett.105.037204.

Litvinenko, KL et al. (2008). "Temperature dependence of the electron Landé g factor in InSb and GaAs". In: *Physical Review B* 77.3, p. 033204.

Mahmood, Waqas and Qing Zhao (2015). "The Double Jones Birefringence in Magneto-electric Medium". In: *Scientific reports* 5, p. 13963.

Nastos, F. et al. (2007). "Full band structure LDA and $\mathbf{k} \cdot \mathbf{p}$ calculations of optical spin-injection". In: *Phys. Rev. B* 76 (20), p. 205113. DOI: 10.1103/PhysRevB.76.205113. URL: http://link.aps.org/doi/10.1103/PhysRevB.76.205113.

Nilsson, G and G Nelin (1972). "Study of the homology between silicon and germanium by thermal-neutron spectrometry". In: *Physical Review B* 6.10, p. 3777.

Parsons, R. R. (1969). "Band-To-Band Optical Pumping in Solids and Polarized Photoluminescence". In: *Phys. Rev. Lett.* 23 (20), pp. 1152–1154. DOI: 10.1103/PhysRevLett.23.1152. URL: https://link.aps.org/doi/10.1103/PhysRevLett.23.1152.

Pierce, DT, F Meier, and P Zürcher (1975). "Direct observation of spin dependent electronic structure of GaAs using spin polarized photoemission". In: *Physics Letters A* 51.8, pp. 465–466.

Piller, Herbert (1972). "Faraday rotation". In: *Semiconductors and Semimetals*. Vol. 8. Elsevier, pp. 103–179.

Popović, RS (1989). "Hall-effect devices". In: *Sensors and Actuators* 17.1-2, pp. 39–53.

Ramsden, Edward (2001). *Hall Effect Sensors: Theory & Application*. Advanstar Communications Incorporated.

Ripka, P et al. (2003). "AMR magnetometer". In: *Journal of Magnetism and Magnetic materials* 254, pp. 639–641.

Ripka, Pavel (2001). *Magnetic sensors and magnetometers*. Artech House.

Romalis, Michael V. and Hoan B. Dang (2011). "Atomic magnetometers for materials characterization". In: *Materials Today* 14.6, pp. 258 –262. ISSN: 1369-7021. DOI: https://doi.org/10.1016/S1369-7021(11)70140-7. URL: http://www.sciencedirect.com/science/article/pii/S1369702111701407.

Roux, Frédéric (2008). "Etude du pompage optique du silicium par photoluminescence polarisée et photo-émission à basse énergie résolue en spin". PhD thesis. Ecole Polytechnique.

Rowe, ACH et al. (2017). "Polarizers, optical bridges, and Sagnac interferometers for nanoradian polarization rotation measurements". In: *Review of Scientific Instruments* 88.4, p. 043903.

Rugar, D. et al. (2004). "Single spin detection by magnetic resonance force microscopy". In: *Nature* 430, pp. 329–332. DOI: doi:10.1038/nature02658. URL: https://www.nature.com/articles/nature02658.

Ryzhov, II et al. (2015). "Measurements of nuclear spin dynamics by spin-noise spectroscopy". In: *Applied Physics Letters* 106.24, p. 242405.

Schmelz, M et al. (2011). "Field-stable SQUID magnetometer with sub-fT Hz- 1/2 resolution based on sub-micrometer cross-type Josephson tunnel junctions". In: *Superconductor Science and Technology* 24.6, p. 065009.

Slobodskyy, A et al. (2003). "Voltage-controlled spin selection in a magnetic resonant tunneling diode". In: *Physical review letters* 90.24, p. 246601.

Spielman, S. et al. (1990). "Test for nonreciprocal circular birefringence in $YBa_2Cu_3O_7$ thin films as evidence for broken time-reversal symmetry". In: *Phys. Rev. Lett.* 65 (1), pp. 123–126. DOI: 10.1103/PhysRevLett.65.123. URL: http://link.aps.org/doi/10.1103/PhysRevLett.65.123.

Su, CW, SC Chang, and YC Chang (2013). "Periodic reversal of magneto-optic Faraday rotation on uniaxial birefringence crystal with ultrathin magnetic films". In: *AIP Advances* 3.7, p. 072125.

Temperature dependence of the energy gap (GaAs). URL: http://www.ioffe.ru/SVA/NSM/Semicond/GaAs/bandstr.html#Temperature.

TFM100-G2 Ultra miniature triaxial fluxgate magnetometer (2008). Billingsley Aerospace & Defense. URL: https://magnetometer.com/wp-content/uploads/TFM100-G2-Spec-Sheet-February-2008.pdf.

Vladimirova, Maria et al. (2018). "Spin temperature concept verified by optical magnetometry of nuclear spins". In: *Physical Review B* 97.4, p. 041301.

Weber, Werner (1977). "Adiabatic bond charge model for the phonons in diamond, Si, Ge, and α- Sn". In: *Physical Review B* 15.10, p. 4789.

Wernsdorfer, W, D Mailly, and A Benoit (2000). "Single nanoparticle measurement techniques". In: *Journal of Applied Physics* 87.9, pp. 5094–5096.

Wernsdorfer, Wolfgang (2009). "From micro- to nano-SQUIDs: applications to nanomagnetism". In: *Supercond. Sci. Technol.* 22. URL: http://iopscience.iop.org/article/10.1088/0953-2048/22/6/064013/meta.

Wood, Robert Williams, Alexander Ellett, et al. (1923). "On the influence of magnetic fields on the polarisation of resonance radiation". In: *Proc. R. Soc. Lond. A* 103.722, pp. 396–403.

Wu, Marcelo et al. (2017). "Nanocavity optomechanical torque magnetometry and radiofrequency susceptometry". In: *Nature Nanotechnology* 12, pp. 127–131.

Xia, Jing et al. (2006). "Modified Sagnac interferometer for high-sensitivity magneto-optic measurements at cryogenic temperatures". In: *Applied Physics Letters* 89.6, 062508. DOI: http://dx.doi.org/10.1063/1.2336620. URL: http://scitation.aip.org/content/aip/journal/apl/89/6/10.1063/1.2336620.

Yabukami, S et al. (2009). "A thin film magnetic field sensor of sub-pT resolution and magnetocardiogram (MCG) measurement at room temperature". In: *Journal of Magnetism and Magnetic Materials* 321.7, pp. 675–678.

Yang, Luyi et al. (2015). "Long-lived nanosecond spin relaxation and spin coherence of electrons in monolayer MoS 2 and WS 2". In: *Nature Physics* 11.10, p. 830.

Yu, Peter Y. and Manuel Cardona (2010). *Fundamentals of Semiconductors*. Ed. by H. Eugene Stanley and William T. Rhodes. Fourth Edition. Graduate Texts in Physics. Springer-Verlag Berlin Heidelberg. DOI: 10.1007/978-3-642-00710-1. URL: https://www.springer.com/fr/book/9783642007095.

Zakharchenya, BI et al. (1971). "Effect of optical orientation of electron spins in a GaAs crystal". In: *Zh. Eksp. Teor. Fiz* 13, pp. 195–197.

Zerrouati, K. et al. (1988). "Spin-lattice relaxation in p -type gallium arsenide single crystals". In: *Phys. Rev. B* 37 (3), pp. 1334–1341. DOI: 10.1103/PhysRevB.37.1334. URL: http://link.aps.org/doi/10.1103/PhysRevB.37.1334.

Zutic, Igor, Jaroslav Fabian, and S. Das Sarma (2004). "Spintronics: Fundamentals and applications". In: *Rev. Mod. Phys.* 76 (2), pp. 323–410. DOI: 10.1103/RevModPhys.76.323. URL: https://link.aps.org/doi/10.1103/RevModPhys.76.323.

université PARIS-SACLAY
ÉCOLE DOCTORALE
INTERFACES
Approches Interdisciplinaires : Fondements, Applications et Innovation

Titre : Limites de détection magnéto-optique pour la spintronique des semi-conducteurs

Mots clés : pompage optique, magnéto-optique, semi-conducteurs, spin

Résumé : Ce travail explore l'utilisation de l'effet magnéto-optique pour étudier la dynamique de spin des électrons de conduction dans les semi-conducteurs non magnétiques lorsqu'ils sont pompés avec des photons polarisés circulairement. En général, les moments magnétiques hors-équilibre induits optiquement dans les semi-conducteurs non magnétiques sont plus petits que ceux des matériaux magnétiques. L'effet magnéto-optique en principe offre une sensibilité suffisante pour détecter ces faibles moments magnétiques via une mesure de rotation Faraday dans la limite de bruit de photons. Nous avons comparés trois méthodes de détection: les polariseurs partiellement croisés, l'interféromètre de Sagnac et le pont optique. L'interféromètre de Sagnac se révèle fonctionnellement équivalent aux polariseurs partiellement croisés, avec une sensibilité diminuée par la perte de photons à chacun des séparateurs de faisceaux nécessairement présents dans cette configuration expérimentale. Par contre, il a été démontré précédemment que les interféromètres de Sagnac permettent de faire la distinction entre les rotations dites réciproques et non réciproques, et cette thèse propose de nouvelles géométries de Sagnac pour distinguer les rotations en fonction de leurs symétries en temps et en parité. La technique du pont optique présente les meilleures performances. Elle permet une mesure de l'angle de rotation de Faraday limitée par le bruit de photons, même avec des puissances lumineuses importantes reçues par les détecteurs, ce qui permet d'obtenir la meilleure figure de mérite possible. Dans les expériences conduites sur des matériaux magnétiques, un bruit de quelques nrad/$\sqrt{\text{Hz}}$ a été mesuré pour une puissance de sonde de 10 mW. Une série de mesures de rotation Faraday pompe-sonde à température ambiante a été réalisée sur GaAs pompé optiquement. Les plus grands signaux sont obtenus lorsque le moment magnétique généré et détecté est maximisé en focalisant fortement les faisceaux pompe et sonde et en choisissant une longueur d'onde de la sonde accordée à une résonance optique dans la structure électronique. Les mesures en champ magnétique transversal montrent un champ Hanle de 0.43 T, à partir duquel on déduit la durée de vie de spin de 88 ps.

Title : Magneto-optical detection limits for semiconductor spintronics

Keywords : optical pumping, magneto-optics, semiconductors, spin

Abstract : This work explores the use of the magneto-optical Kerr effect to study conduction electron spin dynamics in non-magnetic semiconductors when pumped with circularly polarized photons. Typically, non-equilibrium, optically-induced magnetic moments in non-magnetic semiconductors are orders of magnitude smaller than those of magnetized materials, including both magnetic and non-magnetic materials in an external magnetic field. The magneto-optical Kerr effect in principal offers sufficient sensitivity to detect such small magnetic moment via a measurement of the Faraday rotation angle of a probe beam in the photon shot noise limit. Three detection configurations have been experimentally compared: partially crossed polarizers, a Sagnac interferometer and an optical bridge. The Sagnac interferometer is shown to be functionally equivalent to partially crossed polarizers, although its sensitivity is compromised by lost photons at each of the obligatory beam splitters present in such a geometry. On the other hand, it has previously been shown that Sagnac interferometers can distinguish between so-called reciprocal and non-reciprocal rotations, and this thesis proposes novel Sagnac geometries to distinguish rotations according to their time and parity symmetries. The optical bridge technique allows for a photon-shot noise limited measurement of the Faraday rotation angle, even with large photon intensities on the detectors, thereby yielding the best possible figure-of-merit. In demonstrations on magnetic materials, a noise floor of a few nrad/$\sqrt{\text{Hz}}$ was measured for a probe power of 10 mW. A series of room-temperature, pump-probe Faraday rotation measurements is performed on optically pumped GaAs to compare and contrast this method with standard polarized photo-luminescence techniques. The largest signals are found when the locally probed moment is maximized by strongly focusing the pump and probe beams, and by choosing a probe wavelength tuned to an optical resonance in the electronic structure. Measurements in transverse magnetic field show a Hanle field of 0.43 T, from which the spin lifetime of 88 ps is deduced.

Université Paris-Saclay
Espace Technologique / Immeuble Discovery
Route de l'Orme aux Merisiers RD 128 / 91190 Saint-Aubin, France